Journal of Advanced Materials and Processing

Islamic Azad University - Najafabad Branch

Journal of Advanced Materials and Processing

Vol.10, No.1, Winter 2022.

ISSN: 2322-388X

E-ISSN: 2345-4601

Publisher: Najafabad Branch, Islamic Azad University, Iron and Steel Association of Iran

Production manager: Mostafa Salehi

Executive assistant: Leily Rezaei, Seyedeh Razieh Anvari

Address: Journal of Advanced Materials and Processing

Department of Materials Engineering, Najafabad Branch, Islamic Azad University, Najafabad, Isfahan, Iran

P.O. Box: 517

Tel:+98-31-42292512 **Fax:**+98-31-42291008

Website: www.jmatpro.iaun.iau.ir

Email:jmatpro@iaun.ac.ir

Table of Content

JMATPRO	Journal of Advanced Materials and Processing 10 (1): 3-12, Winter 2022 http://jmatpro.iaun.iau.ir 20.1001.1.2322388.2022.10.1.1.4

Research Paper

Electromagnetic Waves Absorption of the Epoxy Resin-MWCNT Composite Synthesis via Ultrasonic Bath and Milling Process

Sadegh Shahriyari[1], Mahdi Omidi[1*], Seyyed Ali Hassanzadeh-Tabrizi[1], Mahdi Yeganeh[2], Hamid Reza Bakhsheshi-Rad[1]

1. Advanced Materials Research Center, Department of Materials Engineering, Najafabad Branch, Islamic Azad University, Najafabad, Iran

2. Department of Materials Science and Engineering, Faculty of Engineering, Shahid Chamran University of Ahvaz, Ahvaz, Iran

ARTICLE INFO

Article history:

Received 19 October 2021
Accepted 23 December 2021
Available online 1 January 2022

Keywords:
Electromagnetic waves absorption
MWCNT
Epoxy resin
Ultrasonic
Composite

ABSTRACT

In this study, ultrasonic bath and milling processes were used to synthesis epoxy resin-multiwalled carbon nanotubes (MWCNT) composite, and their effect on the absorption of magnetic waves was investigated using the Vector Network Analyzer (VNA) test. The effect of the concentration of MWCNT used to attract the wave's magnetic part in the epoxy resin matrix is also investigated. This study showed that the optimal amount of MWCNT in this epoxy resin-MWCNT composite was about 5 wt.% for the ultrasonic bath method, while it was around 15 wt% for the milling method. The ultrasonic bath caused the reflection losses (RL) value reaches to about -25 dB in the range of 9 to 11 GHz. The results of the VSM test showed that the composite produced from epoxy resin and MWCNT is a soft magnetic material. Also, the sample produced in the ultrasonic bath process has a higher magnetic saturation than the milling process, which causes it to absorb more electromagnetic waves.

Citation: Shahriyari, S.; Omidi, M; Hassanzadeh-Tabrizi, S.A.; Yeganeh, M.; Bakhsheshi-Rad, H.R. (2022) Electromagnetic Waves Absorption of the Epoxy Resin-MWCNT Composite Synthesis via Ultrasonic Bath and Milling Process, Journal of Advanced Materials and Processing, 10 (1), 3-12. Dor: 20.1001.1.2322388.2022.10.1.1.4

[*] **Corresponding Author**
E-Mail Address: m_omidi@iaun.ac.ir

1. Introduction

Today's world relies heavily on technologies based on electromagnetic radiation, which is one of the most fundamental phenomena of nature. With the advancement of technology, unexpected problems are created for human health. For example, the more devices containing electromagnetic waves are used, the more human health is threatened. Since electromagnetic waves have many applications in the GHz frequency range for mobile phones, communication networks, radar systems, etc., protection against waves in this range is essential for humans [1-6]. Electromagnetic absorbers are among the most fundamental parts of wireless communications, etc., which have attracted much attention in the last decade [7-9]. These materials reduce the amount of reflected wave energy, thereby attenuating electromagnetic waves. Electromagnetic absorbers are used as microwave absorbers and for shielding applications. Absorbents must have properties that enhance their performance, including a) high absorption of electromagnetic waves in the high-frequency range, b) the electromagnetic wave absorbent material must be thin thickness, c) the absorption range of the absorbent material should cover the wide frequency range, d) other properties of the adsorbent materials include their high mechanical strength and low weight, e) it must also have high thermal and chemical stability and f) Finally, low production costs can be mentioned as a feature for electromagnetic wave absorbers [10-14].

An electromagnetic wave absorber is a substance that attenuates the electromagnetic energy emitted, and there are generally two views on the absorption of electromagnetic waves. Microscopically, the performance of materials in electromagnetic fields is determined by the displacement of free electrons and their bonding in the electric field and the direction of their atomic motions in the magnetic field. According to Maxwell's equations, the adsorption rate of the adsorbent can be measured [10, 11]. From a macroscopic point of view, the reaction of materials (absorption and reflection) against electromagnetic waves is determined by three related parameters, electrical conductivity ($\varepsilon^* = \varepsilon' - i\varepsilon''$), magnetic permeability ($\mu^* = \mu' - i\mu''$), and electrical conductivity (σ) [12]. The (μ' , ε') real parts are related to storage, and (μ'', ε'') the imaginary parts are related to the dissipation of electromagnetic waves. Also, the imaginary part ratio to the real part is equal to the material loss factor [13]. The wave absorber must have wave resistance to dissipate it [14]. The wave resistance is defined by impedance and is presented in the following Equation (1):

$$z_{in} = \frac{z_{in}}{z_0} = \sqrt{\frac{\mu}{\varepsilon \tanh\left[-i2\pi\frac{d}{\lambda}\sqrt{\varepsilon\mu}\right]}} \quad (1)$$

where, μ, ε are magnetic permeability and dielectric permeability, respectively. It was worth noting that d, thickness, and λ are also the wavelengths of free space. By calculating the input impedance, the reflective loss is also obtained, which is presented in Equation (2):

$$RL(dB) = -20\, log\left(\frac{z_{in}-1}{z_{in}+1}\right) \quad (2)$$

Wave absorbers are typically selected from intermediate metals, oxides, hydroxides, nanoparticles, nanotubes, conductive polymers, and composites. These nanocomposites include conductive polymers (absorbers of the electric wavelength) and magnetic particles (absorbers of the magnetic wavelength) dispersed in the polymer matrix. When the dimensions of the structures of mineral compounds are reduced to the nanoscale, they have significant effects on their mechanical, optical, electrochemical, and thermal properties and the absorption of their electromagnetic waves [15-22]. Currently, epoxy resin-MWCNT composites are employed as microwave absorbers for shielding applications. Applications of some of the structures and materials used in the field of electromagnetism are: electromagnetic wave absorbers, electrical shields, antenna designs, protection of humans and biomaterials against electromagnetic waves, and improved electromagnetic compatibility [16-22]. In one study, the effect of commercial multi-walled CNTs with different diameters and length-to-diameter ratios on X-band microwave adsorption, MWCNT epoxy nano-composite, prepared by ultrasonic methods and the ball mill was investigated. The research showed that the MWCNT with the largest aspect ratio resulted in composites with the highest X-band microwave absorption performance, which is considerably better than that of reported pristine CNT/polymer composites with similar or lower thicknesses and CNT loadings below 4 wt% [23]. In this paper, we tried to investigate the effect of carbon nanotubes in a polymer matrix and the existence of different intermediate processes, including ultrasonic baths and the milling process, which affects the separation of nanotubes. Finally, this study aims to fabricate a nanocomposite from epoxy-MWCNT resin and to investigate the absorption power of electromagnetic waves at the scale of 12-8 GHz.

2. Materials and methods

In the present study, multi-walled carbon nanotubes with dimensions of 25 nm in diameter and 10 μm in length were used. The nanotubes used in this study were produced by the United Nanotech Innovations company (UNI), with purity and theoretical density of around 98% and 0.14 g/cm^3, respectively. Figure 1 shows the histogram and morphology of the nanotubes. It can be seen that the nanotubes are intertwined strands with dimensions of approximately 40 nm.

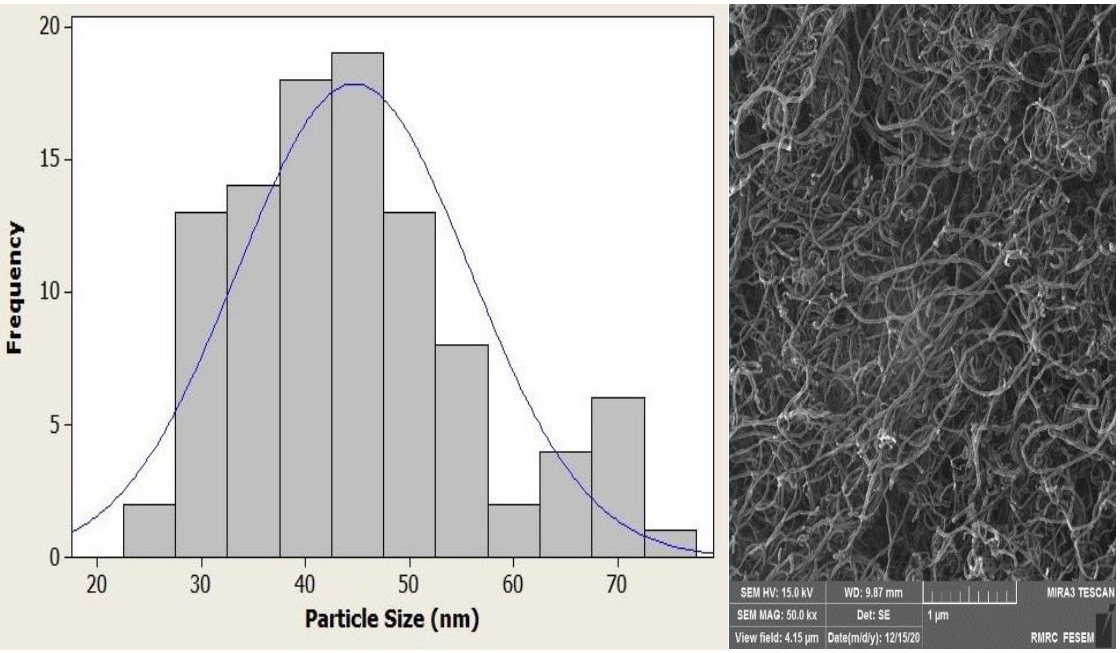

Fig. 1. Histogram and SEM image of MWCNTs powders.

The epoxy resin selected in this study consists of two components, EPL 1012 based on Bisphenol F-type and EPH112 as a hardener, listed in Table 1. Its low viscosity allows for complete impregnation of reinforcement fibers like glass, carbon, and aramid or mineral powder such as silica and makes it suitable for processing methods such as wet lay-up and Resin transfer molding (RTM).

Table 1. The thermal and physical properties of epoxy resin.

Properties	Amount	Unit	Standard
Volume Electrical Strength	$1.8*10^{15}$	Ohm.cm	ASTM D257
Surface Electrical Strength	$9.5*10^{12}$	Ohm	ASTM D257
Dielectric Constant	6	-	ASTM D150
Coefficient of Thermal Expansion	$6.2*10^{-5}$	$(C^0)^{-1}$	ASTM D864

In the present study, an ultrasonic bath and milling process was used to increase the absorption of electromagnetic waves. The carbon nanotubes were placed in a laboratory calibrated cylinder with 50 cc of ethanol. The carbon nanotubes and ethanol mixture was placed in an ultrasonic bath, and ultrasonic waves separated the nanotubes for 80 min. The frequency used in this step was set to 100 Hz. It is also worth noting that the milling process leads to an increase in the absorption of electromagnetic waves. A mixture of carbon nanotubes and ethanol was added to a steel cup. Stainless steel balls of four different sizes of 5, 7, 9, and 13 mm were used in the mixing process. The mixing process was performed wet, and the time used was one hour at 250 rpm in a planetary ball mill. To produce an epoxy resin-MWCNT composite, the weight values of the composite were calculated based on Equation 3:

$$m_C(gr) = (x)A + (1-x)B \quad (3)$$

where m_C is the weight of the composite in grams, A and B are the weight of the carbon nanotube and the composite matrix, respectively, X is the weight percentage of the reinforcing phase in the final composite. Also, in this formula, part B consists of two components, resin, and hardener, the ratio of which is shown in Equation 4.

$$B = \big((85\%)R + (15\%)H\big) \quad (4)$$

The resin is denoted by R and the hardener by H, and then, after mixing the composite materials in appropriate proportions in a sterile laboratory container for 3 min and using an electric mixer, they were mixed at a speed of 1000 rpm. After mixing, the resulting composite was placed in a drying oven. At this stage, to remove ethanol from the composite composition, a temperature of 110 °C and 24 hours were selected. At the end of the drying step, the sample was cut according to Waveguide (WR90) to perform the electromagnetic wave absorber test. The sample size for use in the networking analyzer (VNA) is 22.6 × 1.10 mm, and its thickness is equal to 5 mm. An electromagnetic wave absorption test was performed in the range of 8 to 12 GHz. A scanning electron microscope (SEM; MIRA3TESCAN-XMU) made by the TESCAN company in the Czech Republic

examined carbon nanotube morphology. Also, the VSM model LBKFB model of Meghnatis Daghigh Kavir Company in Iran investigated the material's magnetic state. In order to calculate the amount of electromagnetic waves absorption, a model networking analyst (VNA, HP 8410C) located in the antenna laboratory of Khajeh Nasir al-Din Tusi University has been selected. IR testing was performed by Bomem MB-Series FT-IR Spectrometer in MID-IR range.

3. Results and Discussion

Figure 2 exhibited the FTIR spectrum epoxy resin specimen without MWCNTs after drying and calcination. Regarding the epoxy resin, the absorption band indicative of the OH bond is observed between 3590 and 3180 cm^{-1}. Owing to the limited number of OH groups in this resin's molecule, the peak noticed is small. The epoxy group is indicated by the 908 cm^{-1} band (in the 947 to 865 cm^{-1} range), while the peak indicates the existence of an aromatic group at 1100 cm^{-1}. The bands at 2951 cm^{-1} and 2872 cm^{-1} are caused by the C–H stretching vibration of the methyl group, whereas the band at 2930 cm^{-1} is caused by the C–H stretching vibration of the methylene group. The methyl C–H in-plane bending symmetrical vibrations s and asymmetrical vibrations as are found at 1379 cm^{-1} and 1451 cm^{-1}, respectively.

At 1597 cm^{-1}, 1586 cm^{-1}, and 1498 cm^{-1}, the distinctive C=C stretching of the benzene ring could be observed. Peaks at 1232 cm^{-1} and 1028 cm^{-1} correlate to C–O stretching, which indicates the modified epoxy resin's molecular backbone. Figure 2b shows the FTIR spectra of epoxy resin samples containing MWCNTs, which revealed two additional peaks at 1696 cm^{-1} related to carbonyl groups (C=O) and 1397 cm^{-1} that related to carboxyl groups (–COO). These two peaks suggested that MWCNTs were effectively encapsulated into the epoxy matrix [24].

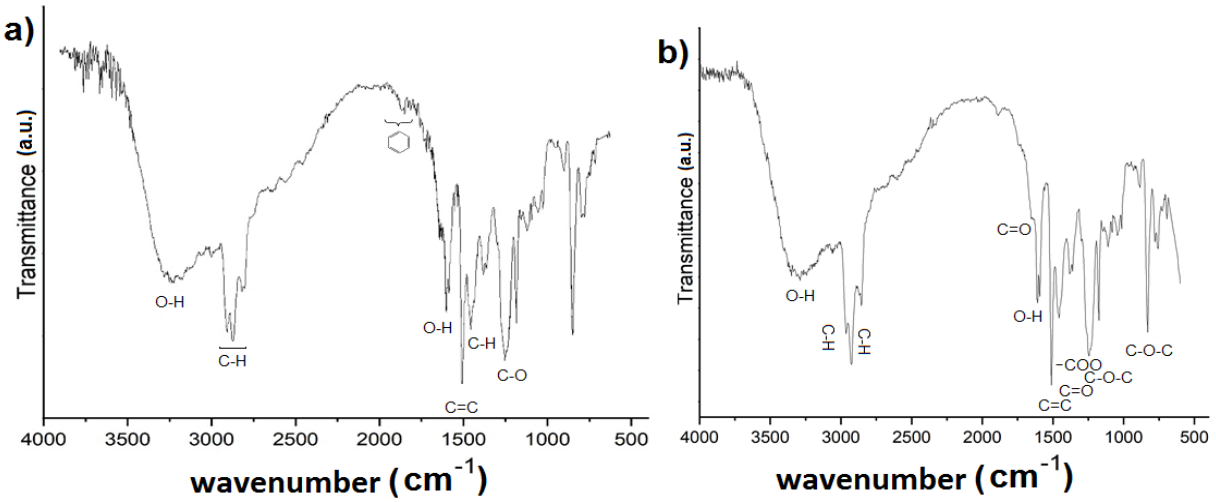

Fig. 2. The FTIR spectra of a) epoxy resin samples without MWCNTs and b) epoxy resin samples with MWCNTs

Figure 3 shows the results of the XRD test from ultrasonic and milling of the epoxy resin-MWCNT composite specimens. In both samples, the MWCNT peak is observed at an angle of 20 degrees. The MWCNT peak in the milling method has a decrease in intensity compared to the ultrasonic method. This decrease in intensity is due to the difference between the synthesis processes in these two samples. The result further confirms that there is no impurity in the synthesized specimens.

Figure 4 shows an electron microscope image of the sample surface with an ultrasonic bath's and no MWCNT agglomeration was seen on the sample surface. The samples prepared with the ultrasonic bath's intermediate stage have MWCNT with the same shape and original structure. Carbon nanotubes in this method of production do not have wall breakage middle stage. It was observed that the carbon nanotubes were well separated from each other, and crushing. Non-degradation of the nanotube structure will ensure that the electrical conductivity is maintained uniformly over a broader length and that the composite is more electrically homogeneous. Non-destruction and crushing of the wall of the multi-walled nanotubes in the sample with the intermediate stage of the ultrasonic bath reduced dislocation density. This reduction in dislocation density minimizes the electrical resistance of the sample [25, 26]. It should also be noted that with increasing MWCNT, the electrical conductivity increases as a result of reducing the level of insulated epoxy resin is reduced. This result has a good agreement with the result presented in the Ref. [21, 27-29].

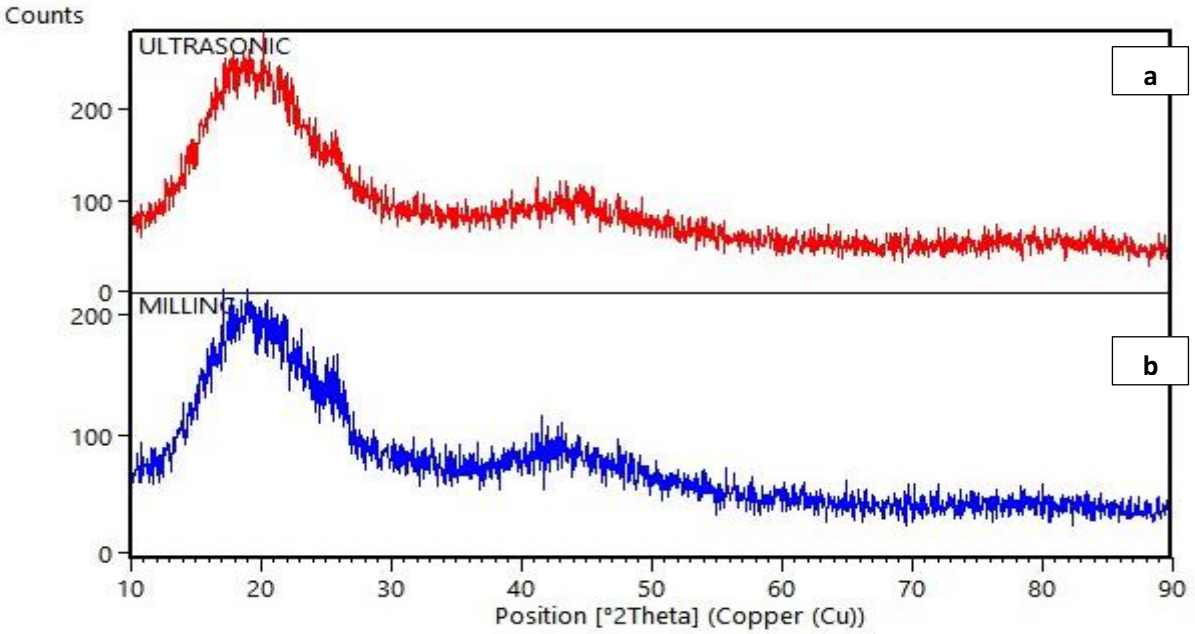

Fig. 3. XRD analysis of Epoxy resin-MWCNT composite: a) Ultrasonic method and b) Milling method

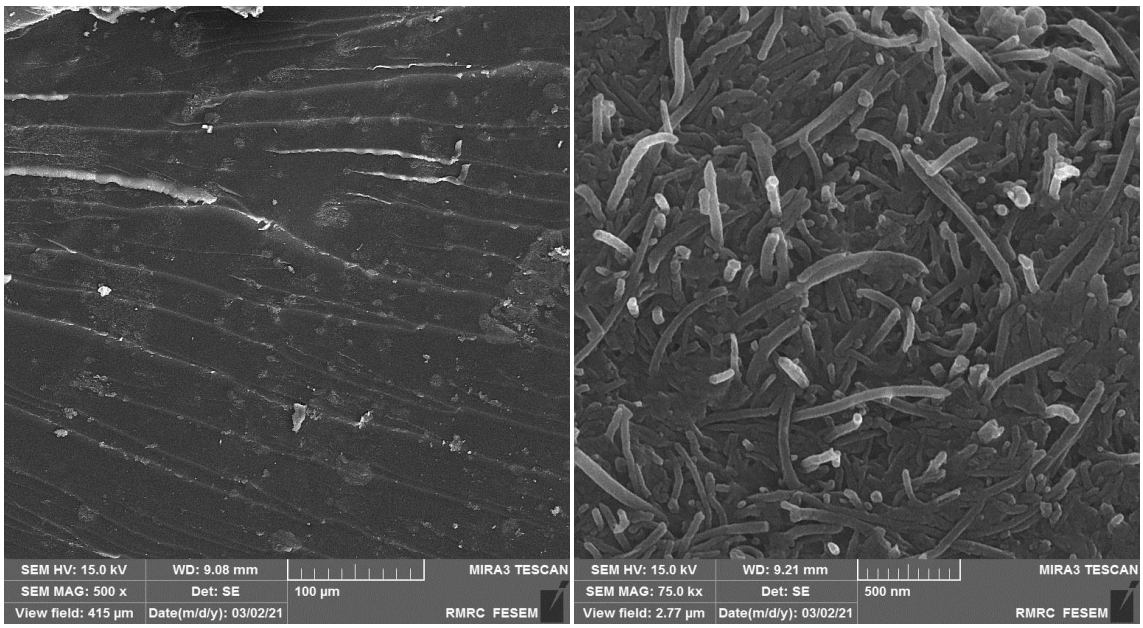

Fig. 4. SEM image of composite surface, epoxy resin-MWCNT with intermediate stage of ultrasonic bath

Figure 5 shows a scanning electron microscope image of the sample surface during the middle stage of the milling process. As seen in the image, the multi-walled carbon nanotubes are agglomerated and observed as an accumulation of nanotubes in the resin matrix. This occurred due to improper separation of the nanotubes by the middle stage of the mill process. Due to the successive blows of the steel bullets in the milling process, the image shows that the multi-walled carbon nanotubes suffered severe damage in structure and shape [30]. These damages can cause the composite's surface to not be fully integrated and homogeneous in electrical conductivity. Agglomeration can also severely affect the composite's electrical conductivity and eliminate electrical conductivity along the sample's entire length [30, 31].

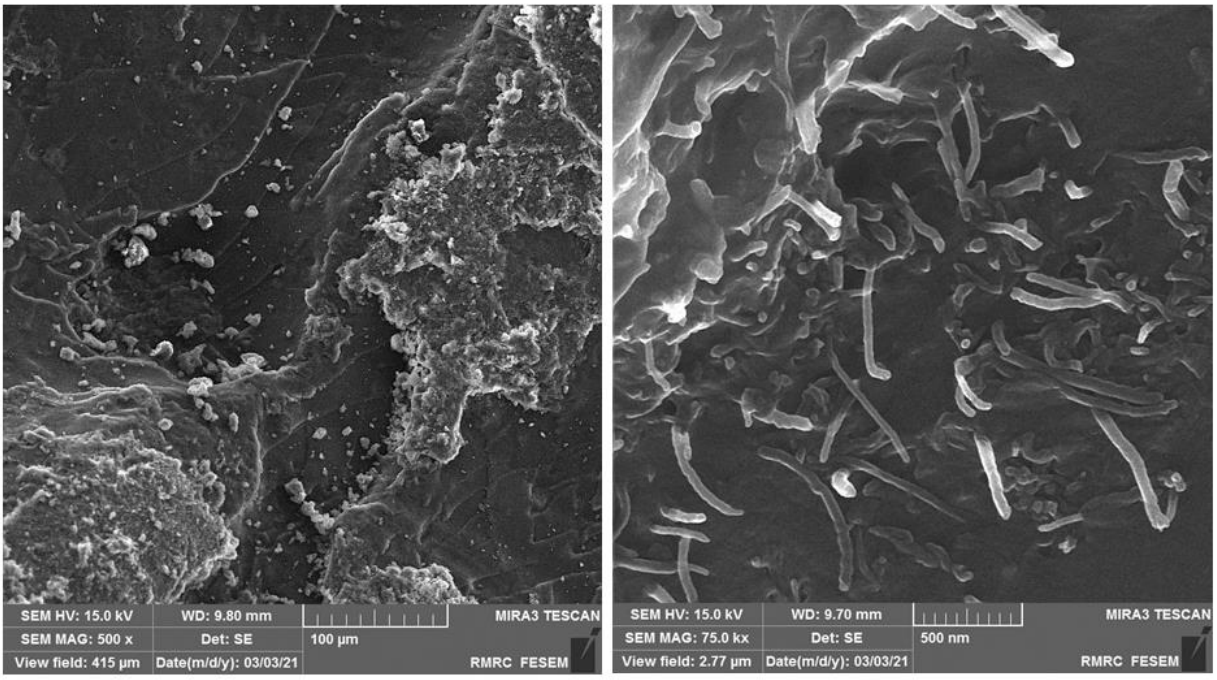

Fig. 5. SEM image of composite surface, epoxy resin-MWCNT with intermediate stage of milling process.

Figure 6 shows the results of the VSM test. In samples 6 (A) and 6 (B), epoxy resin and MWCNT composites with different intermediate stages underwent VSM testing, and it was observed that the results diagram was wholly changed and showed a soft magnetic material. Soft magnetic composite has properties well suited for absorbing magnetic waves, including meager coercive force, high permeability, high saturation of the core, and low residual magnetism. However, there is a slight difference between the two graphs. Figure 6 (A), which is related to the ultrasonic intermediate method, has a higher saturation magnet than 6 (B), which shows the hysteresis ring of the composite sample by the milling method. The reason for this saturation magnet is attributed to the uniform distribution of the MWCNT and lack of MWCNT agglomeration in the epoxy matrix after the milling process.

Figure 6 (C) shows that when the epoxy resin is placed in the magnetic field, its magnetic saturation is reduced, which reduces the absorption power of the magnetic part of the wave. It should be noted that magnetic and electric waves never exist alone, and the presence of each causes the emergence of the other. Since, in the VSM test, the field strength gradually increases and the epoxy resin is the only adsorbent of the electrical part of the wave, it is observed that the absorption of the magnetic part is significantly reduced. Then, when the presence of the field reaches zero, some magnetic residue is observed in the sample. The result revealed that the highest magnetic saturation at ($2500_{(Oe)}$) is related to the ultrasonic sample equal to ($0.1_{(emu/g)}$) and then for the milling sample ($0.075_{(emu/g)}$), and the lowest number is related to the epoxy resin sample with ($-0.01_{(emu/g)}$). As shown in the SEM images, the MWCNT distribution in the matrix of epoxy resin by the ultrasonic method is more uniform than in the milling method. This more uniform distribution and lack of MWCNT agglomeration in the epoxy matrix is the main reason for the higher saturation of the ultrasonic synthesized resin epoxy-MWCNT composite.

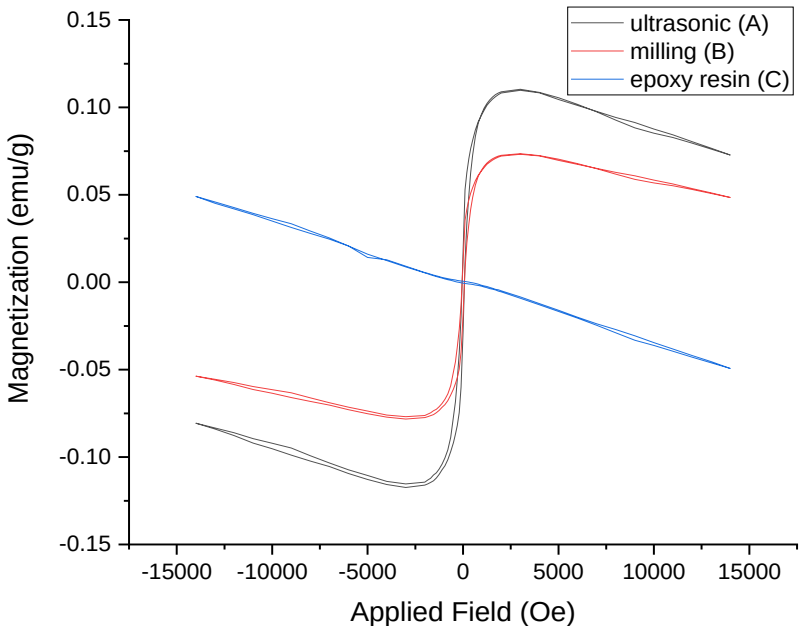

Fig. 6. VSM test results of composites produced, A) composites produced with ultrasonic bath's middle stage, B) composites produced with middle stage of milling process, C) Sample produced with epoxy resin without carbon nanotubes.

In order to investigate the absorption of electromagnetic waves, the reflection losses (RL) of the composites containing different amounts of carbon nanotube (0, 5, 10, 15, and 20 wt%) are shown in Figure 7. In this figure, the studied samples used ultrasonic waves to separate the carbon nanotubes. It was observed that the sample with 5 wt% of carbon nanotube has the highest reflection losses value. Also, this high RL value observed in the wide range between 9 to 11 GHz which is about -25 dB. It seems that increasing the concentration of carbon nanotubes by more than 5% by weight causes the nanotubes to not separate properly from each other. This unbalanced distribution of carbon nanotubes causes electrical conductivity not to be adequately maintained along the composite's entire length, which reduces the absorption of electromagnetic waves [32-34]. The 5 wt% sample mutation should be related to reaching the electrical conductivity threshold of epoxy resin–MWCNT nanocomposite [35]. Due to the proper distribution of carbon nanotubes in the resin matrix due to the separation of carbon nanotubes from each other by ultrasonic waves in the ultrasonic bath, the effective surface for magnetic wave absorption will increase. Proper distribution of nanotubes causes sequential reflections of electromagnetic waves in the resin epoxy-MWCNT nanocomposite [36].

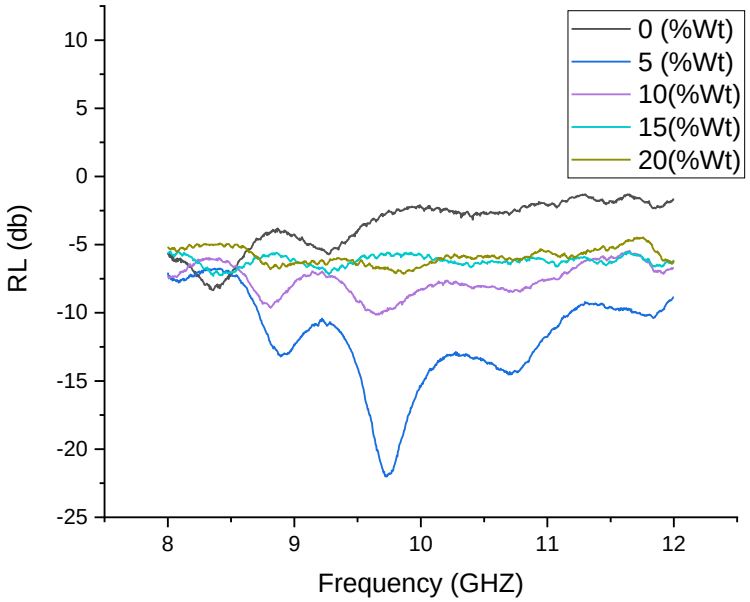

Fig. 7. The reflection losses of the composites containing different amounts of carbon nanotube produced with ultrasonic bath's middle stage: 0, 5, 10, 15, and 20 wt%

Carbon nanotubes will increase the electrical permeability of epoxy resin due to its very high electrical conductivity, which can help absorb electromagnetic waves [37-47]. Figure 8 shows the reflection losses (RL) of the composites containing different amounts of carbon nanotube produced with the middle stage of the milling process. As in Figure 8, all the produced composites showed a similar adsorption procedure in this diagram. However, the value of reflection losses of the produced composites by milling process is much lower than that of the samples with the intermediate ultrasonic bath process. Unlike the intermediate ultrasonic method, which had the highest adsorption at 5 wt%, the milling method had the highest RL value at 15 and 20 wt%. The impact of milling metal balls with carbon nanotubes in the milling method caused the carbon nanotubes to break. These collisions will shorten the length of the carbon nanotubes and break their walls. Reducing the nanotube walls' length and crushing will cause the nanotube network's integrity to be lost and cause the electrical conductivity not to form correctly.

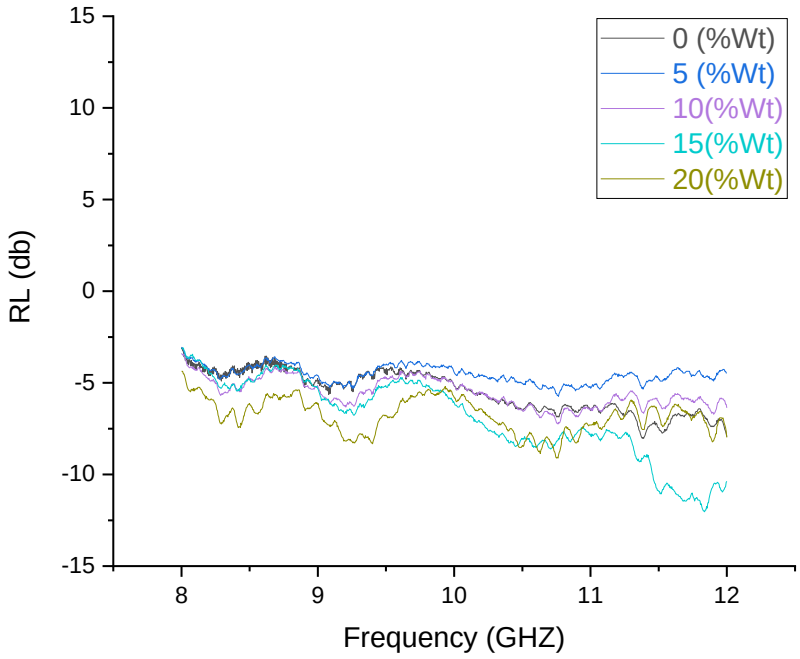

Fig. 8. The reflection losses of the composites containing different amounts of carbon nanotube produced with the middle milling stage: 0, 5, 10, 15, and 20 wt.%

4. Conclusions

According to the results obtained from the discussion and conclusion, it can be reported that:

1- The presence of compounds with two bands can help absorb the electrical part of the wave to absorb electromagnetic waves. In addition, the ultrasonic bath makes the MWCNT segregated more conveniently compared to the milling process.

2- Due to the absence of steel balls used in the milling process, the MWCNTs are not damaged in the ultrasonic intermediate process. Moreover, the production sample with the intermediate milling process causes areas with carbon nanotube agglomeration to be created.

3- The presence of carbon nanotubes that experienced mechanical damage and agglomeration reduces the electrical conductivity in the samples, which ultimately reduces the absorption of electromagnetic waves.

4- The highest reflection losses (RL) observed in the sample contains 5 wt.% carbon nanotubes, which were produced via the ultrasonic bath. Also, its maximum RL value range is 11-9 GHz and about -25 dB. Furthermore, the sample produced in the ultrasonic bath process has a higher magnetic saturation than in the milling process, which causes it to absorb more electromagnetic waves.

References

[1] J. Rushchitsky, Theory of waves in materials, ed., Bookboon, 2011.

[2] J. Cao, W. Fu, H. Yang, Q. Yu, Y. Zhang, S. Liu, P. Sun, X. Zhou, Y. Leng, S. Wang, B. Liu, G. Zou, "Large-scale synthesis and microwave absorption enhancement of actinomorphic tubular ZnO/CoFe2O4 nanocomposites". The Journal of Physical Chemistry B., Vol. 113, No. 14, 2009, pp. 4642-7.

[3] I.V. Shadrivov, M. Lapine, Y.S. Kivshar, Nonlinear, tunable and active metamaterials. Cham, Switzerland: Springer International Publishing; 2015.

[4] L. Peng, L. Li, R. Wang, Y. Hu, X. Tu, X. Zhong, " Microwave sintered Sr1− xLaxFe12− xCoxO19 (x= 0–0.5) ferrites for use in low temperature co-fired ceramics technology. Journal of Alloys and Compounds, Vol. 656, No. 2016, pp. 290-294.
[5] S. Lu, K. Ma, X. Wang, X. Xiong, W. Xu, C. Jia, " Fabrication and characterization of polymer composites surface coated Fe3O4/MWCNTs hybrid buckypaper as a novel microwave-absorbing structure. Journal of Applied Polymer Science, Vol. 132, No. 20, 2015, pp. 41974.
[6] I. Al Kawni, R. Garcia, S. Youssef, M. Abboud, J. Podlecki, R. Habchi, "Stabilization and encapsulation of magnetite nanoparticles", Materials Research Express, Vol. 3, No. 12, 2016, pp. 125024.
[7] N. Shiri, A. Amirabadizadeh, A. Ghasemi, "Influence of carbon nanotubes on structural, magnetic and electromagnetic characteristics of mnmgtizr substituted barium hexaferrite nanoparticles", Journal of Alloys Compounds, Vol. 690, No. 2017, pp. 759-764.
[8] X. Jian, B. Wu, Y. Wei, S.X. Dou, X. Wang, W. He, N. Mahmood, " Facile synthesis of Fe3O4/GCs composites and their enhanced microwave absorption properties. ACS Applied Materials & Interfaces, Vol. 8, No. 9, 2016, pp. 6101-6109.
[9] Z. Yan, J. Cai, Y. Xu, D. Zhang, "Microwave absorption property of the diatomite coated by Fe-CoNiP films". Applied Surface Science, Vol. 346, No. 2015, pp. 77-83.
[10] C.H. Papas, Theory of electromagnetic wave propagation, ed., Courier Corporation, 2014.
[11] M.F. Iskander, Electromagnetic fields and waves, ed., Prentice Hall, 1992.
[12] L.-F. Chen, C. Ong, C. Neo, V. Varadan, V.K. Varadan, Microwave electronics: Measurement and materials characterization, ed., John Wiley & Sons, 2004.
[13] X.C. Tong, Advanced materials and design for electromagnetic interference shielding, ed., CRC press, 2016.
[14] D. Micheli, C. Apollo, R. Pastore, M. Marchetti, "X-band microwave characterization of carbon-based nanocomposite material, absorption capability comparison and ras design simulation", Composites Science and Technology, Vol. 70, No. 2, 2010, pp. 400-409.
[15] X. Qi, Y. Deng, W. Zhong, Y. Yang, C. Qin, C. Au, Y. Du, "Controllable and large-scale synthesis of carbon nanofibers, bamboo-like nanotubes, and chains of nanospheres over Fe/SnO2 and their microwave-absorption properties". The Journal of Physical Chemistry C., Vol. 114, No. 2, 2010, pp. 808-814.
[16] M.-J. Park, J. Choi, S.-S. Kim, "Wide bandwidth pyramidal absorbers of granular ferrite and carbonyl iron powders", IEEE Transactions on Magnetics, Vol. 36, No. 5, 2000, pp. 3272-3274.
[17] E.F. Kuester, C.L. Holloway, "A low-frequency model for wedge or pyramid absorber arrays-i: Theory", IEEE Transactions on Electromagnetic Compatibility, Vol. 36, No. 4, 1994, pp. 300-306.
[18] C.L. Holloway, E.F. Kuester, "A low-frequency model for wedge or pyramid absorber arrays-ii: Computed and measured results", IEEE Transactions on Electromagnetic Compatibility, Vol. 36, No. 4, 1994, pp. 307-313.
[19] D.-A. Li, H.-B. Wang, J.-M. Zhao, X. Yang, "Fabrication and electromagnetic characteristics of microwave absorbers containing ppy and carbonyl iron composite", Materials Chemistry and Physics, Vol. 130, No. 1-2, 2011, pp. 437-441.
[20] A. Mandal, C.K. Das, " Effect of BaTiO3 on the microwave absorbing properties of Co-doped Ni-Zn ferrite nanocomposites ", Journal of Applied Polymer Science, Vol. 131, No. 4, 2014.
[21] Y. Zhai, Y. Zhang, W. Ren, "Electromagnetic characteristic and microwave absorbing performance of different carbon-based hydrogenated acrylonitrile–butadiene rubber composites", Materials Chemistry and Physics. Vol. 133, No. 1, 2012, pp. 176-181.
[22] T. Ting, Y. Jau, R. Yu, "Microwave absorbing properties of polyaniline/multi-walled carbon nanotube composites with various polyaniline contents", Applied Surface Science, Vol. 258, No. 7, 2012, pp. 3184-3190.
[23] B.Q.N. Bien Dong Che, Le-Thu T Nguyen, Ha Tran Nguyen, Viet Quoc Nguyen, Thang Van Le & Nieu Huu Nguyen "The impact of different multi-walled carbon nanotubes on the X-band microwave absorption of their epoxy nanocomposites", Chemistry Central Journal Vol. 9, No. 2015, pp.1-13.
[24] Z. Wu, S. Li, , M. Liu, Z. Wang and X. Liu,. Liquid oxygen compatible epoxy resin: Modification and characterization. RSC Advances, 2015, *5*(15), pp.11325-11333.
[25] S. Rathee, S. Maheshwari, A.N. Siddiquee, M. Srivastava, "A review of recent progress in solid state fabrication of composites and functionally graded systems via friction stir processing", J Critical Reviews in Solid State Materials Sciences, Vol. 43, No. 4, 2018, pp. 334-366.
[26] H. Li, A. Misra, Z. Horita, C.C. Koch, N.A. Mara, P.O. Dickerson, Y. Zhu, "Strong and ductile nanostructured cu-carbon nanotube composite", J Applied Physics Letters, Vol. 95, No. 7, 2009, pp. 071907.
[27] S. Barrau, P. Demont, E. Perez, A. Peigney, C. Laurent, C.J.M. Lacabanne, "Effect of palmitic acid on the electrical conductivity of carbon nanotubes−epoxy resin composites", Macromolecules. Vol. 36, No. 26, 2003, pp. 9678-9680.

[28] J. Sandler, M. Shaffer, T. Prasse, W. Bauhofer, K. Schulte, A.J.P. Windle, "Development of a dispersion process for carbon nanotubes in an epoxy matrix and the resulting electrical properties", Polymer. Vol. 40, No. 21, 1999, pp. 5967-5971.
[29] Y.S. Song, J.R.J.C. Youn, "Influence of dispersion states of carbon nanotubes on physical properties of epoxy nanocomposites", Carbon. Vol. 43, No. 7, 2005, pp. 1378-1385.
[30] H. Zhuang, G. Zheng, A. Soh, "Interactions between transition metals and defective carbon nanotubes", J Computational Materials Science, Vol. 43, No. 4, 2008, pp. 823-828.
[31] H. Kaurav, S. Manchanda, K. Dua, D.N. Kapoor, "Nanocomposites in controlled & targeted drug delivery systems", Proc. Nano Hybrids and Composites, 2018, pp. 27-45.
[32] J. Hernández, M.C. García-Gutiérrez, A. Nogales, D.R. Rueda, M. Kwiatkowska, A. Szymczyk, Z. Roslaniec, A. Concheso, I. Guinea, T.A. Ezquerra, "Influence of preparation procedure on the conductivity and transparency of swcnt-polymer nanocomposites", J Composites Science Technology, Vol. 69, No. 11-12, 2009, pp. 1867-1872.
[33] J. Li, P.C. Ma, W.S. Chow, C.K. To, B.Z. Tang, J.K. Kim, "Correlations between percolation threshold, dispersion state, and aspect ratio of carbon nanotubes", J Advanced Functional Materials, Vol. 17, No. 16, 2007, pp. 3207-3215.
[34] J. Aguilar, J. Bautista-Quijano, F.J.E.P.L. Avilés, "Influence of carbon nanotube clustering on the electrical conductivity of polymer composite films", Express Polym Lett. Vol. 4, No. 5, 2010, pp. 292-299.
[35] A.P. Singh, P. Garg, F. Alam, K. Singh, R. Mathur, R. Tandon, A. Chandra, S. Dhawan, "Phenolic resin-based composite sheets filled with mixtures of reduced graphene oxide, γ-Fe2O3 and carbon fibers for excellent electromagnetic interference shielding in the x-band", Carbon, Vol. 50, No. 10, 2012, pp. 3868-3875.
[36] H.-B. Zhang, Q. Yan, W.-G. Zheng, Z. He, Z.-Z. Yu, "Tough graphene− polymer microcellular foams for electromagnetic interference shielding", ACS Applied Materials & Interfaces, Vol. 3, No. 3, 2011, pp. 918-924.
[37] G. De Bellis, A. Tamburrano, A. Dinescu, M.L. Santarelli, M.S. Sarto, "Electromagnetic properties of composites containing graphite nanoplatelets at radio frequency", Carbon, Vol. 49, No. 13, 2011, pp. 4291-4300.
[38] P. Bhattacharya, C.K. Das, S.S. Kalra, "Graphene and mwcnt: Potential candidate for microwave absorbing materials", Journal of Materials Science Research, Vol. 1, No. 2, 2012, pp. 126.
[39] S.u.D. Khan, M. Arora, M.A. Wahab, P. Saini, "Permittivity and electromagnetic interference shielding investigations of activated charcoal loaded acrylic coating compositions", Journal of Polymers, Vol. 2014, No. 2014, Article ID 193058.
[40] A. Gharieh, M.S. Seyed Dorraji, "A systematic study on the synergistic effects of mwcnts and core–shell particles on the physicomechanical properties of epoxy resin", Scientific Reports. Vol. 11, No. 1, 2021, pp. 1-11.
[41] G. Hu, W. Fu, Y. Ma, J. Zhou, H. Liang, X. Kang, X.J.M. Qi, "Rapid preparation of MWCNTS/epoxy resin nanocomposites by photoinduced frontal polymerization", Materials. Vol. 13, No. 24, 2020, pp. 5838.
[42] S. Roy, R.S. Petrova, S.J.N.r. Mitra, "Effect of carbon nanotube (CNT) functionalization in epoxy-CNT composites", Nanotechnology reviews, Vol. 7, No. 6, 2018, pp. 475-485.
[43] M. Yazdi, V.H. Asl, M. Pourmohammadi, H. Roghani-Mamaqani, "Mechanical properties, crystallinity, and self-nucleation of carbon nanotube-polyurethane nanocomposites", Polymer Testing. Vol. 79, No. 2019, pp. 106011.
[44] M. Haghgoo, R. Ansari, M.J.C.P.B.E. Hassanzadeh-Aghdam, "Prediction of electrical conductivity of carbon fiber-carbon nanotube-reinforced polymer hybrid composites", Composites Part B: Engineering. Vol. 167, No. 2019, pp. 728-735.
[45] M.A. Zhilyaeva, E.V. Shulga, S.D. Shandakov, I.V. Sergeichev, E.P. Gilshteyn, A.S. Anisimov, A.G. Nasibulin, "A novel straightforward wet pulling technique to fabricate carbon nanotube fibers", Carbon. Vol. 150, No. 2019, pp. 69-75.
[46] H. Jintoku, Y. Matsuzawa, M.J.C. Yoshida, "Dual use of anionic azobenzene derivative as dispersant and dopant for carbon nanotubes for enhanced thermal stability of transparent conductive films", Carbon. Vol. 152, No. 2019, pp. 247-254.
[47] J. Pan, L.J.M.C. Bian, Physics, "A physics investigation for influence of carbon nanotube agglomeration on thermal properties of composites", Materials Chemistry and Physics. Vol. 236, No. 2019, pp. 121777.

JMATPRO	Journal of Advanced Materials and Processing 10 (1): 13-26, Winter 2022 http://jmatpro.iaun.iau.ir 20.1001.1.2322388.2022.10.1.2.5

Research Paper

Development and Evaluation of Nanomagnetic Carrier for the Controlled Loading and Release of Celecoxib

Shabnam Ahmadvand [1], Maryam Kargar Razi[1*], Babak Sadeghi [2], Seyedeh Sara Mirfazli [3]

1. Department of Chemistry, Islamic Azad University, North Tehran Branch, Tehran, Iran
2. Department of Chemistry, Islamic Azad University, Tonekabon Branch, Tonekabon, Iran
3. Department of Medicinal Chemistry, School of Pharmacy International Campus, Iran University of Medical Sciences, Tehran, Iran

ARTICLE INFO

Article history:

Received 22 October 2021
Accepted 19 December 2021
Available online 1 January 2022

Keywords:
Dynamic Light Scattering (DLS)
Magnetite
Nanocomposite
Celecoxib
TGA

ABSTRACT

The aim of the present study was to develop synthesize, characterize, and find many applications of functionalized metal oxide nanoparticles. Herein, a new strategy is developed to functionalize magnetite nanoparticles to improve their performances of cerium oxide-functionalized Fe_3O_4@SiO_2@CeO_2 magnetic nanoparticles (FSC). In this study, after preparing optimized FSC, characterization and identification of their chemical structure were carried out by FT-IR, FESEM, VSM, TGA, DLS, and XRD. Afterward, the functionalized nanoparticles were examined in the delivery of celecoxib as an active drug model involving cerium oxide and hydroxyl functional groups. The results with respect to particle size, present investigation indicate that the formulations (m_{FSC}=5 mg, pH=3.3) can be considered as best among various formulations. Dynamic light scattering (DLS) techniques used to measure particle size and zeta potential distribution revealed successful preparation of an Fe_3O_4@SiO_2@CeO_2 nanocomposite prepared on Fe_3O_4@SiO_2 (FS), with a hydrodynamic size distribution of 45 nm.

Citation: Ahmadvand, Sh.; Kargar Razi, M.; Sadeghi, B.; Mirfazli, S.S. (2022) Development and Evaluation of Nanomagnetic Carrier for the Controlled Loading and Release of Celecoxib, Journal of Advanced Materials and Processing, 10 (1), 13-26. Dor: 20.1001.1.2322388.2022.10.1.2.5

[*] **Corresponding Author.**
E-Mail Address: m_kargarrazi@iau-tnb.ac.ir

1. Introduction

In regeneration, nanomaterials with biomaterials are offer ways to control surface and mechanical properties. Moreover, it increases cellular adhesion, differentiation, and integration of stem cells into the environment around us. Finally, the additional possibilities of increasing the biological performance of biomaterials are because of the drug delivery capabilities of nanoparticles [1].

The use of nanotechnology to improve current approaches in tissue and organ regeneration has received increased attention over the years owing to the great versatility that they offer in terms of size and surface chemistry, allowing the utilization as carriers for the delivery of drugs, genetic material, or growth factors (GFs). Indeed, various nanoparticles have been developed for therapy; these include dendrimers, liposomes, polymer-based nanoparticles, micelles, carbon nanotubes, and many more [2]. The slower transit times exhibit regarding nanoparticulate oral delivery systems than larger-sized particles in various dosage forms, increasing the local concentration gradient across absorptive cells, thereby enhancing local and systemic delivery of both free and bound drugs across the gut [3].

A number of biocompatible carrier systems involving large surface areas and tailorable pore size are introduced for drug delivery, such as calcium phosphate cement [4], organic polymers [5], various inorganic composites [6], metal-organic frameworks [7], and nanoporous silica [8, 9].

In regeneration, nanoparticles improve biomaterials' regenerative capabilities, offering ways to control surface and mechanical properties. Moreover, the incorporation of nanoparticles within biomaterials increases cellular adhesion, differentiation, and integration of stem cells into the surrounding environment [10]. Inevitably, the release rate of drugs can be affected by important parameters such as pores size and functional groups anchored to the surface of the carrier [11]. The modification in the surface and properties could be effective [12] and make the pores interact with drugs and control drug delivery processes [13]. Magnetic iron oxide nanoparticles with a large surface area, due to their multifunctional properties, superparamagnetism, and low toxicity, have been known as potential carriers in drug delivery for applications in medicine and biology [14-16]. The purpose of this investigation is to construct developed a new strategy to functionalize Fe_3O_4 by CeO_2 and well-ordered magnetic core/mesoporous shell $Fe_3O_4@SiO_2$ spheres. Then, the fabricated nanocarrier was used for the promising delivery of celecoxib as a model antiviral drug [17-20]. Influences of the type and concentration of the surfactant, pH, contact time, and temperature on the loading/release of celecoxib, loading capacity, and in vitro potential for drug adsorption enhancement of $Fe_3O_4@SiO_2@CeO_2$ magnetic nanoparticles (FSC) are systematically investigated.

2. Experimental

2.1. Methods and Materials

All chemicals were received from commercial resources (Merck and Chem Lab) and utilized without further refinement. Field emission scanning electron microscope (FESEM) micrographs were taken by applying an LEO 440i (acceleration speed voltage 26 kV). FT-IR spectra were recorded on a Bomem MB100. These measurements were carried out at a resolution of 4 cm^{-1} in KBr pellets. The pellets have been used for FTIR spectroscopy measurement.

The particle size of HA/casein nanoparticles was measured using Dynamic Light Scattering (DLS) technique (ZS/ZEN3600 Zeta sizer; Malvern, Instruments Ltd, Malvern, UK). The crystalline structure of the samples was assessed by X-ray diffraction (XRD) analysis on a Seisert Argon 3003 PTC using nickel filtered XD-3Cu Ka radiations (k = 1.5418 A). A freeze dryer, Model FD-10, Pishtaz Equipment Engineering Co, Iran, was applied for drying of the prepared nanomaterials. Fe_3O_4 and $Fe_3O_4@SiO_2@CeO_2$ nanocomposites were synthesized by the introduced single-step solvothermal method with a few modifications [20-22].

2.2. Preparation

Fe_3O_4 nanoparticles were prepared similar to the method reported in several studies [20-22]. $FeCl_3.6H_2O$ (2.2 g), $NaNO_3.3H_2O$ (0.42 g), PEG-400 (53 ml), and 6 ml ethanol were mixed under intense stirring at 25 °C for 40 min. Then, 3 g of NaAc was added, and the resulting was mixed under intense stirring at 25 °C for 14 h. After that, the mixture was put on a stainless steel autoclave (with Teflon-lined) of 60 ml volume. Eventually, the autoclave was warmed and retained at 190 °C for 12 h, and afterward, it was chilled off to room temperature. The particles were washed three times with absolute ethanol and were dried by a rotary evaporator [18].

A one-step synthesis was used to obtain silica-coated Fe_3O_4 nanoparticles. 0.15 g of Fe_3O_4 was dispersed in a mixture containing distilled water (3 ml), absolute ethanol (7 ml), and ammonia (0.3 ml, 25%) with sonication for 40 min. Then, the reaction mixture was conducted with 0.7 ml *cetyltrimethylammonium bromide (CTAB)* and was stirred for 20 h. Then, the precipitate (black color) was filtered and well dried.

2.3. Surface modification of the prepared nanomaterial

Fe_3O_4@SiO_2 (0.06 g) was spread out in 2.2 ml of dry toluene by ultrasonication for 25 min under N_2. Then, 0.06 ml of CeO_2/CTAB was joined and was refluxed under nitrogen for 20 h. After completion of the reaction, the resulting Fe_3O_4@SiO_2@CeO_2 magnetic nanoparticles (FSC) were isolated by filtration, washed with acetone, and dried at room temperature [19-20]. All materials were used directly without any further purification.

2.4. Particle size and zeta potential distributions

The size distribution and particle size of the FSC/drug were characterized by photon correlation spectroscopy (PCS) using a Zetasizer 2300 Malvern Instruments, UK. This solution (including FSC/drug) was diluted with filtered (0.32μm) with ultra-pure water and analyzed using Zetasizer. The surface charge was determined using an aqueous dip cell in an automatic mode by placing diluted samples (with ultra-purified water) in the capillary measurement cell, and the cell position was adjusted [23-25]. The particle size of HA/casein nanoparticles was measured using Dynamic Light Scattering (DLS) technique (ZS/ZEN3600 Zeta sizer; Malvern, Instruments Ltd, Malvern, UK).

2.5. Loading and release studies of Celecoxib

The Celecoxib loading was studied by adding FSC (0.005 g) into a phosphate buffer (5 ml, pH 3.3) containing celecoxib (0.07 mM in ethanol) with magnetic stirring at ٤٠ °C for ٤ h. Then, the mixture was isolated via an external magnet and was utilized for measuring the drug loading amount. To remove the unloaded celecoxib, the precipitate was re-dispersed in ٤ ml of the above buffer (Schematic 1). Uv-Vis quantified the free-celecoxib content at 253 nm. The amount of the loaded drug was calculated by Eq. (1) [26].

Loading content = M_0-M_t /M_N × 100 % Eq. (1)

Here, M_0 and M_t are the amounts of celecoxib in the primary and filtered solutions, respectively. M_N is the amount of FSC used for the loading process.

To determine the amount of the drug adsorbed after 120 min, 8, 24, and 48 h, 1 ml of the above solution was replaced with a fresh buffer solution and was analyzed by UV-Vis [27]. The loading process would be achieved via the hydrogen bonding interactions of the hydroxyl groups of celecoxib with the surface amino groups of FSC. To study the impact of drying conditions on the loading efficacy of the modified nanomaterial; the prepared final compound was dried under freeze conditions. Results showed only a little enhancement in the loading capacity compared with the one dried under usual thermal conditions.

This system was equipped with a 4 mV helium/neon laser at 633 nm wavelength and measured the particle size with the noninvasive backscattering technology at a detection angle of 173° after at least 100-fold dilution with purified water. The DLS measurements were performed at 25.0 ± 0.1 °C at 20-second intervals for three repeat measurements. Each diluted nanoparticle suspension was put in a universal folded capillary cell equipped with platinum electrodes for zeta potential measurement. The electrophoresis mobility was measured and the zeta potential (ζ) was calculated by the Dispersion Technology Software provided by Malvern.

Aliquots of 1 ml were withdrawn at pre-determined time intervals and immediately replaced by the same volume of the fresh medium. The aliquots were suitably diluted with the dissolution medium and analyzed by UV-Vis Spectrophotometer at the appropriate wavelength. Stability studies of prepared FSC nanoparticles were carried out by storing optimized formulation at 25 ± 1 °C and 40 ± 2 °C for 90 days. The samples were analyzed at 1-3 months for their drug content, drug release rate ($t_{50\%}$) as well as any changes in their physical appearance (ICH Q1A (*R*2) 2003) [28].

3. Results and discussion

Fig. 1a, b shows the FT-IR spectra of celecoxib, FSC, and celecoxib-loaded Fe_3O_4@SiO_2@CeO_2. The reaction of hydroxyl groups on the surface of Fe_3O_4@SiO_2 with the ethoxy groups of trimethoxysilylpropylamine ended in the formation of a novel carrier system. The bands at ٦48, 940, and 1069 cm^{-1} are attributed to the Fe-O, Si-O-H, and, Si-O-Si vibrations, respectively. The bands at 648 cm^{-1} in the FT-IR spectrum were ascribed to Ce–O stretching vibration, which corroborated that it is cross to the surface of nanomagnetic material. The grafted Ce–O groups at the surface of FSC formed H-bond with the oxygen atoms of celecoxib, causing the drug molecules to settle down onto the carrier surface Fig. 1a [29-30].

According to the chemical structure of celecoxib, the presence of S=O stretching vibration at 1339 cm^{-1}, together with aliphatic C–H stretching vibrations in 2925–2986 cm^{-1} for the alkyl groups confirmed loading of the celecoxib. Moreover, the bands at 1090, 1437, and 1561 cm^{-1} are assigned to C-N, C-H, and N-H bending vibrations, respectively Fig. 1b.

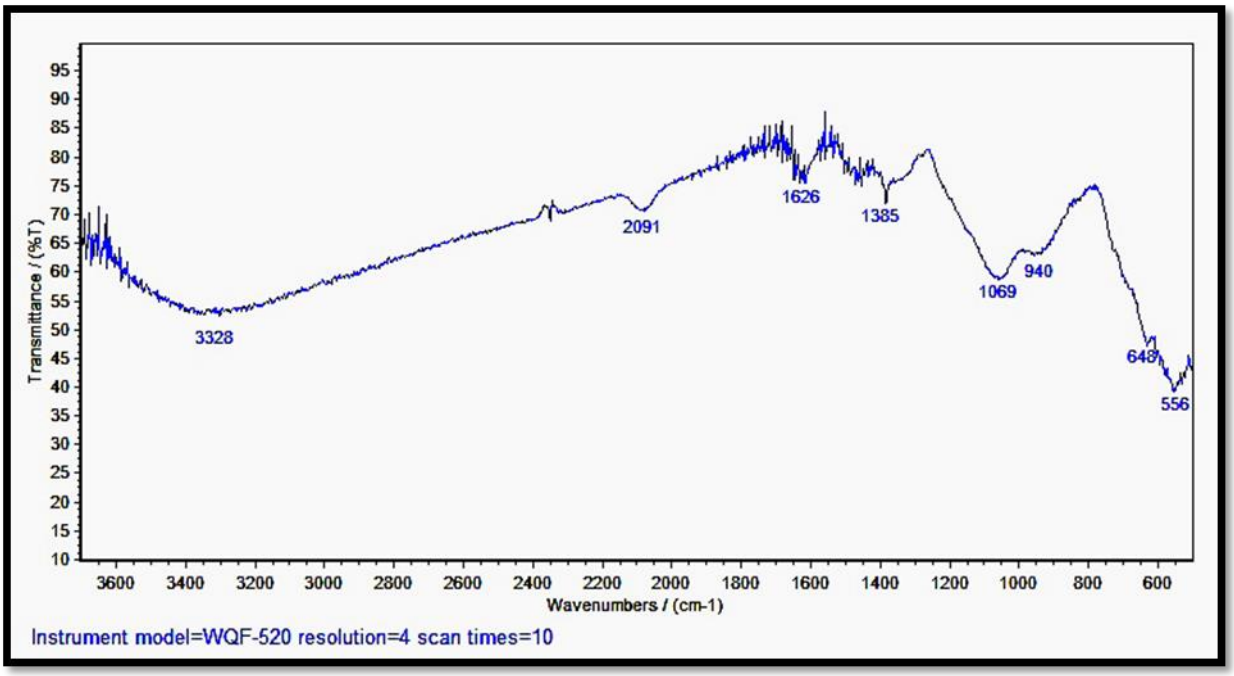

a)

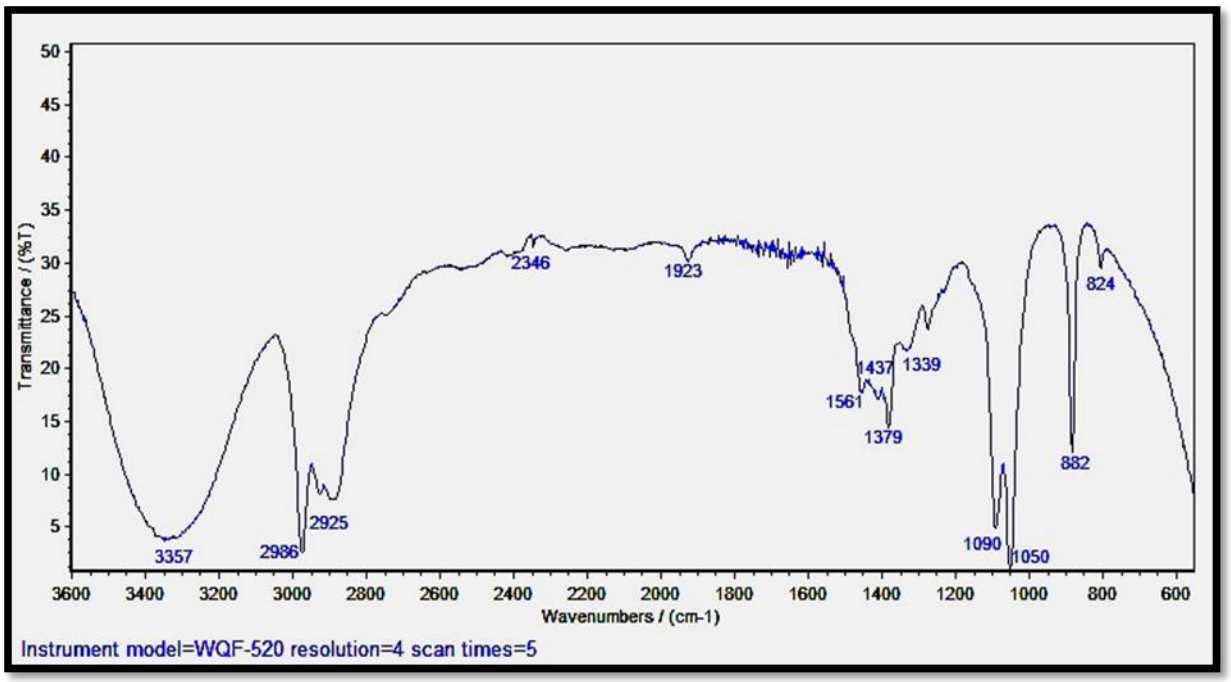

b)

Fig. 1. FT-IR spectra of FSC (a), and celecoxib loaded Fe_3O_4@SiO_2@CeO_2 (b).

The XRD patterns for Fe_3O_4 and drug-loaded Fe_3O_4@SiO_2@CeO_2 (FSC) are depicted in Fig. 2. It is assigned that the relative intensities and positions of the reflection peaks for Fe_3O_4 nanoparticles agree well with the standard diffraction card JCPDS 12882-54552. Comparing the XRD pattern of initial Fe_3O_4 nanoparticles to the modified one displayed that the pores remained intact after functionalization (Fig. 3) [31]. The attendance of a distinct peak at nearly 2θ = 25-35°, which matches with the reported ones, authenticated that the pores retained after functionalization and the structure of magnetite remained intact after drug loading.

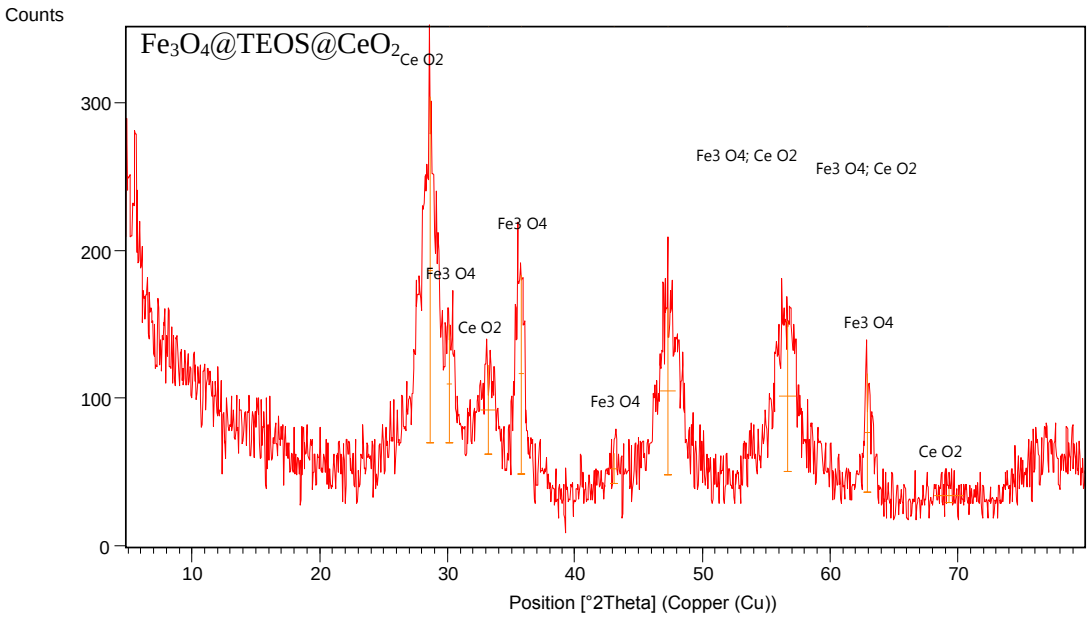

Fig. 2. XRD pattern of $Fe_3O_4@SiO_2@CeO_2$ (FSC) nanocomposite.

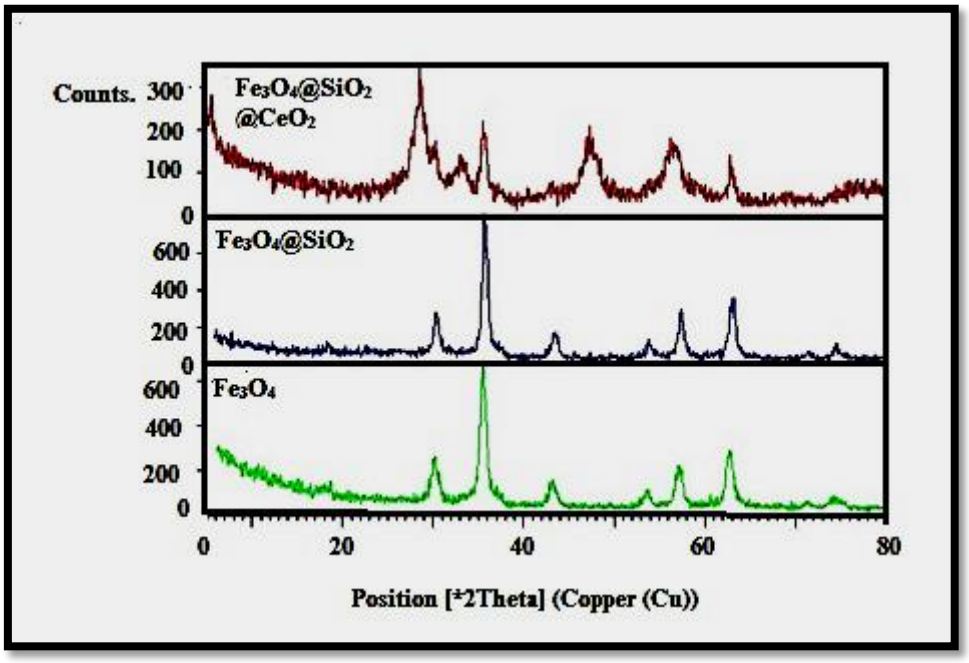

Fig. 3. Compare the resulting pattern XRD pattern of Fe_3O_4, $Fe_3O_4@SiO_2$ (FS), $Fe_3O_4@SiO_2@CeO_2$ (FSC) nanocomposite.

Zetasizer analyzed the particle size of Celecoxib/FSC nanoparticles loaded. EDX spectroscopic results related to the FSC nanocomposite coating containing cerium oxide and silica are reported in Fig. 4. The EDX spectrum of this nanocomposite shows the presence of Fe, Si, Ce, O, C elements. X-ray diffraction analysis and the presence of corresponding peaks confirm the presence of cerium and silica nanoparticles in this nanocomposite. The Z-particle size (r.nm) of Celecoxib/FSC nanoparticles formulations ranged from 2.9 to 13.3 nm, as shown in Table 1. Particle size and zeta potential result revealed that all nanoformulation were within the range of 2.9 to 13.3 nm, with the slight negative in charge.

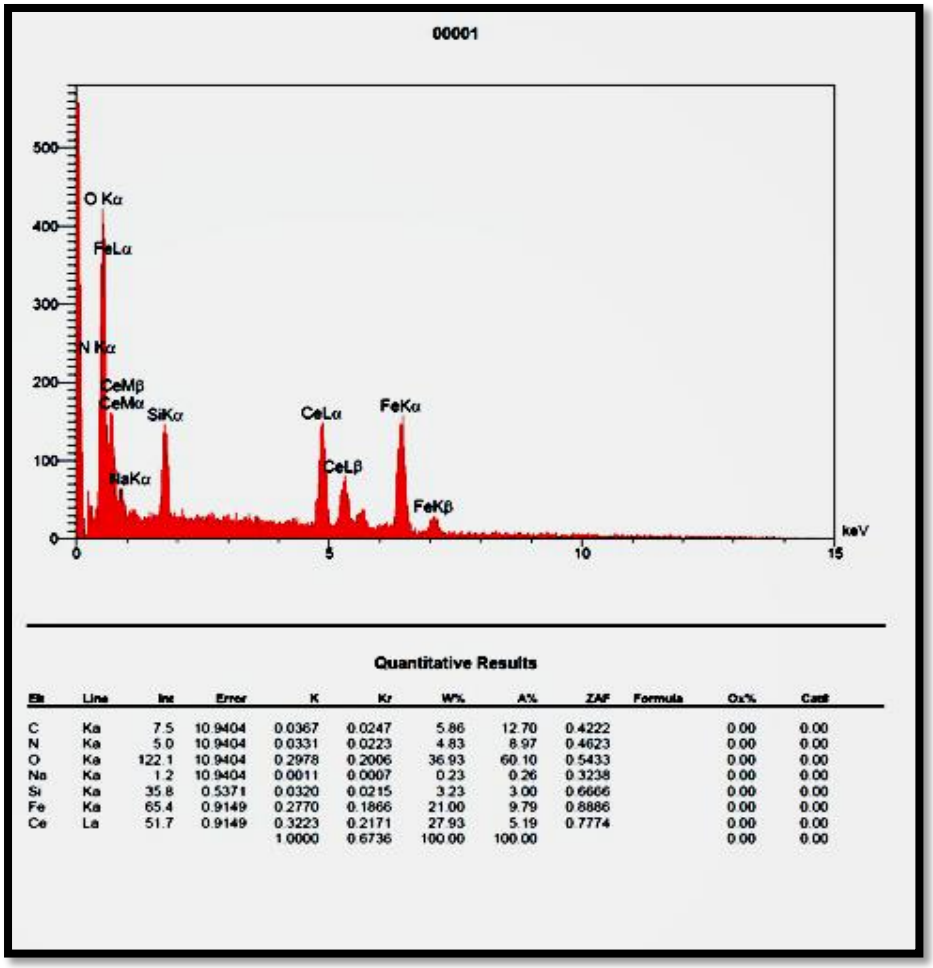

Fig. 4. Spectrum of EDX and size distribution of Fe_3O_4@SiO_2@CeO_2 (FSC) anocomposite.

Table 1. Evaluation of particle size and zeta potential.

Formulation	Particle Size		Zeta Potential (mV)
	Size (r.nm)	Mean Intensity (%)	
FSC	2.903	41.8	-5.17
	4.128	58.2	
FSC	11.157	31.7	-6.18
	13.30	68.3	

In this respect, the dimensions (size and surface) characteristics of nanoparticles are of prime importance. Particles of 50 nm diameter with hydrophilic surfaces have a longer circulation in the blood and increase the targeting efficiencies to specific sites [28-29]. The electric charge present on the FSC nanoparticles was evaluated by measuring the zeta potential. The zeta potential of FSC nanoparticles was in the range of -6.18 to -5.17 mV (Table 1) which indicates no agglomeration, meanwhile with moderate stability.

Scanning electron microscopy micrograph of optimized Celecoxib/FSC nanoparticles showed that the particles have a smooth surface and they are uniformly and spherically distributed (Fig. 5). The size and morphology of Fe_3O_4 and FSC were further studied with FESEM. Fig. 5 describes that Fe_3O_4 nanoparticles were semi-spherical in shape; therefore, the prepared Fe_3O_4 nanoparticles by solvothermal method resulted in uniform sizes with good dispersibility. The images dispersion of transmission electron microscopic (TEM) of FSC nanoparticulate (Fig. 6) further confirms the spherical shape of nanoparticles with less or no aggregation. The average grain size obtained by XRD via the Scherrer equation for Fe_3O_4 (<30 nm) was in good agreement with the results obtained by FESEM (<25 nm). The FESEM images for FSC nanocomposites before and after drug loading confirmed that the semi-spherical shape of the nanoparticles was unchanged and no observable change in morphology of the nanoparticles occurred.

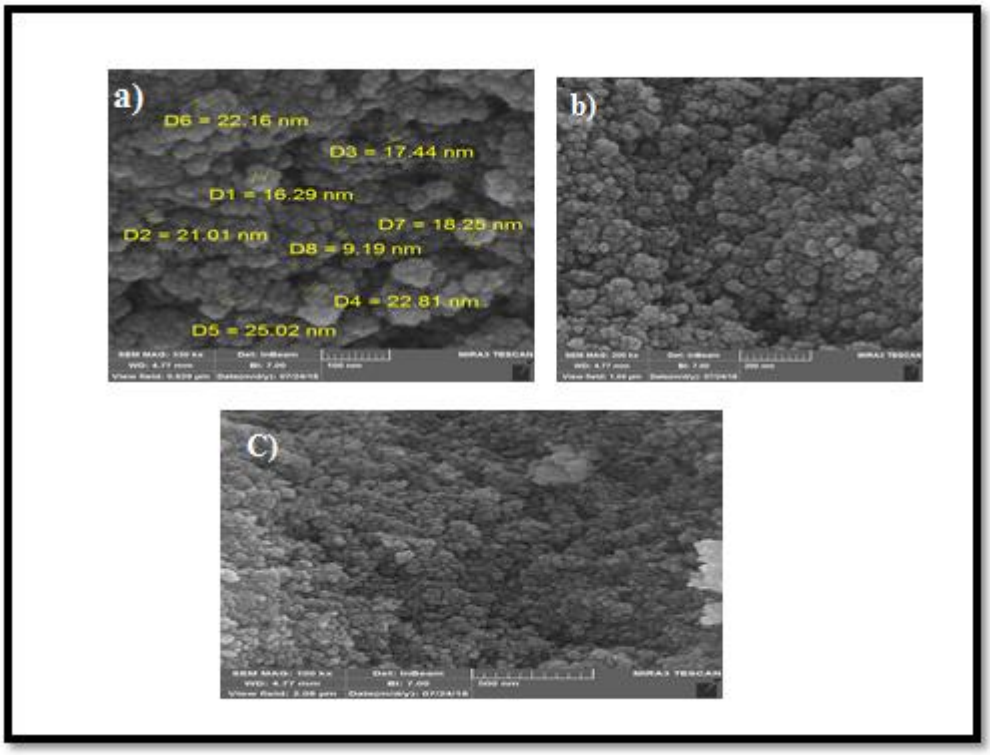

Fig. 5. FESEM images of the FSC with resolution of (a) 100 nm, (b) 200 nm, (c) 500 nm.

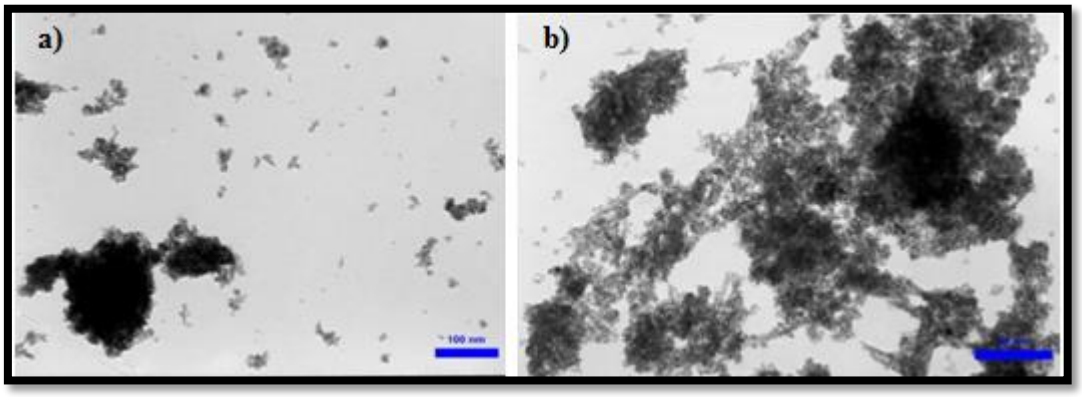

Fig. 6. (a, b). TEM images of the Fe_3O_4@SiO_2@CeO_2 (FSC).

Considering the d-orbital of Ce and the influence of hydrogen bonding on the loading of the drug onto the pores of the modified nanomagnetic material, further studies were outlined to clarify loading and release efficacies. The pH, loading time, and temperature seem to be the main parameters on the celecoxib loading.

The impact of pH on celecoxib loading was investigated using a variety of pHs ranging from acidic to basic. As Fig. 7 shows, for the increments of the hydrogenic interactions in an alkaline pH, the best loading can be achieved at pH 3.3. The decrease in loading was observed at high alkaline pH (>7) merely due to the hydrolysis of Fe–O–Si and C-O-Si bands and demolition of the bind to the agent. The loading temperature was also screened on the drug loading capacity. Findings displayed that by enhancing temperature, the drug loading improves. This phenomenon can be attributed to decreasing desorption because of the hydrogenic interactions by raising temperature [32]. The effect of time on the loading of celecoxib onto FSC was also investigated.

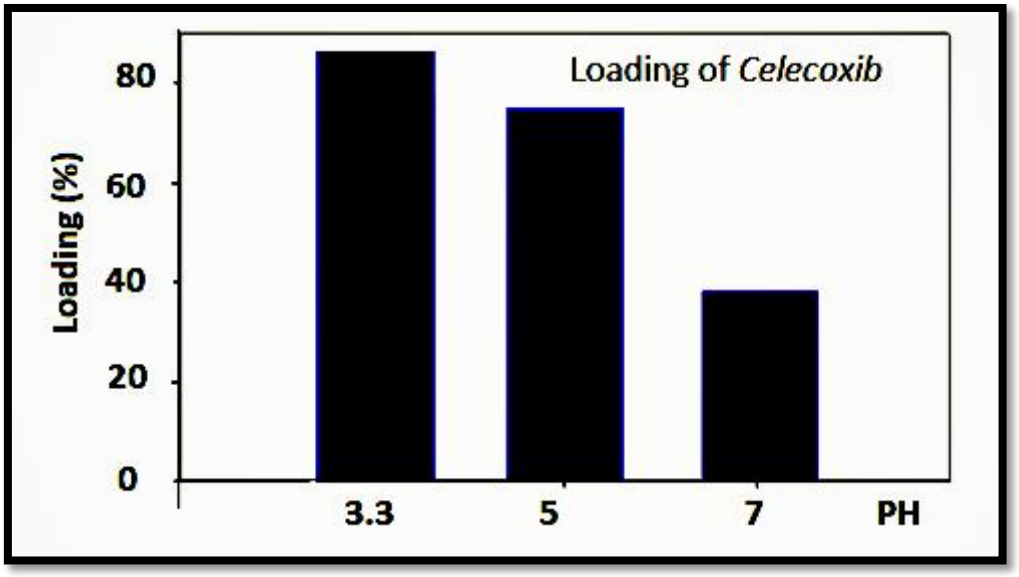

Fig. 7. Effect of pH on loading of celecoxib onto FSC.

Dynamic light scattering (DLS) is a valuable tool for studying size and degree of agglomeration of the nanoparticles as a function of time in the suspension solution. In this technique, one can determine the hydrodynamic size of the nanoparticles by measuring the intensity of laser scattered light that passes through a colloidal solution. Larger particles will diffuse slower than smaller particles. So, particle size can be mathematically provided by measuring the time dependence of the scattered light. The DLS experimental data obtained in this work which is given in Fig.8, shows a zeta particle size distribution of 45 nm. In fact, this is the average particle size of the FSC nanocomposite prepared on $Fe_3O_4@SiO_2$ (FS). The zeta-potential (Fig. 9)of the particles, which is a basic parameter in controlling the stability of colloidal suspensions, is obtained by measuring particles mobility under an applied electric field which is applied and can be calculated using the Smoluchowski equation [33]:

$$\zeta = \frac{\eta}{\varepsilon_0.\varepsilon_r}\ U \qquad (2)$$

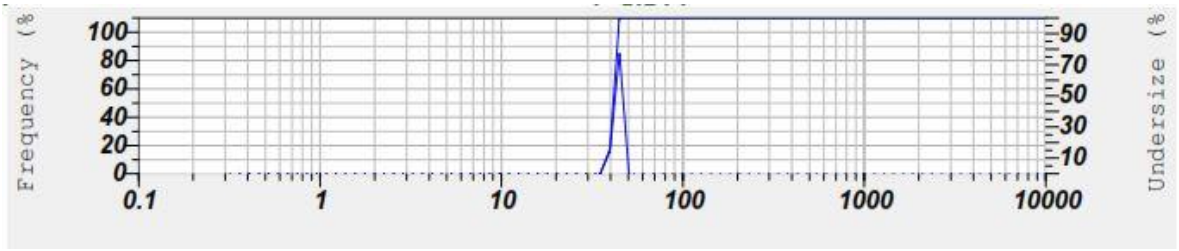

Fig. 8. DLS measured results for FSC nanocomposite prepared on $Fe_3O_4@SiO_2$ (FS).

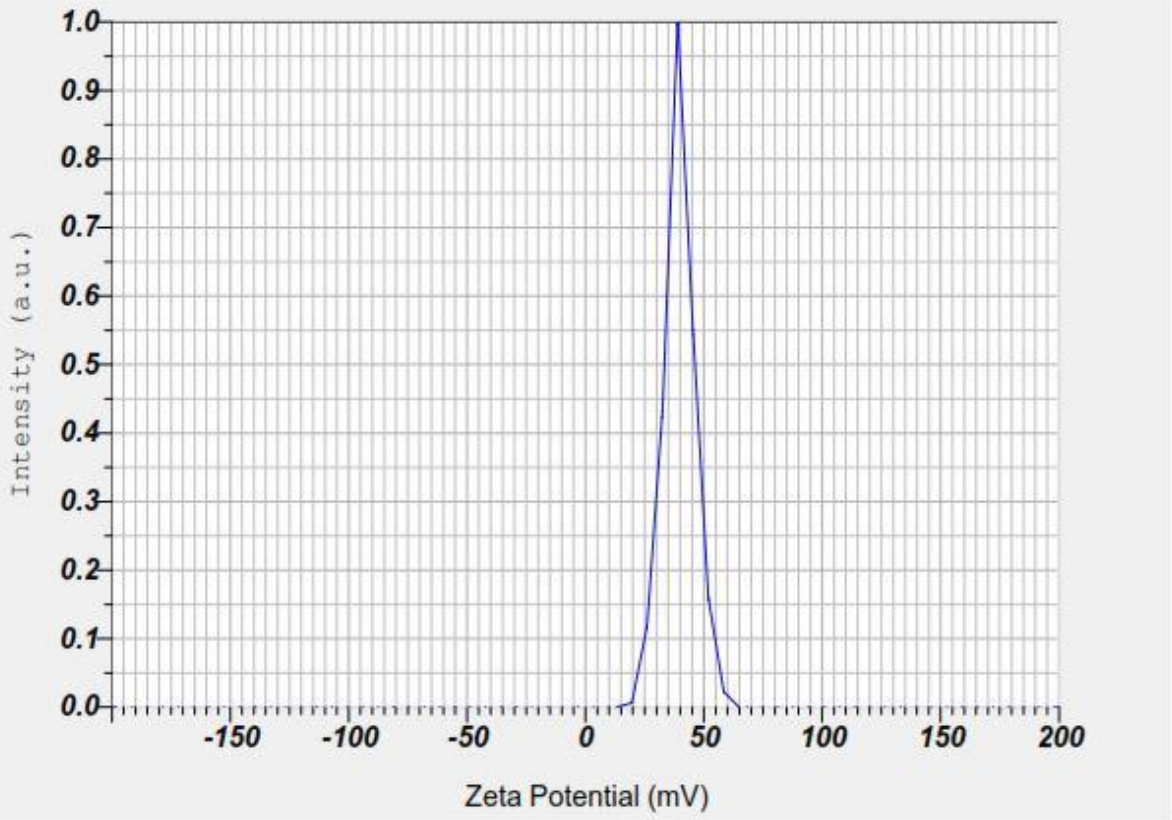

Fig. 9. Zeta potential distributions for FSC nanocomposite prepared on Fe_3O_4@SiO_2 (FS).

Where, ε_0 and εr are dielectric constants of vacuum and solvent respectively, η is viscosity and U is the mobility of the particles in suspended solution. In general, when an electric field is applied to the charged particles in a colloidal sample, particles move toward an electrode opposite to its surface charge. Because the velocity is proportional to the amount of charge of the particles, zeta potential can be therefore estimated by measuring the mobility of these particles. To determine the speed of the particles movement, the particles was normally irradiated with laser light, and the light emitted from the particles was detected from the shifted scattered frequency. Since shifted scattered light from incident light is proportional to the speed of the movement of the particles, the electrophoretic mobility of the particles can be thereby measured [34-37]. The most widely used theory for calculating zeta potential from experimental data was developed by Marian Smoluchowski in 1903 [37].

Experimental zeta potential value obtained in this work for FSC nanocomposite prepared on Fe_3O_4@SiO_2 (FS) is given in Fig. 9. This result reveals a bimodal zeta potential distribution may be due to the two different populations of particles within the prepared suspension sample. About 42% of the particles have a zeta potential of +50 mV, and 58% of the particles have a lower value of +40.94 mV. Considering that and a dividing line between stable and unstable aqueous dispersions reported at either +15 or +65mV, particles with zeta potentials more positive than +30mV have been considered stable, and particles with low absolute values of the zeta potential will agglomerate, and the dispersion becomes unstable [38-46], we can conclude that colloidal samples prepared in this work at the our experimental condition even after 4 hours ultrasonic treatment, were unstable because of FSC nanocomposite high tendency to aggregate.

Considering the important role of temperature on the drug loading and the body temperature, three different temperatures 35, 43, and 50 °C were investigated (Fig. 10). Results showed that by increasing temperature, the drug loading was increased, and the best loading was achieved at 50 °C.

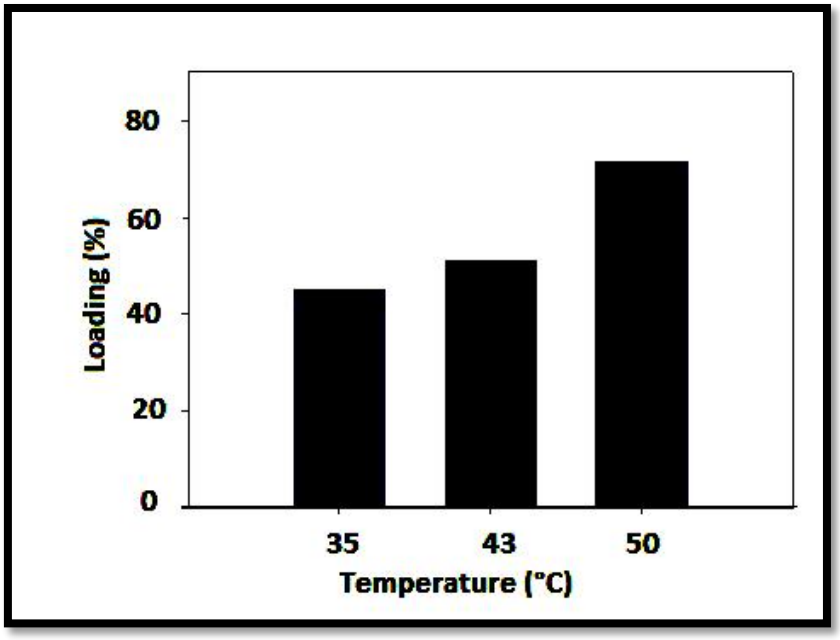

Fig. 10. Effect of temperature on loading of celecoxib onto FSC.

According to the diagram with equation Y=19.883X+0.0025, the correlation coefficient for equation 0.999 has been calculated, which is desirable (Table 2, Fig. 11). According to the results, the only mechanism of drug release from nanocomposite in solution was the Fickian model, and matrix degradation did not have the main role in the release of *Celecoxib*. The early high-level release is probably due to the release of *Celecoxib* on the surface of the nanocomposite that was matched with the Higuchi model (Table 3). Therefore, because of the heavy-metal degradation of the FSC, the release mechanism does not match with the Hixon-Crowell model. The greatest value of the correlation coefficient (r^2) was obtained from the Higuchi model. In addition, the correlation coefficient for the different release rates of the drug from FSC explains relative adaptation to the First-order model. This model is related to the delivery of poorly soluble drugs into the release medium. In addition to Fickian theory, four more models were used to analyze the drug-release profile further, including the first order, Higuchi, and Hixon–Crowell models. These model equations are listed as follows:

First order: $\ln Q_t = \ln Q_0 + K_1 t$ (3)

Hixson–Crowell: $Q_0^{1/3} - Q_t^{1/3} = K_s t$ (4)

Higuchi: $Q_t = K_H \sqrt{t}$ (5)

Q_t is the amount of drug dissolved in time t, Q_0 is the initial amount of drug in the solution (most of the time, $Q_0^{¼}$), K_1 is the first-order release constant, K_H is the Higuchi dissolution constant, and K_S is a constant incorporating the surface–volume relation [31-32].

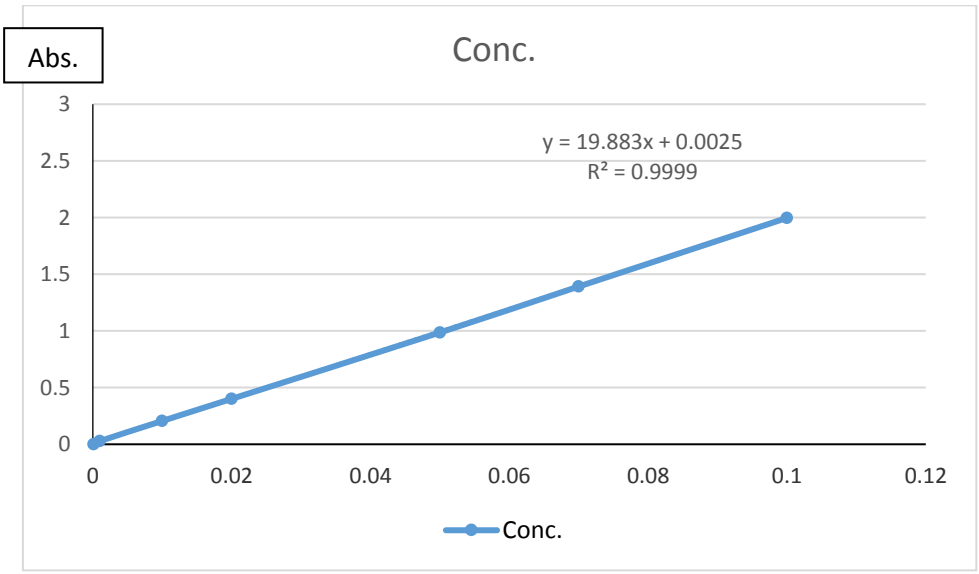

Fig. 11. Celecoxib calibration curve onto FSC.

Table 2. Results of celecoxib adsorption.

Conc. (mM)	Absorbsion
0.0001	0
0. 001	0.028
0.01	0.206
0.02	0.401
0.05	0.986
0.07	1.392
0.1	1.997

Table 3. Regression coefficients of mathematical models fitted to the release of *Celecoxib* from the FSC- *Celecoxib* nanocomposites mats.

samples	Zero order	First order	Hixson–Crowell	Higuchi
FSC- *Celecoxib*	0.37 ± 0.03	0.61 ± 0.06	0.4 ± 0.01	0.8 ± 0.09

Stability studies of Celecoxib/FSC were carried out by storing optimized formulation at 4 ± 1 °C and 30 ± 2 °C for 3 months. The samples were analyzed at 1-3 months for their drug content and drug release rate ($t_{50\%}$), as well as any changes in their physical appearance (Table 4). These results indicated that the developed Celecoxib/FSC nanoparticles retain their pharmaceutical properties at various environmental conditions over a period of 3 months and are physically/chemically stable.

Thermogravimetric analysis (TGA) traces of $Fe_3O_4@SiO_2@CeO_2$ magnetic nanoparticles are illustrated in Fig. 12. TGA of Fe_3O_4 exhibits 9% weight loss because of the removal of water molecules and surface hydroxyl groups (Fe−OH) [44], whereas that of $Fe_3O_4@SiO_2@CeO_2$ contains two weight losses in the range 180−210 and 500−680 °C. The first weight loss is attributed to the dehydration of CeO_2. Similar TGA behavior was observed by Yang and co-workers in nanoceria prepared by the solvothermal synthesis in ethylene glycol [48]. TGA analysis revealed that, apart from the solvent mass loss, all samples underwent large weight loss in the temperature range 205–395 °C (13–26%) accompanied by endothermic processes [46], probably due to oxalate decomposition and leaching of organic ligands [49], that formed an inorganic–organic composite with ceria.

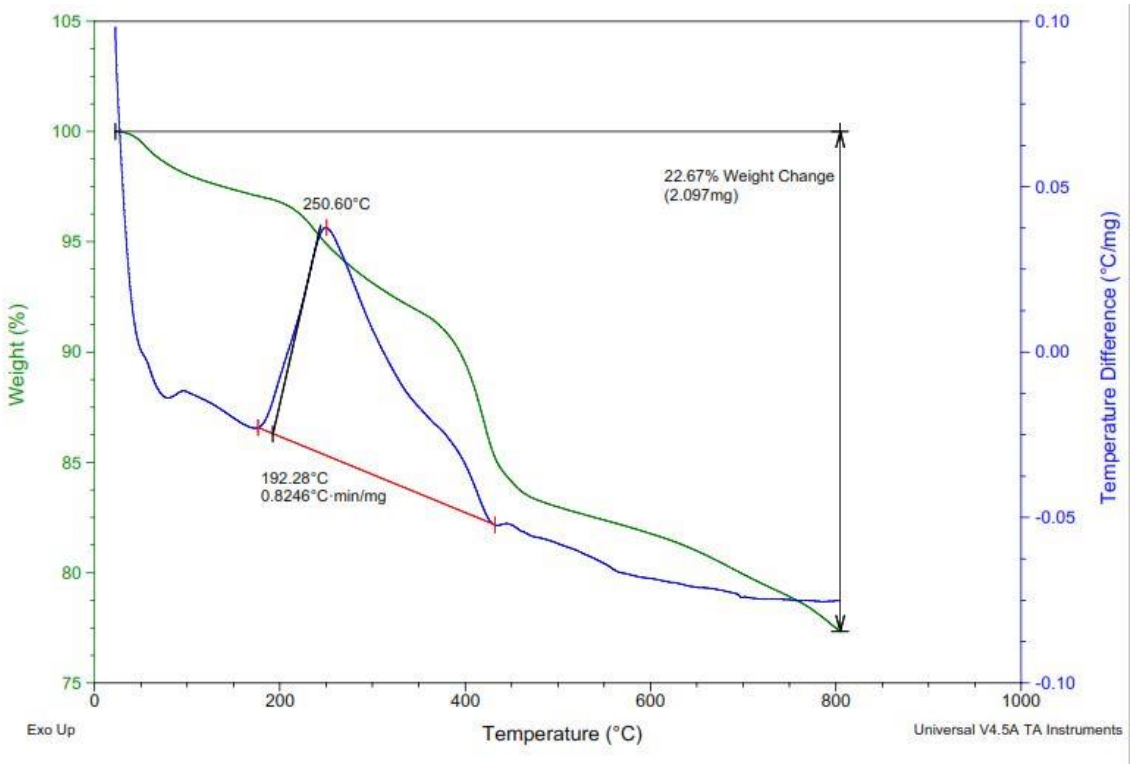

Fig. 12. TGA curves of $Fe_3O_4@SiO_2@CeO_2$ (FSC) in the range 0−1000°C.

Table 4. Regression coefficients of mathematical models fitted to the release of *Celecoxib* from the FSC- *Celecoxib* nanocomposites.

Temperature	Evaluation Parameters	Observation (Months)			
		0	1	2	3
40°C ± 2°C	Physical appearance	---	No change	No change	No change
	%Drug content	77.15	74.65	73.45	71.86
	$t_{50\%}$ (hrs)	13.85	13.18	12.90	12.75
8°C ±1°C	Physical appearance	---	No change	No change	No change
	%Drug content	77.15	75.67	74.91	72.88
	$t_{50\%}$ (hrs)	13.85	13.65	13.16	12.92

4. Conclusions

In this study, celecoxib/FSC nanoparticles were successfully prepared by the modified nanoprecipitation method. Magnetite Fe_3O_4@SiO_2 nanoparticles are synthesized by the sol-gel method. In summary, the uniform Fe_3O_4 nanoparticles were successfully synthesized, and then the prepared nanoparticles were enriched with silanol groups and were finally modified with TMPA to improve their efficiencies in the delivery of celecoxib. The introduced biocompatible delivery system showed a very good capacity for the storage of a large amount of celecoxib. The two important parameters of pH and amounts of the nanocomposite were investigated. In order to show the necessity of modification, the efficiency of the FSC nanomaterial was compared with FSC, and the results demonstrated that modification has been absolutely effective. With respect to particle size entrapment efficiency, it can be included that the formulation (m_{FSC}=5 mg, pH=3.3) was considered to be the best among various formulations. The pH and concentration of biomaterial used for formulating these batches of nanoparticles showed a significant effect on its efficiency to entrap the Celecoxib molecule. Dynamic light scattering (DLS) techniques used to measure particle size and zeta potential distribution revealed successful preparation of the FSC nanocomposite prepared on Fe_3O_4@SiO_2 (FS), with a hydrodynamic size distribution of 45 nm. Bimodal zeta potential distribution in divergence with the DLS average zeta size data reveals the instability of the FSC nanocomposite because of casein- calcium nanocomposite's high tendency to aggregation. Cerium oxide displaces electron transfer and absorption band due to the presence of f-orbital in the cerium network.

ETHICS APPROVAL AND CONSENT TO PARTICIPATE

Not applicable.

HUMAN AND ANIMAL RIGHTS

No animals/humans were used for the studies that are the basis of this research.

CONSENT FOR PUBLICATION

Not applicable.

AVAILABILITY OF DATA AND MATERIALS

Not applicable.

ACKNOWLEDGMENTS

The financial support and encouragement support was provided by the Research vice Presidency of North Tehran Branch, Islamic Azad University and Executive Director of Iran-Nanotechnology Organization (Govt. of Iran), and Executive Director of Iran-Nanotechnology Organization (Govt. of Iran).

References

[1] Van, R. S.; Habibovic, P. Enhancing regenerative approaches with nanoparticles. J. R. Soc. Interf. Vol. 14, No. 129, 2017, pp. 20170093.

[2] Conte, R.; Marturano, V.; Peluso, G. Recent advances in nanoparticle-mediated delivery of anti-inflammatory phytocompounds. Int. J. Mol. Sci. Vol. 18, No. 4, 2017, pp. 709-714.

[3] Arbos, P.; Campanero, M. A.; Arangoa, M. A.; Renedo, M. J.; Irache, J. M. Influence of the surface characteristics of PVM/ MA nanoparticles on their bioadhesive properties. J. Control. Release. Vol. 89, No. 1, 2003, pp. 19-30.

[4] Ginebra, M. P.; Traykova, T.; Planell, J. A. Calcium phosphate cements as bone drug delivery systems: A review. J. Control. Rel. Vol. 113, No. 2, 2006, pp. 102-107.

[5] Patri, A. K.; Majoros, L. J.; Baker, J. R. Dendritic polymer macromolecular carriers for drug delivery. Curr. Opin. Chem. Bio. Vol. 6, No. 4, 2002, pp. 466-471.

[6] Rezwan, K.; Chen, Q. Z.; Blaker, J. J.; Boccaccini, A. R. Biodegradable and bioactive porous polymer/inorganic composite scaffolds for bone tissue engineering. Biomater. Vol. 27, No. 18, 2006, pp. 3413-3431.
[7] Horcajada, P.; Chalati, T.; Serre, C.; Gillet, B.; Sebrie, C. Porous metal-organic-framework nanoscale carriers as a potential platform for drug delivery and imaging. Nat. Mater. Vol. 9, 2010, pp. 172-178.
[8] Zahir Abadi, I. J.; Sadeghi, O.; Lotfizadeh, H. R.; Tavassoli, N.; Amani, V.; Amini, M. M. Novel modified manoporous silica for oral drug delivery: Loading and release of clarithromycin. J. Sol Gel Sci. Technol. Vol. 61, No. 1, 2012, pp. 90-95.
[9] Tang, F.; Li, L.; Chen, D. Mesoporous silica nanoparticles: Synthesis, biocompatibility and drug delivery. Adv. Mater. Vol. 24, No. 12, 2012, pp. 1504-1534.
[10] Van, R. S.; Habibovic, P. Enhancing regenerative approaches with nanoparticlesJ. R. Soc. Interf. Vol. 14, No. 129, 2017, pp. 20170093.
[11] Tang, Q.; Xu, Y.; Wu, D.; Sun, Y.; Wang, J. Studies on a new carrier of trimethylsilyl-modified mesoporous material for controlled drug delivery. Control. Rel. Vol. 114, No. 1, 2006, pp. 41-46.
[12] Trewyn, B. G.; Giri, S.; Slowing, I. I.; Lin, V. S. Y. Mesoporous silica nanoparticle based controlled release, drug delivery and biosensor systems. Chem. Commun. Vol. 31, No. 3, 2007, pp. 3236-3241.
[13] Yang, Q.; Wang, S. H.; Fan, P.; Wang, L.; Di, Y.; Lin, K.; Xiao, F. S. pH-responsive carrier system based on carboxylic acid modified mesoporous silica and polyelectrolyte for drug delivery. Chem. Mater. Vol. 17, No. 1, 2005, pp. 59-68.
[14] Chomchoey, N.; Bhongsuwan, D.; Bhongsuwan, T. Magnetic properties of magnetite nanoparticles synthesized by oxidative alkaline hydrolysis of iron powder. J. Nat. Sci. Vol. 44, No. 12, 2010, pp. 963-971.
[15] Hoa, L. T. M.; Dung, T. T.; Danh, T. M.; Duc, N. H.; Chien, D. M. Preparation and characterization of magnetic nanoparticles coated with polyethylene glycol. J. Phys. Vol. 187, No. 1, 2009, pp. 12-18.
[16] Acar, H. Y. C.; Garaas, R. S.; Syud, F.; Bonitatebus, P.; Kulkarni, A. M. Superparamagnetic nanoparticles stabilized by polymerized PEGylated coatings. J. Magn. Magn. Mater. Vol. 293, No. 1, 2005, pp. 1-7.
[17] Mohammadyan, E.; Ghafuri, H.; Kakanejadifard, A.; Synthesis and characterization of a magnetic Fe_3O_4@CeO_2 nanocomposite decorated with Ag nanoparticle and investigation of synergistic effects of Ag on photocatalytic activity. Optik. Vol. 166, 2018, pp. 39-48.
[18] Moradi, B.; Nabiyouni, Gh. R,; Ghanbari, D.; Rapid photo-degradation of toxic dye pollutants: green synthesis of mono-disperse Fe_3O_4–CeO_2 nanocomposites in the presence of lemon extract. J. Mater. Sci: Mater. Elect. Vol. 29, No. 5-6, 2018, pp.11065-11080.
[19] Rizzuti, A.; Dipalo, C. M.; Allegereta, I.; Terzano, R.; Cioffi, N.; Microwave-assisted solvothermal synthesis of Fe_3O_4–CeO_2 nanocomposite and their catalytic activity in the imine formation from benzyl alcohol and aniline. Catalyst. Vol. 10, No. 1325, 2020, pp. 1-22.
[20] Channei, D.; Inceesungvorn, B.; Wetchakun, N.; Phanichphant, S. Synthesis of Fe_3O_4/SiO_2/CeO_2 core-shell magnetic and their application as photocatalyst. J. Nanosci. Nanotechnol. Vol. 14, No. 10, 2014, pp. 7756-7762.
[21] Huang, Y.; Zhang, L.; Huan, W.; Xiaojuan, L.; Yang, Y. A study on synthesis and properties of Fe_3O_4 nanoparticles by solvothermal method. Glass Phys. Chem. Vol. 36, No. 3, 2010, pp. 325-331.
[22] Saadatjooa, N.; Golshekana, M. Organic/inorganic MCM-41 magnetite nanocomposite as a solid acid catalyst for synthesis of benzo [α] xanthenone derivatives. J. Mol. Cat. A: Chem. Vol. 377, No. 5, 2013, pp. 173-179.
[23] Donga, Y.; Wai, K. N.; Shen, S.; Kim, S.; Tan, R. B. H. Preparation and characterization of spironolactone nanoparticles by antisolvent precipitation. Int. J. Pharm. Vol. 375, No. 1-2, 2009, pp. 84-88.
[24] Maniya, N. H.; Sanjaykumar, R. P.; Murthy, Z. V. P. Controlled delivery of celecoxib from porous silicon micro- and nanoparticles. Appl. Sur. Sci. Vol. 330, No. 8, 2015, pp. 358-363.
[25] Huang, S. T.; Du, Y. Z. Synthesis and anti-hepatitis B virus activity of celecoxib conjugated stearic acid-g-chitosan oligosaccharide micelle. Carbohydr. Polym. Vol. 83, No. 18, 2001, pp. 1715-1722.
[26] Dandagi, P.; Patel, P.; Mastiholimath, V.; Gadad, A. Development and characterization of a particulate drug delivery systemfor etoposide. Ind. J. Novel Drug Deliv. Vol. 3, No. 1, 2001, pp. 43-51.
[27] Liu, X.; Ma, Z.; Xing, J.; Liu, H. Preparation and characterization of amino–silane modified superparamagnetic silica nanospheres. J. Magn. Magn. Mater. Vol. 270, No. 1-2, 2004, pp. 1-6.
[28] Masteri-Farahani, M.; Tayyebi, N. A new magnetically recoverable nanocatalyst for epoxidation of olefins. J. Mol. Catal. A: Chem. Vol. 348, No. 1, 2011, pp. 83-88.
[29] Banerjee, S. S.; Chen, D. H. Magnetic nanoparticles grafted with cyclodextrin for hydrophobic drug delivery. Chem. Mater. Vol. 19, No. 25, 2007, pp. 6345-6349.

[30] Allemann, E.; Gurny, R.; Deolker, E. Drug loaded nanoparticles: preparation methods and drug targeting issues. Eur. J. Pharm. Biopharm. Vol. 39, No. 5, 1993, pp. 173-191.
[31] Banerjee, T.; Mitra, S.; Singh, A. K.; Sharma, R. K.; Maitra, A. Preparation and biodistribution of ultrafine chitosan nanoparticles. Int. J. Pharm. Vol. 243, No. 1-2, 2002, pp. 93-105.
[32] Moazzen, E.; Ebrahimzadeh, H.; Amini, M.; Sadeghi, O. J. A novel biocompatible drug carrier for oral delivery and controlled release of antibiotic drug: Loading and release of clarithromycin as an antibiotic drug model. Sol Gel Sci. Technol. Vol. 66, No. 5, 2013, pp. 345-352.
[33] Rodríguez-Lugo V., Salinas-Rodríguez E., Vázquez R. A., Alemán K., Rivera A. L., Hydroxyapatite synthesis from a starfish and β-tricalcium phosphate using a hydrothermal method. RSC Adv. Vol. 7, No. 13, 2017, pp. 7631-7639.
[34] Shahmohammadi M., Jahandideh R., Behnamghader A., Rangie M., Sol-gel synthesis of FHA/CDHA nanoparticles with a nonstochiometric ratio. Int. J. Nano Dimens. Vol. 1, No. 1, 2010, pp. 41-45.
[35] Wang J. P., Chen Y. Z., Yuan S. J., Sheng G. P., Yu H. Q., Synthesis and characterization of a novel cationic chitosan-based flocculant with a high water-solubility for pulp mill wastewater treatment. Vol. 43, No. 20, (2009), pp. 5267-5275.
[36] De Bruyn J. R., Goiko M., Mozaffari M., Bator D., Dauphinee R. L., Dynamic light scattering study of inhibition of nucleation and growth of hydroxyapitate crystals by osteopontin. Plus One. Vol. 8, No. 55, (2013), pp. 56764-56768.
[37] Lyklema J., Fundamentals of interface and colloid science. Vol. 2, (1995), pp. 3-208. ISBN 0-12-460529-X.
[38] Russel W. B., Saville D. A., Schowalter W. R., Colloidal dispersions, cambridge university press. (1992), ISBN 0-521-42600-6.
[39] Dukhin A. S., Goetz P. J., Ultrasound for characterizing colloids. Elsevier. (2002), ISBN 0-444-51164-4.
[40] Hunter R. J., Foundations of colloid science, Oxford University Press. (1989), ISBN 0-19-855189-4.
[41] Smoluchowski M., Contribution to the theory of electro-osmosis and related phenomena. Bull. Int. Acad. Sci. Cracovie. Vol. 3, No. 3, (1903), pp. 184-199.
[42] Morrison I. D., Ross S., Colloidal dispersions: Suspensions, emulsions, and Foams. (2002), ISBN 978-0-471-82848-8.
[43] Wang L., Li S., Phosphorylated osteopontin peptides inhibit crystallization by resisting the aggregation of calcium phosphate nanoparticles. Cryst. Eng. Comm. Vol. 14, No. 22, (2012), pp. 8037-8043.
[44] Sadjadi M. S., Meskinfam, M., Sadeghi B., Jazdarreh H., Zare K., In situ biomimetic synthesis, characterization and in vitro investigation of bone-like nanohydroxyapatite in starch matrix. Mat. Chem. Phys. Vol. 124, No. 1, (2010), pp. 217-222.
[45] Sadjadi M. S., Meskinfam, M., Sadeghi B., Jazdarreh H., Zare K., In situ biomimetic synthesis and characterization of nano hydroxyapatite in gelatin matrix. J. Biomedical Nanotech. Vol. 7, No. 3, (2011), pp. 450-454.
[46] Sadeghi B., Ghammamy Sh., Gholipour Z., Amini Nia A., Gold/hydroxypropyl cellulose hybrid nanocomposite constructed with more complete coverage of gold nano-shell. Mic. & Nano Lett. IET. Vol. 6, No. 4, (2011), pp. 209-213.
[47] Wu Y., Xing v, Zhou T., Zhao C., Examining the use of Fe_3O_4 nanoparticles to enhance the NH3 sensitivity of polypyrrole films. Poly. Bull. Vol. 59, No. 3, 2011, pp. 227-234.
[48] Zhang, J.; Yang, J.; Wang, J.; Ding, H.; Liu, Q.; Schubert, U.; Rui, Y.; Xu, J. Top of Form Bottom of Form Surface oxygen vacancies dominated CeO_2 as efficient catalyst for imine synthesis: Influences of different cerium precursors. J. Mol. Catal. Vol. 443, No. 2, 2017, pp. 131-138.
[49] De Almeida, L.; Grandjean, S.; Vigier, N.; Patisson, F. Insights into the thermal decomposition of Lanthanide(III) and Actinide(III) Oxalates – from neodymium and cerium to plutonium. Eur. J. Inorg. Chem. Vol. 31, No. 62, 2012, pp. 4986-4999.

JMATPRO	Journal of Advanced Materials and Processing 10 (1): 27-38, Winter 2022 http://jmatpro.iaun.iau.ir 20.1001.1.2322388.2022.10.1.3.6

Research Paper

Mechanical Alloying and Spark Plasma Sintering of Equiatomic AlCoCrFeMnNi High Entropy Alloy

Farhad Abdi [1], Hossein Aghajani[1, 2*], Shahin Khameneh Asl[1]

1. Department of Materials Engineering, University of Tabriz, Tabriz, Iran.

2- School of Metallurgy and Materials Engineering, Iran University of Science and Technology, Tehran, Iran.

ARTICLE INFO

Article history:

Received 11 September 2021
Accepted 22 December 2021
Available online 1 January 2022

Keywords:
AlCoCrFeNiMn high entropy alloy
Mechanical alloying
Spark plasma sintering

ABSTRACT

In this research, a high entropy alloy of AlCoCrFeNiMn is made through mechanical alloying and the spark plasma sintering processes. Ball milling was done at different times of 12 h, 36 h, and 48 h in a cup with a diameter of 20 cm. Ball to powder percent weight of 10:1 was selected. X-ray diffraction patterns indicate the formation of solid solution microstructure after 48 h. The crystal size decreases from 23 to 16 nm with increasing milling time. The lattice strain of the structure increments from 0.3 to 0.68% with increasing time up to 48 h. SEM images clearly show the phenomenon of powder agglomeration and the absence of intermetallic compounds or brittle, complex structures. It is observed that with increasing ball-milling time, homogenization of powders increases, and the body-centered cubic phase is formed in the structure. The mechanically alloyed powders were consolidated spark plasma sintered at 700, 900, and 1000 °C. 50 MPa pressure, argon gas as atmosphere, and ten minutes as sintering time were selected as the sintering process parameters. The X-ray diffraction pattern shows that the structure of consolidated high entropy alloy has face-centered cubic and body-centered cubic phases. After sintering by the spark plasma method, the density of powders was measured by Archimedes' rules, and the value was determined as 99% of theoretical density. The structure was without porosity. The hardness was measured using the microhardness Vickers test. Loading force was 50 g and loading time was seven seconds. The highest hardness was about 649 $HV_{0.05}$.

Citation: Abdi, F.; Aghajani, H; Khameneh Asl, Sh. (2022) Mechanical Alloying and Spark Plasma Sintering of Equiatomic AlCoCrFeMnNi High Entropy Alloy. Journal of Advanced Materials and Processing, 10 (1), 27-38. Dor: 20.1001.1.2322388.2022.10.1.3.6

* **Corresponding Author**
E-Mail Address: haghajani@iust.ac.ir

1. Introduction

To develop new materials for the aerospace, automotive, and rail industries, scientists are trying to find materials and alloys that have improved and desired properties. High Entropy Alloys (HEA) were first introduced as a new concept in the design and production of alloys [1-3]. High entropy alloys are a new level of metal alloys. Unlike conventional alloys that are consisted of one or two main metal elements, these alloys contain at least five or more metal elements in the range of 5-35 atomic percentages.

High entropy alloys are widely used in the transportation and energy industries due to their low density and high strength. High entropy alloys are an excellent alternative to titanium and steel alloys [4]. Among the remarkable properties of HEAs, low diffusion and strength stability have received much attention at high temperatures. In the form of a rod or powder, HEAs can be coated on the surfaces of tools and other components as surface hardening materials. The thermal spray or plasma arc process is used for surface hardening [4].

High entropy alloy possesses several properties, including high strength, thermal stability, wear resistance, and corrosion resistance. These alloys have the highest configurational entropy. This parameter plays a significant role in the organization of solid solutions. The formation of a solid solution depends on some parameters, such as the melting point, the synthesis temperature, and the interaction between the atoms. They are known as multipurpose element alloys (MPEAS), concentrated solid alloys (CSAs), and complex composite alloys (CCAs) [5, 6]. High entropy alloys (HEAs) are based on four inherent properties: First, the entropy effect, which reinstates the solid solution formation. Second is the effect of lattice distortion, which mainly affects the properties. Third, the impact of slow diffusion reduces the diffusion kinetics, and fourth, the effect of alloying elements, which have a combined impact on the final properties. The CoCrFeNiMn alloy is one of the first HEAs alloys extensively investigated because of its excellent physical properties, among cryogenic properties [7], thermodynamic stability [8], and other properties.

It has been reported that the CoCrFeNiMn alloy microstructure includes only BCC solid solution. Although CoCrFeNiMn alloy has excellent properties, it does not have high mechanical properties [9]. Aluminum may improve mechanical properties and result in a higher lattice distortion. He et al. [10] confirmed that increasing the amount of Al increases the yield strength and reduces the density. The strengthening mechanism is via establishing a BCC solid solution phase [11, 12]. Also, Hall-Petch effects and refined grains play an essential role in this mechanism [13].

The HEAs have excellent corrosion resistance. By controlling the synthesis process, FCC, BCC, or an amorphous phase can be achieved, which leads to excellent corrosion resistance. In particular, combining some elements, including Cr, Ni, Co, and Cu, can increase the corrosion resistance of these alloys [14]. HEAs are made by melt casting [14-19, 21], mechanical alloying, high-energy ball milling [20, 22], and sputtering or molecular beam epitaxy (MBE) [23].

Many studies have been conducted on these alloys' synthesis and composition after normal melting and solidification. These benefits include good density in the specimens, no gas vacancies, and the removal of harmful contaminants from other elements. However, melting creates coarse grains (≥4μm) with a heterogeneous structure during solidification [24]. The other method is powder metallurgy. A combination of mechanical alloying (MA) and sintering processes is prevalent in producing high entropy alloys. This method has a wide range of applications. In mechanical alloys (MA), solid solutions are formed at room temperature, and a homogeneous alloy is formed.

The mechanical alloying (MA) process presents many challenges in preparing HEA powders, including contamination during milling, oxidation, and a limited ability to shape [25]. The phase is observed to change with increasing rotation speed and the use of balls of different diameters. Phase transformation occurs when energy is transferred to the powders. High energy is very effective in achieving a Nano--crystalline structure in the powders [26]. The material of the milling cup also affects the type of phases. As an example, the CoCrFeNiMn alloy exhibits a single-phase FCC structure when synthesized using a WC cup and ball [27], while the BCC phase appears in the structure when synthesized using a stainless-steel cup and balls [28]. This may be due to the presence of chromium in the stainless steel. The FCC or BCC phase formation is related to reactive powders' processing condition and composition. He et al. [29] examined the impacts of Al addition on the microstructure and tensile strength of FeCoCrNiMn HEA. He et al. [29] reported that regarding the Al-containing HEA alloy, when the Al amount exceeded to 16%, the microstructure changed from the initial FCC to a single BCC structure. CoCrFeNiMnAl alloy made by mechanical alloying demonstrates FCC phase upon annealing at 500 °C. The FCC and BCC phases are created after Spark Plasma Sintering (SPS) process [30]. The powder metallurgy process makes it possible to achieve Nano-sized particles, which

improves the mechanical properties. A comparison of induction melting and powder metallurgy shows that powder metallurgy is an excellent and preferred process in producing HEAs. In powder metallurgy, grain refining occurs during mechanical alloying so that these particles are kept together during sintering. While in the melting and induction method, the grains are coarse and non-uniform. The milled alloys must be compacted to become a high-density structure with acceptable operational properties. Sintering is selected mainly to achieve a combination of density and crystalline structure. SPS is one of the most widely used techniques for sintering powders, despite some limitations such as C contamination and small sample sizes with most SPS units. Alloy powders are first pressurized and then heated to be condensed. Other methods such as hot vacuum pressing (HVPS) [31-35], Beam microwave sintering (BMS) [36], and hot isostatic pressing (HIP) [37] are also used for sintering [38, 39]. Some parameters, such as short process times, make the SPS method superior to the other methods mentioned. As a result, there is less time for grain growth, and the grains can be easily compacted to nano-crystalline size [40]. Studies have demonstrated that applying the maximum pressure at higher temperatures results in better adhesion and bonding of powder particles. This leads to achieving greater flexibility [40]. Comparing microwave sintering and SPS methods shows that the first method creates a large amount of porosity in AlCoCrFeNi high entropy alloy, which affects the mechanical properties [41]. So, it can be concluded that SPS is the preferred method for sintering HEA powder.

In this research, the mechanical alloying (MA) method was used to make an AlCoCrFeNiMn alloy powder. After that, spark plasma sintering (SPS) was applied to powders, and the structure and phases formed at different sintering temperatures were characterized.

2. Experimental procedure

The production of AlCoCrFeNiMn alloy involves a few steps. In the first step, 99% pure powders of Al, Co, Mn, Ni, and Fe were prepared (Table 1). After determining the ratios required to achieve an equiatomic ratio, the required values were weighed on a high precision scale (0.0001g). Powders were then fed into a ball milling chamber and milled at different speeds. A stainless-steel chamber with a diameter of 10 cm was used in the mill process. And the balls were made of stainless steel. The ball to the powder weight percent (BPR) was selected as 10: 1. The mill was set at a rotational speed of 120 rpm. In this process, ethanol and alcohol were used as a process control agent (PCA). The powder mixture was milled at different times of 12 h, 36 h, and 48 h for mechanical alloying.

Table 1. Amounts and specifications of powder elements used to make AlCoCrFeNiMn alloy.

No	Element	Purity (%)	Size (μm)	Wt.%	Made by
1	Al	≥ 99	20 ≥	8.77	Germany
2	Co	≥ 99	10 ≥	19.17	Germany
3	Cr	≥ 99	63 ≥	16.89	South Korea
4	Fe	≥ 99	45	18.19	Germany
5	Mn	≥ 99	63 ≥	18.19	South Korea
6	Ni	≥ 99	75	17.87	Russia

The plasma spark sintering process was used to consolidate powders which were prepared after 48 h of ball milling. The sintering temperatures were selected 700, 900, and 1000 ° C. Sintering was performed in a vacuum atmosphere with average pressure 1.5 Pa. The axial pressure was 50 MPa, and the temperature rate was 50 °C / minute. The sample was maintained for ten minutes and then cooled in an argon atmosphere to ambient temperature.

The crystal structure of milled powders and sintered alloys was investigated by Bruker AXS, Advance D8, and Cu Kα X-ray devices. The scanning 2θ range was from 20 to 100 degrees. The scanning speed was 0.1 degrees per second. After SPS, the resulting alloys were studied again by X-Ray diffraction. The microstructure of the sintered samples was studied with an optical microscope CARL-ZEISS-4996387, and images with a magnification of 100× were prepared.

The mechanically alloyed powders and SPS synthesized alloys were investigated by ROVENTEC Vega TESCAN MIRA3 scanning electron microscope. The density of sintered alloys at different temperatures was determined using

Archimedes' principles. The hardness of the sintered alloy specimens was measured by the hardness Vickers MX-96604-BUEHLER micro-hardness tester. Vickers micro-hardness tester (MHVN) was used with a force of 50 g and a loading time of 15 seconds.

3. Results and discussion

3.1. Mechanically alloyed powder

Figure 1 illustrates the XRD patterns of as-milled AlCoCrFeMnNi powders combined at different milling times. At the angles of 2θ=38° peak of Al, 2θ=43° peak of Mn, 2θ=45° peak of Co, Cr, Ni, Fe, and Al, 2θ=49° peak of Co and Mn, 2θ=53° peak of Co and Ni, 2θ=65°peak of Cr, Fe and Ni 2θ=76° peak of Co and Ni, 2θ=78° peak of Al and 2θ=84° peak of Fe and Cr elements are present. These peaks' intensities are less than the intensity of the elemental peaks in the XRD test taken from the powder of these elements [25].

After 12 h of milling, peaks of alloying elements are observed with a noticeable decrease in intensity. With the increase of milling time, peaks broadening is apparent, and some peaks become invisible after 48 h. By increasing the mixing time to 36 h, the peaks are flattened. The vanishing of the peaks can indicate the formation of a solid solution phase. Although the elements' peaks are seen at first, with the increasing milling time, the peak intensity of the elements decreases. As a result, milling becomes effective. 36-hour milling produces only BCC peaks with peaks of some elements, such as Al and Ni. As the milling time increases to 48 h, only one peak is visible, confirming the formation of a complete solid solution phase. After milling for 48 h, the elemental peaks have vanished. An accumulated peak at 2q = 44-45° indicates the formation of a solid solution structure of BCC. The formation of BCC phases in the alloy is due to powerful BCC forming elements such as Cr, Fe, Mn, and Al [42].

Three parameters use to evaluate the collective behavior of elements in a multi-component alloy system: the entropy of mixing (ΔSmix), the enthalpy of mixing (ΔHmix), and the atomic size difference parameter (δ). The values of ΔSmix and ΔHmix could be figured out based on the Boltzmann hypothesis and the Miedema model, respectively. Using these three parameters, the formation criteria for equiatomic high entropy solid solution can be summarized as the following:

(1) $\Delta Smix \geq 1.61R$

(2) $\delta \leq 6.45$:

(3) $-2.685\ \delta - 2.54 \leq \Delta Hmix \leq -1.28\ \delta + 5.44$ kJ/mol.

Adopted the three parameters and took another two into account: the electronegativity (Δχ) and the valance electron concentration (VEC), which were considered from the Hume-Rothery rules [18, 19]. Both Δχ and VEC have weak effects on enhancing the formation of solid solution or amorphous phase. However, VEC plays a significant role in forming the FCC or BCC solid solution in high-entropy alloys, a large value of VEC (≥8) promotes the formation of the FCC phase, while a smaller value leads to the BCC phase. The as-calculated values of ΔSmix ($JK^{-1}mol^{-1}$), ΔHmix ($KJmol^{-1}$), and δ for AlCoCrFeMnNi high-entropy alloy are 1.61R, -11.89, and 5.56 respectively, which are highly consistent with the formation criteria.

Moreover, the extension of solid solubility is the main advantage of MA. Therefore, it is reasonable to infer that forming a simple solid solution for the MA-ed HEA is easier. According to the value of valence electron concentration, the solid solution type of AlCoCrFeMnNi high-entropy alloys is BCC, which has been confirmed by XRD analysis [42].

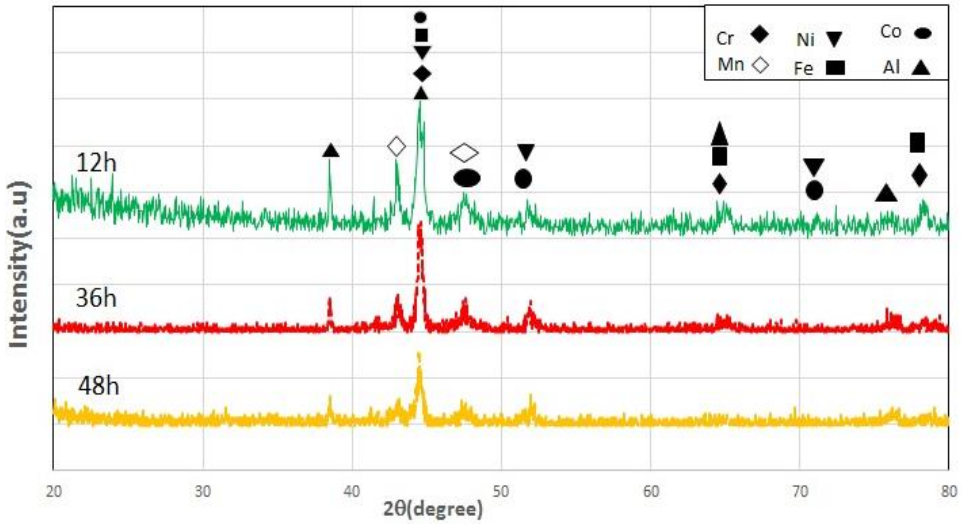

Fig. 1. XRD diagram of high entropy AlCoCrFeMnNi alloy powder with various milling times of 12 h, 36 h, and 48 h.

Along with the milling method, the decrement in intensity and the broadening of the peak may result from the three parameters: refined crystal size, high lattice strain, and decreased crystallinity. As a result of the mechanical alloying process, the diffraction peak vanishes due to 1) crystal refinement, 2) high lattice distortion, and 3) solid solution. The Scherer formula measures the size of the crystals (CS) after different milling periods. Also, lattice strain (LS) was measured with the help of Expert High Score software. According to the Table 2, the size of the crystals and the strain of the lattice change with milling time.

Table 2. The crystal size (CS) and lattice strain (% LS) at different milling time.

Milling time (h)	CS (nm)	LS %
0	-	-
12	20	0.35
36	17	0.6
48	15	0.66

Table 2 illustrates the impression of milling time on the crystallinity of AlCoCrFeNiMn powders. Increasing the milling time resulted in a decrease in the crystal size. As the milling time increases, more particles will collide with each other and with steel balls. The rotation of the chamber at a speed of 120 RPM also causes an exponential increase in these collisions. 20 nanometers for 12 h of milling reaches 15 nm for 48 h of milling, which shows this decreasing trend. When collisions increase, energy is transferred to the atoms, which causes the placement of elements with different atomic radii in the crystal structure. So, the crystal stress and lattice strain increase.

The crystal strain increases from 0.35% in 12 h to 0.66% in 48 h of milling. It is actually due to the repeated collisions of the powder particles and balls. On the other hand, the network distortion increases to 0.66%. In the research of Ju et al. [42], the same results about lattice distortion have been reported. According to the Scherer formula, BCC peaks are low in intensity and the corresponding peaks widths′ show a decrease in crystal size. It shows the alloying process is being completed after 48 h of milling. The nanoscale of crystallite size indicates that the micrometer-scale alloy particles have reached nanoscale-sized grains.

Figure 2 shows SEM images of powders. It can be seen the conversion in size, morphology, and agglomeration is a subordinate of milling time duration mechanical alloying. Al, Co, Cr, Fe, Ni, Mn element powders adhere to each other through cold welding by repeated collisions of steel balls. On average, the size of agglomerated powders increased after 12 h of milling. After 48 h, the particle size does not grow because of a balance between the cold welding and breaking of the welded powders. As shown in Figure 2 (a), micrometer-sized particles gradually adhere to each other through cold welding. As the milling time increases, more particles are welded to each other. This trend can be observed in Figure 2 (b,c). Figure (d,e) show the morphology of the particles after 48 h of milling, which is the final stage of mechanical alloying. It is shown that particles are fractured and have nanometer-scale sizes. This issue has also been obtained in the research of Wang et al. [42]. The size of the crystals and the strain of the lattice are measured after different milling times by the Scherer formula. They showed that after 30 h of mechanical alloying, the crystal size reaches 15 nm. Further increase in milling time has little effect on the crystal size, which indicates that equilibrium is achieved in mechanical alloying [42].

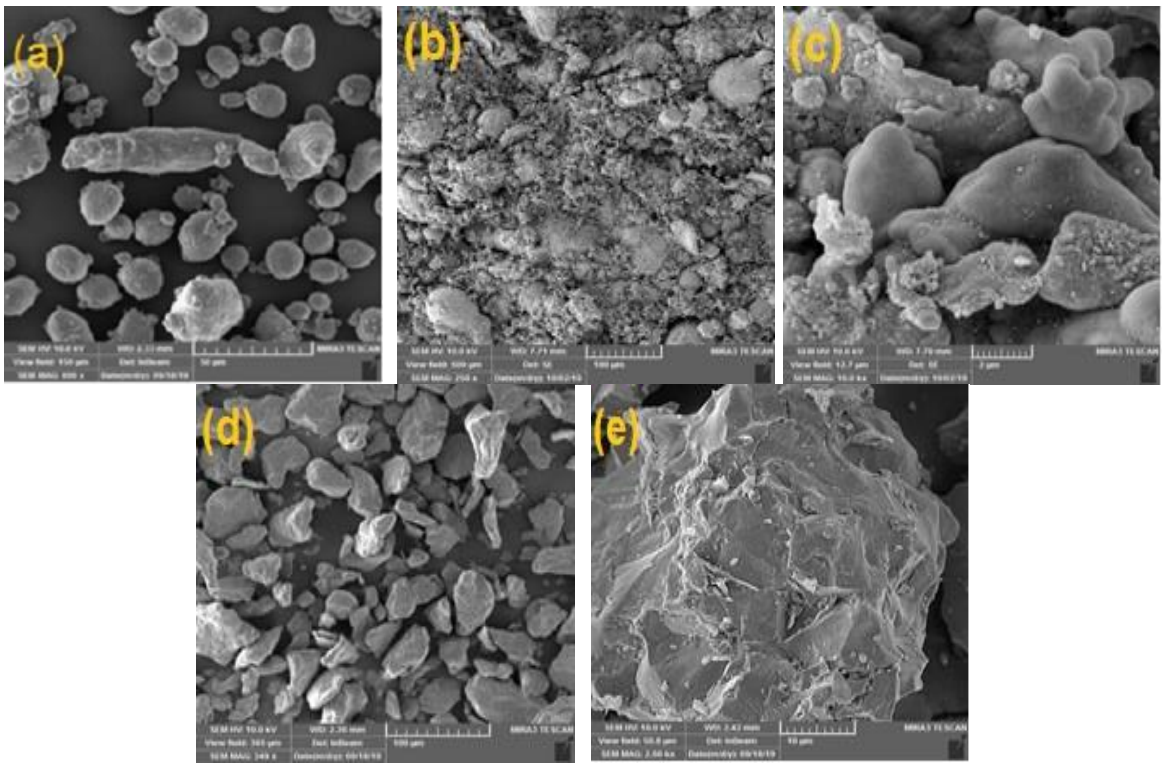

Fig. 2. SEM images of milled powders at different milling times (a) 12 h, (b,c) 36 h, and (d,e) 48 h.

3.2. Spark Plasma Sintered Specimens

To optimize the sintering temperature, experiments were done at 700, 900, and 1000 °C. Figure 3 shows the XRD pattern for spark plasma sintered specimens. In sintered sample at 700 °C, both BCC and FCC phases are detected. It is exciting that no intermetallic compounds were found in sintered high entropy alloy, which is desirable for mechanical properties in ambient temperature applications. The solid solution structure is composed of a structure consisting of BCC and FCC phases. The peak at 2θ=28° is related to the element carbon, which results from the graphite used in the spark plasma sintering process.

The creation of a solid solution in a high entropy alloy relates to the entropy of mixing (ΔSmix), enthalpy of mixing (ΔHmix), atomic size difference parameter (δ), electronegativity (Δχ) and electronic valance configuration (VEC). The theoretical calculation of these parameters was made on AlCoCrFeNiMn high entropy alloy. The value of ΔSmix, ΔHmix, δ, Δ χ, and VEC was apperceived to be 1.79R JK^{-1} mol^{-1}, -11.67 KJ mol^{-1}, 5.56, 1.2843, 7.1638, respectively. According to the listed parameters, the phase formation of AlCoCrFeNiMn high entropy alloy could be a mixture of both FCC and BCC solid solution, which complies with the XRD pattern outcome after sintering (Figure 3) [43].

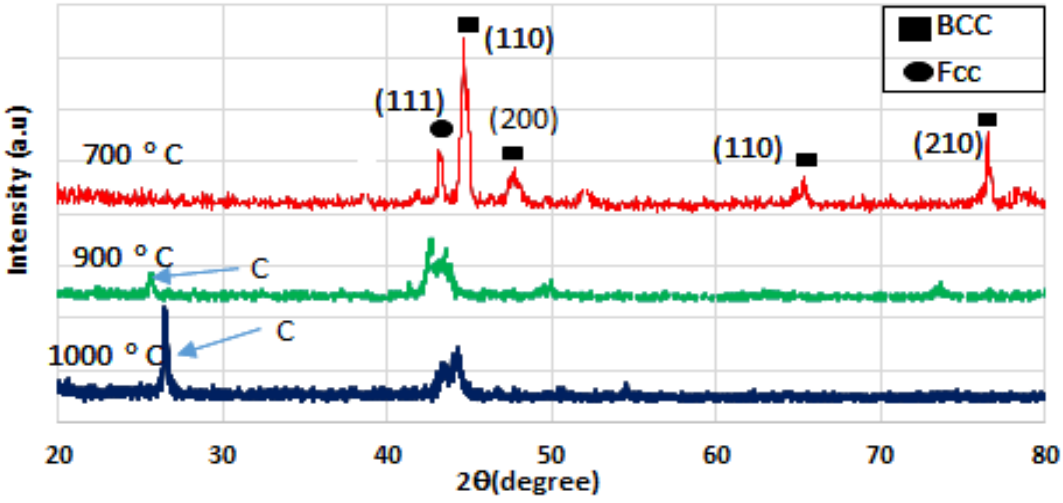

Fig. 3. XRD pattern of high entropy AlCoCrFeMnNi alloy powder at different sintering temperatures of 700, 900, and 1000 °C.

Figure 4 shows the microstructure of AlCoCrFeNiMn alloy sintered via the SPS process. These images show the metallographic images of spark plasma sintered alloy after it had been ball milled for 48 h. The formation of two phases with white and gray colors is clearly seen. Also, it is obviously seen very fine; dark color particles are dispersed in between dendrite. It seems that the structure in Figure 4 (c) is larger compared to Figure 4 (a,b). The reason is the occurrence of secondary grain growth at 1000 °C. The dark dispersed particles are graphite particles that are introduced during the SPS process and form some compounds with chromium. This is a chromium carbide compound that the graphite used in the sintering process penetrates due to the high penetration speed and combines with the chromium alloy element.

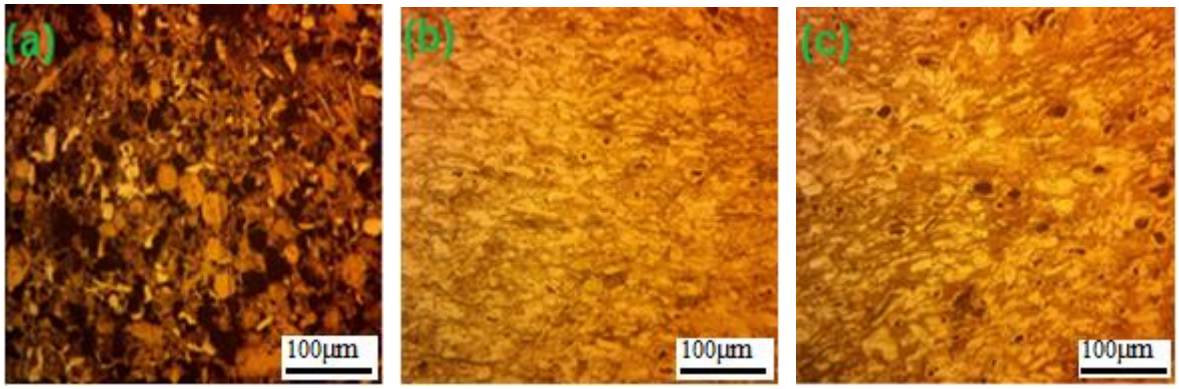

Fig. 4. Metallographic of AlCoCrFeMnNi alloy after sintering at different temperatures of (a) 700, (b) 900 and (c) 1000 °C.

Figure 5 shows the secondary electron image (SE), EDS, and map analysis of powders milled for 48 h and sintered by SPS. The images show that there are three areas with light and dark gray and black colors. Based on the EDS analysis of dark gray areas, the intensity of aluminum is higher there. The distribution of elements can be seen in the map analysis. It shows that these areas have more aluminum. The weight percentage of aluminum is 20.53 percent in this area. The region with 7.7wt % Cr is actually the BCC phase, which has the element of aluminum as the main phase. Aluminum's large atomic size prevents it from fitting into the structure of the FCC, which causes the formation of the BCC phase. The grain size is calculated at different sintering temperatures. At a sintering temperature of 700 °C, the grain size of the white phase is 30.7 µm and the grain size of the gray phase is 28.8 µm. At 900 °C, the grain sizes become 19.2 µm and 18.8 µm, respectively. At 1000 °C sintering temperature, the white phase grain size is 23 micrometers and the gray phase grain size is 21.3 micrometers. It is observed that with increasing the temperature, at first, a decrease in grain size is observed, and then at 1000 °C, a little increase in grain size could be seen. This decrease could be due to the bonding of different particles in the sintering process and the formation of new grain boundaries. The subsequent increase in grain size can be due to the increase in temperature and grain growth.

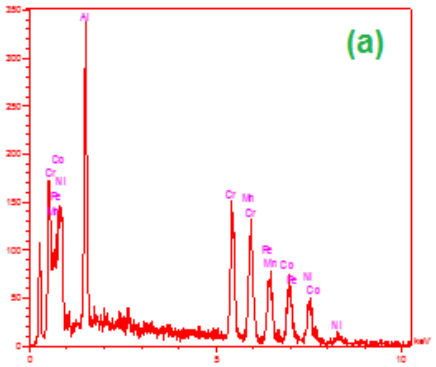

Elt	Line	Int	Error	K	Kr	W%	A%
Al	Ka	625.10	0.82	0.13	0.12	20.53	35.25
Cr	Ka	117.60	0.71	0.09	0.08	7.70	6.87
Mn	Ka	241.90	0.71	0.22	0.20	19.08	16. 09
Fe	Ka	72.20	0.71	0.08	0.07	6.98	5.79
Co	Ka	168.40	0.71	0.23	0.20	21.79	17.13
Ni	Ka	150.60	0.71	0.26	0.23	23.93	18.88
				1.00	0.90	100.00	100.00

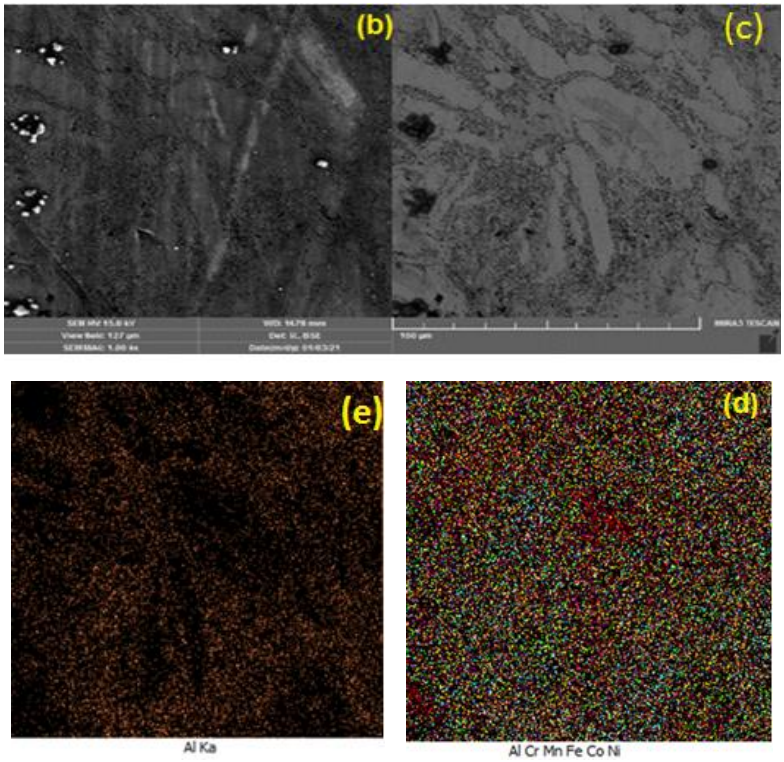

Fig. 5. (a) EDS of the dark gray zone at AlCoCrFeMnNi alloy powder sintered at 900°C. (b) and (c) Microstructure secondary image (SE) and, (e)-(d) map image of the dark gray zone at AlCoCrFeMnNi alloy powder sintered at 900°C.

Figure 6 shows the secondary electron image (SE), EDS, and map analysis of powders milled in 48 h and sintered by SPS. The images show that there are some areas with a light gray zone. According to the EDS analysis performed on light gray areas, the intensity of Cr is higher in this area. From the map analysis, the distribution of elements can be seen very easily. It illustrated that these areas have more Cr. The weight percentage of Cr is 19.29%. The region with 9.02 wt.% Al is actually the FCC phase, which has the element of Cr as the main phase. According to XRD patterns, AlCoCrFeNiMn alloy contains FCC and BCC phases. Some areas of microstructure have a dark area due to the fine size and the existence of the third carbide phase. The white phase is the exactly rich zone from Cr and has the HEA alloy composition. The dark gray phase has an Al and Ni-rich concentration which can be identified as the B2 phase, and the dark spots are the areas rich in Cr, which can be chromium carbide (Cr_3C_{27}). The carbon introduction occurs from the graphite crucible used in the sintering process. Carbon diffusion usually occurs rapidly. Carbide phases are often found in alloys obtained from the SPS process.

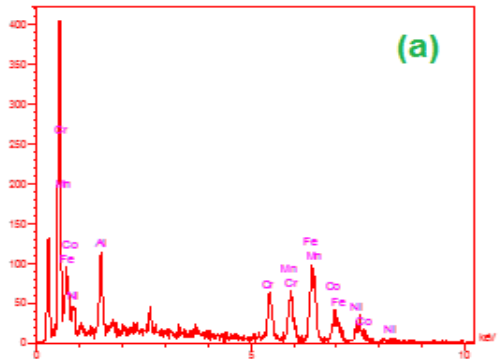

Elt	Line	Int	Error	K	Kr	W%	A%
Al	K a	276.00	0.99	0.05	0.05	9.02	17.03
Cr	K a	311.10	1.03	0.21	0.20	19.29	18.91
Mn	K a	229.90	1.03	0.19	0.18	17.60	16.32
Fe	K a	201.20	1.03	0.20	0.19	19.11	17.44
Co	K a	142.40	1.03	0.17	0.17	17.70	15.30
Ni	K a	112.60	1.03	0.17	0.17	17.28	15.00
				1.00	0.96	100.00	100.00

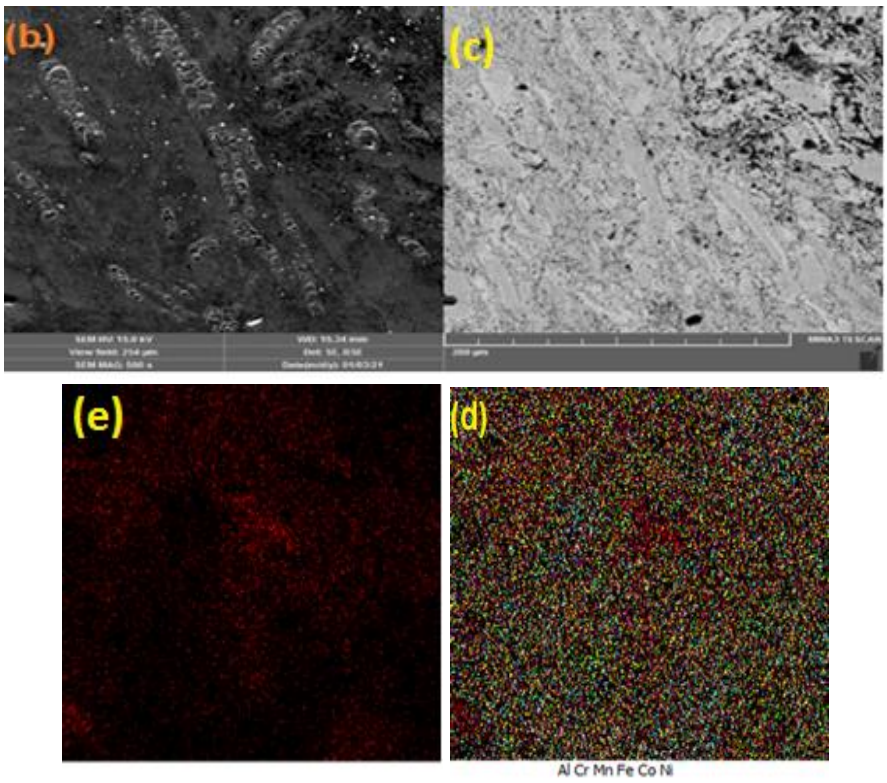

Fig. 6. (a) EDS, (b), (c) Microstructure secondary image (SE) and, (e) and (d) map image of the light gray zone at AlCoCrFeMnNi alloy powder sintered at 900°C.

The relative density and hardness of the alloy were measured after sintering at these temperatures. Figure 7 shows the relative density of spark plasma sintered specimens. The measured relative densities of all samples are larger than 99%, indicating they have reached near theoretical density. It is seen that the relative density enhances significantly from 700 to 900 °C. But a slight increase is seen from 900 to 1000 °C. At 1000°C, rapid grain growth stops, leading to a low increase in density. The increase in temperature caused by grain growth, elimination of grain boundaries, and loss of space between boundaries results in decreased porosity between grains and increased density. Although the highest density is attained at 1000 °C, the slope of density is decreased.

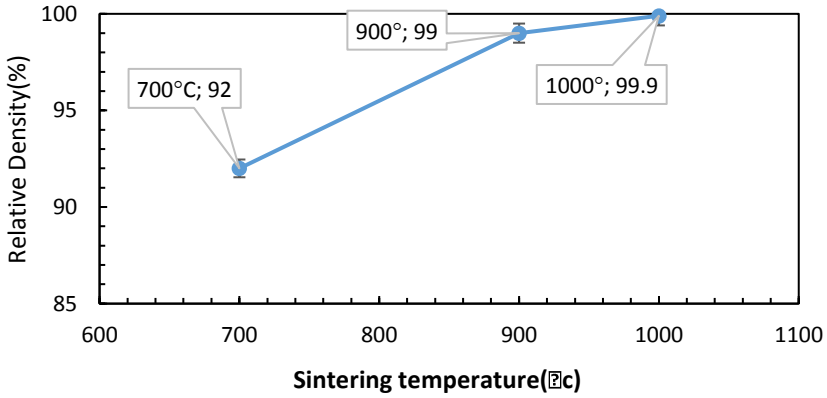

Fig. 7. Relative density of AlCoCrFeNiMn alloy at different sintering temperatures.

Figure 8 shows the hardness of sintered specimens. The hardness increased from 700 to 900 °C and then gradually decreased from 900 to 1000 °C due to the phenomenon of grain growthwhen HEAs are produced by powder metallurgy, grain refinement is accomplished during the mechanical alloying process. In the sintering step, these particles are kept smaller. Increasing the lattice distortion in mechanical alloying increases mechanical properties. Solid solution and the emergence of a BCC solid-phase increase the hardness to 649 Vickers. The hardness of 527 Vickers is achieved at 1000 °C due to slight grain growth with a slight decrease in hardness.

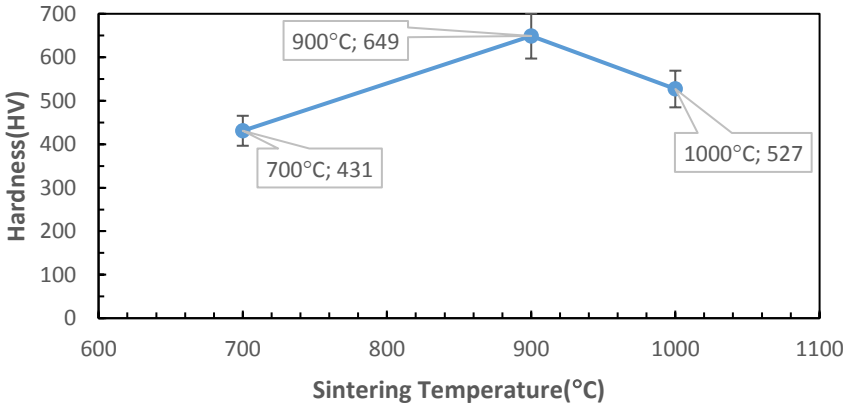

Fig. 8. Hardness of AlCoCrFeNiMn sintered alloy at different sintering temperatures.

It can be stated that the high entropy alloy of AlCrCoFeMnNi, which has a hardness of about 650 HV, will have good abrasion resistance. According to the Archard equation, the wear rate value is inversely related to the amount of hardness. The expectation is that alloys with higher hardness will have lower wear rates [44].

Cr is an important compound in HEA alloys and in the case of alloys with the equiatomic elements, Cr stabilizes the BCC structure and plays an important role in the mechanical properties of the alloy. The presence of Cr, Fe, Co elements that have the BCC structure at room temperature usually promotes the formation of the BCC phase. With the formation of the BCC phase, it is often seen an improvement in mechanical properties. The hardness of AlCoCrFeMnNi high entropy alloy also depends on the microstructure of the alloy. When the structure changes from a two-phase to a one-phase solid solution structure, the hardness increases, and this change improves the wear resistance [45].

4. Conclusions

In this study, AlCoCrFeNiMn alloy was prepared by milling and then SPS sintering process. Process parameters such as milling time and sintering temperature were optimized to get good results in an alloy with a high entropy single phase. 1) Milling times were selected as 12 h, 36 h, and 48 h, respectively. Based on the results, after 48 h of milling a high entropy alloy with a single solid solution structure was produced by mechanical alloying. The same phase is achieved in 48 h of milling. The optimum time to reach the alloy with the desired structure and properties was determined as 48 h. Also, the sintering operation was performed by spark plasma sintering at temperatures of 700, 900, and 1000 °C. 2) According to the XRD patterns and SEM images of the obtained structure, it consists of two-phase, chromium-rich FCC, and aluminum-rich BCC phase. Also, black carbide compounds are formed due to the introduction of graphite used in the SPS process and its combination with carbide-forming elements such as chromium. 3) If the density is a factor, then 1000 °C is the optimum sintering temperature since the density is 99.9% of the theoretical density. 4) The highest hardness is achieved at 900 °C sintering and is equal to 649 $HV_{0.05}$.

Declarations

There's no financial/personal interest or belief that could affect the objectivity, data, and nature of the manuscript. Also, this manuscript has no associated data. All data are given in the text.

Reference

[1] S. K. Tang, The Process Fundamentals and Parameters of Electro-Spark Deposition, Waterloo, Ontario, Canada, 2009.

[2] Environmental Security Technology Certification Program (ESTCP), Electrospark Deposition for Depot- and Field-Level Component Repair and Replacement of Hard Chromium Plating, U.S. Department of defense, Project WP-0202, 2006.

[3] E. sharghivand. H. Aghajani, M. Roostaei: FeNiCrAlCoMn High Entropy Alloy Coating Prepared on Ti6Al4V by ESD, Imat 2018, Tehran, Iran, 2018.

[4] D. Liu, W. Gao, Z. Li, H. Zhang and Z. Hu, Electro-spark deposition of Fe-based amorphous alloy coatings, Materials Letters 61 (2007) 165–167.

[5] S. Praveen, H.S. Kim, High- Entropy Alloys: Potential candidates for High-Temperature Applications-An Overview, Adv. Eng.Mater. 20 (2018) 1700645.

[6] W. Li, P. L., Peter K. Liaw, Microstructure and properties of high-entropy alloy films and coatings: a review, Mater. Res. Lett, 6 (2018) 199-229.

[7] N. Stepanoy, M. Tikhonovsky, N. Yurchenko, D. Zyubkin, M. Klimova, S. Zherebstove, A. Efenov, G. Salishchev, "Effect of cryo-deformation on structure and properties of CoCrFeMnNi high-entropy alloy, Intermetallics, 2015, 59, 8-17.

[8] B. Sckuh, F. Mendez-Martin, B. Volker, E.P. George, H. Clements, R. Pipan, A. Hohenwarter, Mechanical properties, microstructure and thermal stability of a nanocrystalline CoCrFeMnNi high-entropy alloy after sever plastic deformation, Acta Mater. 96 (2015) 258-268.

[9] M-R. Chen, S-J. Lin, J-W. Yeh, M-H. Chung, S-K. Chen, Y-S. Huang, Effect of vanadium addition on the microstructure, hardness, and wear resistance of Al0.5CoCrFeMnNi high-entropy alloy, Metal. Mater. Trans. A 37 (5) (2006), 1363-1369.

[10] J. Y. He. W. H. Liu, H. Wang, Y. Wu. X.J. Liu, T. G. Nieh, Z.P. Lu, Effects of Al addition on structural evolution and tensile properties of the CoCrFeMnNi high-entropy alloy system,Acta Mater. 62 (2014) 105-113.

[11] T. Borkar. B. Gwalani, D. Chudhuri, C. V. Mikler, C.J. Yannerta, Xianodong Chen, ghavan Ramanujan, M. J. Styles, M. A. Gibson, R. Banerjee, A combinatorial assessment of AlXCrCuFeNi2 (0< X < 1.5) complex concentrated alloys: microstructure, microhardness, and magnetic properties, Acta Mater. 116 (2016) 63-76.

[12] B. Gwalani, V. Soni, D. Choudhuri, M. Lee, J. Y. Hwang, S. J. Nam, H. Ryu, S. H. Hong, R. Banerjee, Stability of ordered L12 and B2 precipitates in face centered cubic based hugh entropy alloys-Al0.3CoFeCrNi and Al0.3CuFeCrNi2.5Cr. Mater. 123 (2016) 130-134.

[13] W. H. Liu, Y. Wu. J. Y. He, T. G. Nieh, Z. P Lu, Grain growth and Hall-Petch relationship in a high-entropy FeCrMnNiCoMn alloy, Scr. Mater. 68 (7) (2013) 526-529.

[14] J. W. Yeh, S. K. Chen, S. J. Lin, J. Y. Gan, T. S. Chin, T. T. Shun, C. H. Tsau, S. Y. Chang, Nanostructured high-entropy alloys with multiple principal elements: Novel alloy design concepts and outcome, Adv. Eng. Mater. 6 (2004) 299-303.

[15] B. Cantor, I.T.H. Chang, P. Knight, A. J. B. Vincent, Microstructural development in equiatomic multicomponent alloys, Mater . Sci. Eng. A. 375-377 (2004) 213-218.

[16] C. J. Tong, M. R. Chen, S. K. Chen, J. W. Yeh, T. T. Shun, S.J. Lin, S. Y. Chang, Mechanical perform of The AlXCrCoCuFeNi High- Entropy Alloy System with Multiprincipal Elements, Metall. Mater. Tran. A. 36 (2005) 1263-1271.

[17] P. K. Huang, J. W. Yeh, T. T. Shun, S. K. Chen, Multi-Principal Element Alloy

[18] With Improved Oxidation and Wear resistance for thermal Spray Coating, Adv. Eng. Mater. 6 (2004) 74-78.

[19] C. Y. Hsu, J. W. Yeh, S. K. Chen,T.T. Shun, Wear resistance and high-temperature compression strength of FCC CuCoNiCrAl0.5 alloy with boron addition, Metal, Mater. Trans. A. 35 (2004) 1465-1469.

[20] K. B. Zhang, Z. Y. Fu, J. Y. Zhang, W. M. Wang, S. W. Lee, K. Niihara, Characterization of nanocrystalline CoCrFeNiTiAl high-entropy solid solution processed by mechanical alloying, J. Alloys Compond. 495(2010) 33-38.

[21] S. Singh,N. Wanderka, B. S. Murty, U.Glatzel, J. Banhart, Decomposition in multi-component AlCoCrCuFeNi high-entropy alloy, Acta Mater. 59 (2011) 182-190.

[22] S. Praveen, A. Anupam, T. Sirasani, B. S. Murty, R. S. Kottada, Characterization of oxide dispersed AlCoCrFe high entropy alloy synthesized by mechanical alloying spark plasma sintering, Trans. Indian Inst. Met. 66 (2013) 369-373.

[23] Y. Zhang, T. T. Zuo, Z. Tange, M. C. Gao, K. A. Dahmen, P. K. Liaw, Z. P. Lu, Microstructure and properties of high-entropy alloys, Prog. Mater. Sci. 61 (2014) 1-93.

[24] F. Otto, A. Dlouhy, C. Somsen, H. Bei, G. Eggeler, E. P. George, The influences of temperature and microstructure, on the tensile properties CoCrFeMnNi high-entropy alloy, Acta Mater. 61(15) (2013) 5743-5755.

[25] M. Roostaei, H. Aghajani, M. Abbasi and B. Abasht, Formation of Al2O3/MoS2 nanocomposite coatings by the use of electro spark deposition and oxidation, Ceramics International, 47 (2021) 11644-53.

[26] X. R. Tan, G. P. Zhang, Q. Zhi, and Z.X. Liu, Effects of milling on the microstructure and hardness of Al2NbTi3Zr high-entropy alloy. Mater. Des. 109 (2016) 27-36.

[27] M. Vaidya, A. Marshal, K. G. Ppradeep, and B. S. Murty: Phase evolution and stability of nanocrystalline CoCrFeNi and CoCrFeMnNi high entropy alloys. J. Alloys Compd. 770, (2019) 1004-15.

[28] W. Ji, W. Wang, H. Wang, J. Zhang, Y.Wang, F. Zhang, and Z. Fu, Alloying behavior and novel properties of CoCrFeMnNi high-entropy alloy fabricated by mechanical alloying and spark plasma sintering. Intermetallics 56 (2014) 24-7.

[29] J. Y. He,W. H. Liu, H. Wang, Y. Wu, X. J. Lui,T. G.Nieh, Z. P. Lu, Effects of Al addition on structural evolution and tensile properties of the FeCoNiCrMn high-entropy alloy system, Acta Mater. 62 (2014) 105-113.

[30] C. Wang, W. Ji, Z. Fu, Mechanical alloying and spark plasma sintering of CoCrFeNiMnAl high-entropy alloy, Adv. Powder Technol. 25 (2014) 1334-1338.
[31] W. Ge, B.Wu, S. Wang, S. Xu, C. Shang, Z. Zhang, and Y. Wang, Characterization and properties of CuZrAlTiNi high entropy alloy coating obtained by mechanical alloying and vacuum hot pressing sintering. Adv. Powder Technol. 28 (2017) 2556-63.
[32] Y. Xie, H. Chang, Q.Tang, W. Chen, W. Chen, and P. Dai, Effects of N addition on microstructure and mechanical properties of CoCrFeNiMn high entropy alloy produced by mechanical alloying and vacuum hot pressing sintering. Intermetallics 93 (2018) 228-34.
[33] H.Cheng, W. Chen, X. Liu, Q. Tang, Y. Xie, and P. Dai, Effect of Ti and C addition s on the microstructure and mechanical properties of the FeCoCrNiMn high-entropy alloy. Mater. Sci. Eng, A 719 (2018) 192-8.
[34] S. Varalakshmi, M. Kmaraj, and B.s. Murty, Processing and properties of nanocrystalline CuNiCoZnAlTi high entropy alloys by mechanical alloying. Mater. Sci. Eng. A 527 (2010) 1027-30.
[35] Z. Fu, W. Chen, Z. Chen, H. Wen, and E. J. Lavernia, Influence of Ti addition and sintering method on microstructure and mechanical behavior of a medium-entropy Al0.6CoNiFe alloy. Mater. Sci. Eng. A 619 (2014) 137-45.
[36] V. Shivam, J. Basu, Y. Shadangi, M.K. Singh, and N.K.K. Mukhopadhyay: Mechano-chemical synthesis, stability and phase evolution in AlCoCrFeNiMn high entropy alloy. J. Alloys Compd, 757 (2018) 87-97.
[37] S. Varalakshimi, G. Appa Rao, M. Kamaraj, and B.S. Murty: Hot consolidation and mechanical properties of Nano crystalline equiatomic AlFeTiCrZnCu high entropy alloy after mechanical alloying. J. Mater. Sci. 45 (2010) 5158-63.
[38] S. Praveen, B. S. Murty, and R. S. Kottada: Alloying behavior in multi-component AlCoCrCuFe and NiCoCrCuFe high entropy alloys. Mater. Sci. Eng, A 534 (2012) 83-9.
[39] M. Vaidya, M. Murakhnshina Garlopal: High-entropy alloys by mechanical alloying: A review, Mater. Res. 34 (2019) 664-86.
[40] S. Praveen, A. Anupam, T. Sirasani, B. S. Murty, and R. S. Kottada: Characterization of oxide dispersed AlCoCrFe high entropy alloy synthesized by mechanical alloying and spark plasma sintering. Trans. Indian Inst. Met. 66 (2013) 369-73.
[41] E. Colombini, R. Rosa, L. Trombi, M. Zadra, A. Casagrande, and P. Veronosi, Hugh entropy alloys obtained by field assisted powder metallurgy route: SPS and microwave heating. Mater. Chem. Phys. 210 (2018) 78-86.
[42] C. Wang, Wei Ji, Zhengyi Fu: Mechanical alloying and spark plasma sintering of CoCrFeMnNiAl high-entropy alloy, Advanced Powder Technology. 25 (2014) 1334-8.
[43] H. Prasad, Sh, Singh, B. B. Panigrahi: Mechanical activated synthesis of Alumina dispersed FeNiCoCrAlMn high entropy alloy. J. Alloys Compd, 692 (2017) 720-6.
[44] J.W. Yeh, S.J. Lin, Breakthrough applications of high-entropy materials. J. Mater. Res. 33 (2018) 3129-37.
[45] L. QH, Y. TM, G. ZN, et al. Microstructure and corrosion properties of AlCoCrFeNi high entropy alloy coatings deposited on AISI 1045 steel by the electrospark process. Metal Mater Trans A. 44 (2012) 1767-1778.

JMATPRO	Journal of Advanced Materials and Processing 10 (1): 39-56, Winter 2022 http://jmatpro.iaun.iau.ir 20.1001.1.2322388.2022.10.1.4.7

Research Paper

Evolution of Biological Properties of Bioactive Diopside and Wollastonite for Bone Tissue Engineering

Ruhollah Zamani Foroushani[1], Ebrahim Karamian[1*], Mohammad Rafienia[2]

1. Advanced Materials Research Center, Department of Materials Engineering, Najafabad Branch, Islamic Azad University, Najafabad, Iran

2. Biomaterial, Nanotechnology and Tissue engineering Department of Advanced Medical Technology, Isfahan University of Medical Sci-ences, Isfahan, Iran

ARTICLE INFO

Article history:

Received 26 November 2021
Accepted 29 December 2021
Available online 1 January 2022

Keywords:
Bioactivity
Biomineralization
Cell responses
Diopside
Wollastonite

ABSTRACT

The present study aimed to synthesize and characterize diopside ($CaMgSi_2O_6$) and wollastonite ($CaSiO_3$) nano-bioceramics via a combination of mechano-chemical and calcination processes. In vitro biomineralization and cell responses of wollastonite and diopside were carried out using simulated body fluid (SBF) for up to 28 days and MG-63 osteoblast cells. Results revealed excellent tissue biomineralization of wollastonite and diopside through generating an apatite-like layer on the surface of nano-bioceramics. Wollastonite and diopside cell responses eventuated non-cytotoxicity by MG-63 osteoblast cells, and their viability and cell proliferation were verified. Results of alizarin red staining and alkaline phosphate enzyme of diopside and wollastonite evidenced great bioactivity and tissue biomineralization with respect to the release of Ca^{2+} and high absorption related to calcium activity, and high activity and growth of alkaline phosphate enzyme to repair bone tissue of diopside, and wollastonite was enhanced in contact with the MG-63 osteoblast cells. Regarding the addition of Mg^{2+} into the calcium-silicate network for the chemical stability network to improve biological properties, results of biological assays verified that diopside possessed high biological and cell responses in comparison to wollastonite; and both of them can be suggested as great bioactive and biocompatible candidates for biomedical applications.

Citation: Zamani Foroushani, R.; Karamian, E.; Rafienia, M. (2022) Evolution of Biological Properties of Bioactive Diopside and Wollastonite for Bone Tissue Engineering, Journal of Advanced Materials and Processing, 10 (1), 39-56.
Dor: 20.1001.1.2322388.2022.10.1.4.7

* **Corresponding Author**
E-Mail Address: karamian1970@gmail.com

1. Introduction

To restore bone defects is a significant challenge in medical and biomedical sciences, and finding alternative materials for bone tissues is vital. Calcium silicates ($CaSiO_3$ and Ca_2SiO_4) and calcium silicate-based ceramics have become the principal focus of biomaterials [1, 2]. The materials possess biological properties such as bioactivity and enhancement of cell interactions compared to traditional calcium phosphates like hydroxyapatite (HAp) or β–tricalcium phosphate [3]. Therefore, they are promising candidates as bone graft materials. Moreover, incorporating metal atoms (Mg, Zn, and Zr) into the crystalline structure of calcium silicates has improved their biological revenue [4-7]. In fact, silicate biomaterials, including wollastonite and Ca–Si–M ternary ceramics (M = Ti, Mg, Zn and Zr) are the topic of many research projects for bone tissue restoration usages. A significant feature of silicate biomaterials is their ability to release the silicon (Si) ion which persuades the growth and distinction of osteoblast cells to some extent [8-10]. Additionally, a precise study of $CaO–SiO_2$ ceramics showed their direct connection with bone. The study showed that ceramics including CaO and SiO_2 have suitable bioactivity and connection power to bone [9]. Recently, an extension of $CaO–SiO_2–MgO$ ceramics with diopside ($CaMgSi_2O_6$) topic has found special consideration in biomaterials applications, and diopside has currently been identified as a bioactive bioceramic. It was reported [10, 11] that the presence of magnesium (Mg) in the $CaO–SiO_2$ system by using diopside as a biomaterial. The chemical composition of diopside is similar to akermanite ($Ca_2MgSi_2O_7$). However, it possesses a lower degradability rate compared to akermanite and wollastonite. In addition, in the chemical composition of diopside, the calcium atom is replaced by a magnesium atom, and Mg–O bond is developed [11-13].

Since the Mg–O bonding energy is higher than that of the Ca–O bonding, the stability of the crystalline structure is increased [12]. On the other hand, the $CaO–SiO_2–MgO$ ceramic systems are appropriate for bone regeneration applications [13].

It was reported [14] that the mechanism of bioactivity of $CaO–SiO_2–MgO$ system ceramics is similar to silicate glass, which is related to the direct release of the Si ions. One of the significant bioceramic compounds is wollastonite ($CaSiO_3$), which has unique characteristics such as thermal stability and high hardness. Therefore, it has acquired abundant applications in the ceramic industry [15]. In addition, wollastonite possesses high bioactivity, so apatite layers appear on it and grow fast only after 3 days. Besides, the growth rate of the hydroxyapatite in nano-structured wollastonite was more than its growth rate in micro-structured wollastonite [16]. One of the most interesting synthesis processes of nano-structured bio-ceramics is mechano-chemical process. The particle sizes of nano-structured materials are less than 100 nm [17]. Due to their ideal physical and chemical properties, they attract much attention from scientific and research communities [18]. In the research, cell responses of MG-63 osteoblast cells, bio-mineralization, calcium activity, and alkaline phosphatase enzyme behavior on synthesized diopside ($CaMgSi_2O_6$) and wollastonite ($CaSiO_3$) nano-bioceramics via a combination of mechano-chemical and calcination processes were surveyed for biomedical applications.

2. Materials and methods

2.1. Raw materials

Calcium carbonate powder ($CaCO_3$) (Merck, Germany), silica (SiO_2) (Merck Co., Germany), and magnesium oxide (MgO) (Merck Co., Germany) were used to synthesize diopside and wollastonite compounds.

2.2. Synthesis of diopside and wollastonite

To synthesize diopside, 15.38 wt.% of MgO, 46.15%wt of SiO_2, and 38.46%wt of $CaCO_3$ were chosen, and then mechano-chemical process (ball milling) was carried out. In this process, ball–to–powder weight ratio and milling speed were 10:1 and 350 rpm, respectively, and the milling times were 5 min, 10 h and 20 h. Then, the developed powders were calcinated at 1200 °C for 2 h [19]. Similarly, the process was conducted to synthesize wollastonite, and the milling times were 5 min, 10 h and 20 h. The raw materials included 37.5 wt.% of SiO_2, 62.5 wt.% of $CaCO_3$, and the molar ratio was 1.125. The milling speed and ball–to–powder weight ratio were 350 rpm and 10:1, respectively. After this process, the milled powders were calcinated at 1200 °C for 2 h [19].

It is worth noting that steel cups with WC coating and zirconia balls were utilized to conduct the mechanochemical process in the study. In addition, the synthesized compounds were converted to bulk compounds by pressing compounds via a press device (pressure of 300 MPa) and a cylindrical mold (diameter of 5mm and height of 7.5mm). Fig. 1 depicts the mechanism of synthesis of the wollastonite and diopside nano-bioceramics.

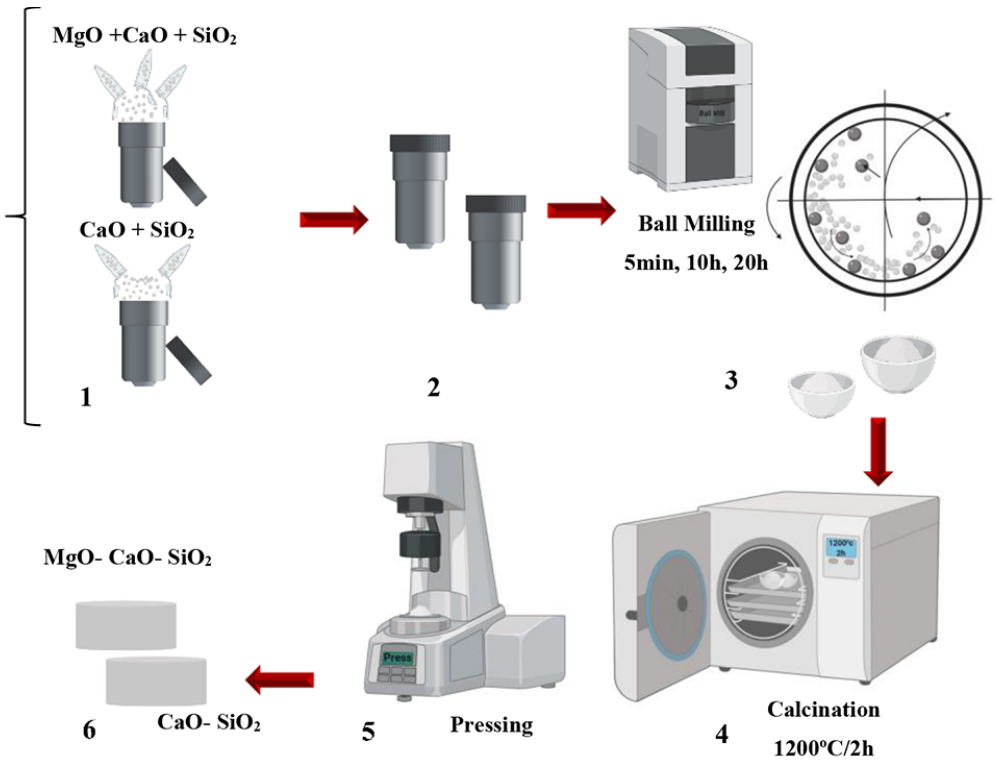

Fig. 1. The mechanism of synthesis of the diopside and wollastonite nano-bioceramics

Table 1. Calculated values of crystallite size by the Scherrer method: (a) diopside and (b) wollastonite

(a)

2θ	Cos(θ)	FWHM	β	D
27.58	0.971	0.1476	0.0025	55
29.86	0.966	0.1968	0.0034	41
30.31	0.965	0.1476	0.0025	56
41.89	0.933	0.1968	0.0034	43
44.37	0.925	0.2460	0.0042	35

(b)

2θ	Cos(θ)	FWHM	β	D
25.987	0.97	0.1476	0.0025	61
27.55	0.971	0.1968	0.0034	47
31.83	0.961	0.1968	0.0034	47
45.88	0.92	0.1968	0.0034	49

2.3. Characterization of diopside and wollastonite

To evaluate the phase structure of the milled and calcinated powders, XRD patterns of these samples were prepared using a PW3040 Philips X-ray diffractometer. The XRD patterns of the samples were obtained via Cu-Kα radiation with a wavelength $\lambda = 1.54018\ A°$ in the ranges of 15–70, 10–60 and 10–50 degrees. To determine the crystallites size of the developed compounds, the width of the present peaks was used in the XRD patterns and Scherrer method. The Scherrer equation [20] is presented as follow:

$$\beta Cos\theta = \frac{K\lambda}{D} \quad (1)$$

where D is the crystallite size, λ is the wavelength, K is the shape factor (about 1), β is the full width at half maximum (FWHM), and θ is half the diffraction angle. To investigate the morphology and micro-structure of the synthesized diopside and wollastonite, scanning electron microscopy (SEM; FEI, Quanta, USA) images were prepared. To examine the chemical composition and distribution of elements of the synthesized diopside and wollastonite compounds, EDS analysis was prepared. To examine the micro-structure and nano-structure of the synthesized diopside and wollastonite, transmission electron microscopy (TEM; EM 208, Philips, the Netherlands) images of the samples were prepared.

2.4. Biomineralization and cell responses

The evaluation of biomineralization and formation of an apatite-like layer on the diopside and wollastonite nano-bioceramics surface was conducted via SBF

solution provided according to the Kokubo method [21]. The nano-bioceramic samples were immersed in 25 ml of the SBF solution (pH=7.4) and were put into an incubator at 37 ℃ for 28 days. After the immersion of the samples for this period, they were washed with distilled water and dried in an oven at 50 °C for 48 h.

The cytotoxicity evaluation was conducted according to ISO 10993-5 standard. The sterilization of the wollastonite and diopside particles was performed in an autoclave. Subsequently, the particles were immersed in Dulbecco's modified eagle medium (DMEM) culture medium using ultrasonic irradiation for 30 min. The MG-63 osteoblast cells (6000 cells) were put into a 24-well plate (TCPS or tissue culture polystyrene) in contact with the culture medium containing the wollastonite and diopside particles. To investigate the cell viability, MTT assay was conducted at 1, 3 and 7 days. Then, the medium was washed with PBS solution, and about 400 µl of the medium and 40 µl of the MTT solutions (5 mg/ml) were added to the culture well, which was kept in an incubator at 37 ˚C for 240 min. The medium was evacuated so that the formazan could be dissolved, and 200 µl of dimethyl sulfoxide (DMSO) was added to the wells. Optical absorption was evaluated over 570 nm.

To examine the deposited calcium rate by the MG-63 osteoblast cells, alizarin red staining was used for 7 and 14 days. After culturing the MG-63 osteoblast cells for 7 and 14 days, the cells were fixed with formaldehyde (4%), and then the prepared alizarin red staining (1%) was added to Tris buffer solution with pH=8 for 15 min. The well plate containing cells was washed with PBS solution several times.

To investigate the alkaline phosphatase enzyme activity rate at 3, 7 and 14 days of cell culture on the diopside and wollastonite compounds, at first, the Ripa solution was used in the entire protein extraction. After extracting the perfect cell culture, 20 µl of the Ripa solution was poured on the bioceramics, and they were pipetted for 10 min. The Ripa solution was centrifuged at 14000 rpm for 10 min and was kept at 4 °C. Afterwards, for each 20 µl of Ripa solution, 1 mM of reagent No.1 of kit of alkaline phosphatase was added to the samples, and they were put into the incubator at 37 °C for 1 min. Then, 250 µl of reagent No.2 was added to the samples, and the same process was repeated. After 1, 2, and 3 min, optical absorption was read over 405 nm, and then its difference was determined from the last minute. Finally, these three differences and their mean were calculated, and the final number was multiplied by the factor 3433.

2.5. Statistical analysis

The experiments were performed for n=3. All data were suggested as mean ± SD. One-way analysis of variance (ANOVA) was used to compare the results. A p-value of less than 0.05 was determined to be statistically significant.

3. Results and discussion

Figs. 2a-c present the XRD patterns of the milled powders of materials like MgO, $CaCO_3$ and SiO_2 at 5 min, 10 h, and 20 h. In Fig. 2a, the milled powers at 5 min, only magnesium oxide (MgO) (JCPDS 01–087–0652) and calcium carbonate ($CaCO_3$) phase (JCPDS 01–081–2027) were observed, and by extending the milling time for 10 h (Fig. 2b), the peaks widened. The phenomenon is due to the decrease in the crystallite size and the increase in the lattice strain during the mechano-chemical process. By extending the milling time for 20 h, because the raw materials became amorphous, the peaks related to the calcium carbonate phase gradually decreased (Fig. 2c, milling time=20 h). In the mechano-chemical (ball milling) process, much energy is applied to the powder particles, and internal energy (ΔU) is highly increased. A lot of strains in the system present serious motion of dislocations, causing different structural defects like dislocations, vacancies, stacking fault, and increasing the development of grains boundary. Finally, these changes increase the speed of the reactions between the milled particles. The transformation of the milled powder structure is so high that the primary lattice is perfectly altered. During the milling process, various phenomena like mixing and chemical reactions in contact with particle levels might occur, causing chemical reactions to take place during the milling process and the reactivity of the milled product to increase [22].

The main peaks of SiO_2 phase are not identifiable in the ranges of diffracted angles of 20–30 degrees in the XRD patterns (Figs. 2a-c). As a result of the milling process for 20 h (Fig. 2c), the pattern lacked the diopside phase ($CaMgSi_2O_6$). Subsequently, to develop the diopside phase, the milled powders were calcinated at 1200 ℃ for 2 h.

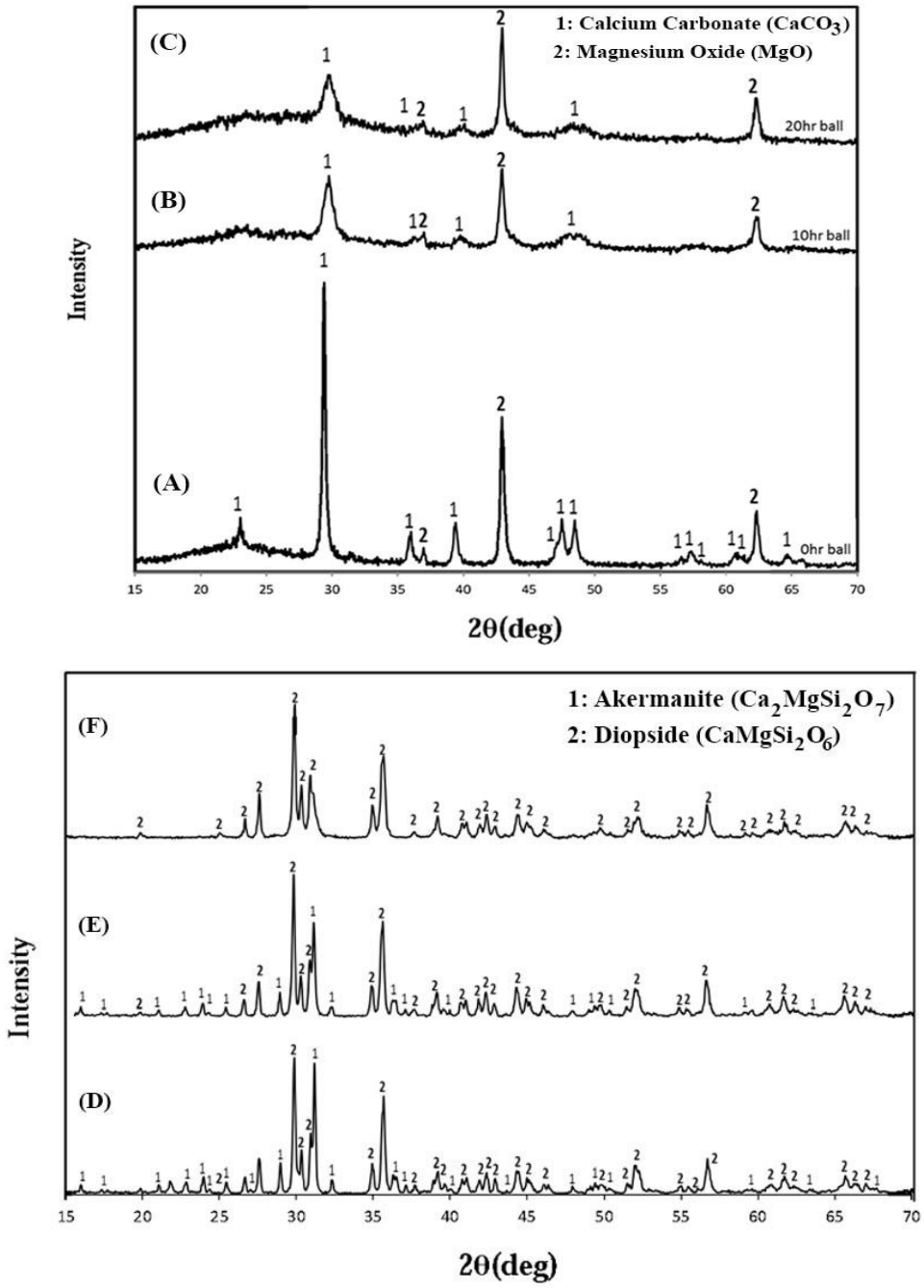

Fig. 2. XRD patterns of the milled powders among raw materials related to the diopside phase: (a) 5 min, (b) 10 h, and (c) 20 h, XRD patterns of the sintering process of the milled powders at 1200 ℃ for formation of diopside phase: (d) 5 min, (e) 10 h, and (f) 20 h

Figs. 2d-f presents the XRD patterns of the calcination process of the milled powders at 5 min, 10 h, and 20 h at 1200 ℃. In the calcinated sample of the milled powder at 5 min (Fig. 2d), the diopside ($CaMgSi_2O_6$) phase (JCPDS 01–071–1494) with mono-clinic structure was developed, and akermanite ($Ca_2MgSi_2O_7$) phase (JCPDS 01–077–1149) with a tetragonal structure was observed in the XRD pattern of this sample (Fig. 2d).

In the calcinated sample of the milled powder at 10 h (Fig. 2e), the peaks related to the diopside phase increased, and those related to the akermanite phase decreased (Fig. 2e). In the calcinated sample of the milled powder at 20 h (Fig 2f), the pattern lacked the akermanite phase, and only the diopside phase was clearly observed because of appropriate milling time (20 h) among the raw materials. Formation of the diopside phase is according to relations 2 and 3:

$$CaCO_3 \rightarrow CaO + CO_2 \quad (2)$$

$$CaO + 2SiO_2 + MgO \rightarrow CaMgSi_2O_6 \quad (3)$$

To obtain the optimum milling time, the milling process was conducted among raw materials like $CaCO_3$ and SiO_2 for 5 min, 10 h and 20 h. Figs. 3a-c indicated the XRD patterns related to the milled powders at 5 min, 10 h and 20 h. In the XRD pattern in Fig. 3a, only the phases related to the raw materials like $CaCO_3$ exist, and by increasing the milling time to 10 h, the peaks widen (Fig. 3b) because of a

decrease in the crystallite size and an increase in the lattice strain during the milling process [23]. In this pattern (Fig. 3b), only the phase related to the raw materials compound was observed. By increasing the milling time to 20 h (Fig. 3c), because the raw materials became amorphous, some peaks related to $CaCO_3$ phase were gradually removed and were increased 20–30 degrees. The main peaks of the SiO_2 phase were in the diffracted angles of 20–30 degrees, which was not identifiable in the XRD patterns (Figs. 3a-c). The patterns lacked the wollastonite phase. Figs. 3d-f exhibited the XRD patterns of the calcination process of the milled powders (5 min, 10 h and 20 h of the milling time) at 1200 ℃ for 2 h.

In Figs. 3d,e, the wollastonite ($CaSiO_3$) phase (JCPDS 01-073-1110) and rankinite phase ($Ca_3Si_2O_7$) (00-011-0317) were observed because of extending the milling time to 20 h among the raw materials. The formation of the wollastonite phase is according to relations 2 and 4.

$$CaO + SiO_2 \rightarrow CaSiO_3 \quad (4)$$

To calculate the crystallite size of the synthesized diopside and wollastonite, the Scherrer method was used. Table 1 presents the calculated values for the synthesized diopside and wollastonite obtained by calcination and mechano-chemical processes (milling time: 20 h). According to the results, the mean crystallite sizes of diopside and wollastonite nano-bioceramics were 46 and 51 nm, respectively.

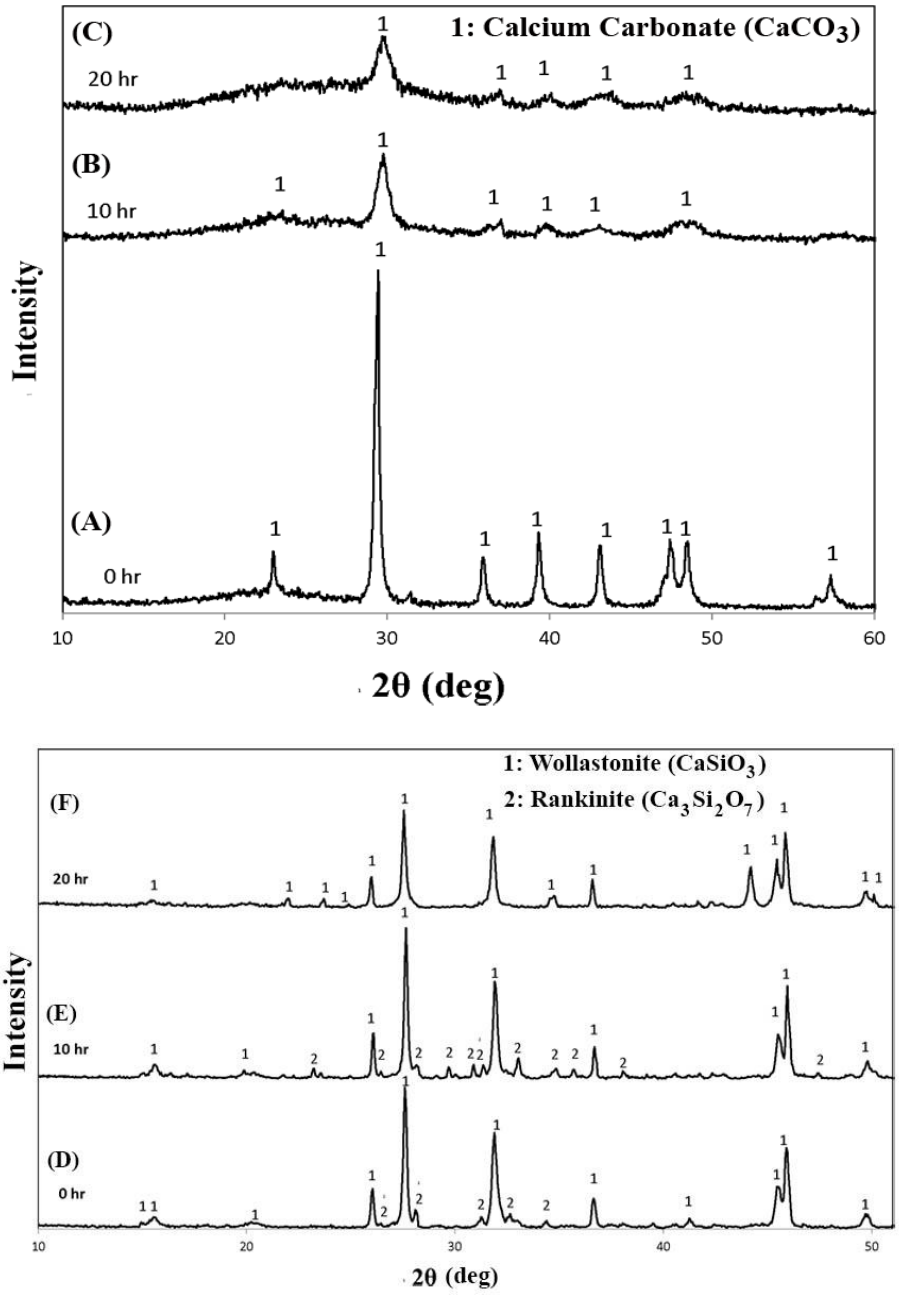

Fig. 3. XRD patterns of the milled powders among raw materials related to the wollastonite phase: (a) 5 min, (b) 10 h, and (c) 20 h, XRD patterns of the sintering process of the milled powders at 1200 ℃ for wollastonite phase formation: (d) 5 min, (e) 10 h, and (f) 20 h

Fig. 4a presents the morphology related to the synthesized diopside. In the SEM image, the diopside structure is continuously in a trapezoidal shape. According to Fig. 4b and Table 2, the results of EDX analysis of the synthesized diopside showed that oxygen (O), silicon (Si), calcium (Ca) and magnesium (Mg) elements are the constituent elements of diopside. They also proved the non–availability of the synthesized compound. Additionally, there are Mg^{2+}, Si^{4+}, and Ca^{2+} ions, meaning that as a result of the milling process, proper primary distribution of the raw materials occurred, causing uniform diopside to develop.

Fig. 4c presents the morphology relevant to the synthesized wollastonite. The SEM image showed the morphology of the wollastonite structure continuously in a plate shape. According to Fig. 4d and Table 3, the EDX results of the synthesized wollastonite showed that oxygen (O), silicon (Si), and calcium (Ca) were the constituent elements of the wollastonite, and its non– availability was proved by the EDX analysis. It reveals that Si^{4+} and Ca^{2+} ions exist, showing an appropriate primary distribution among the raw materials after the milling process, which made uniform wollastonite.

(a)

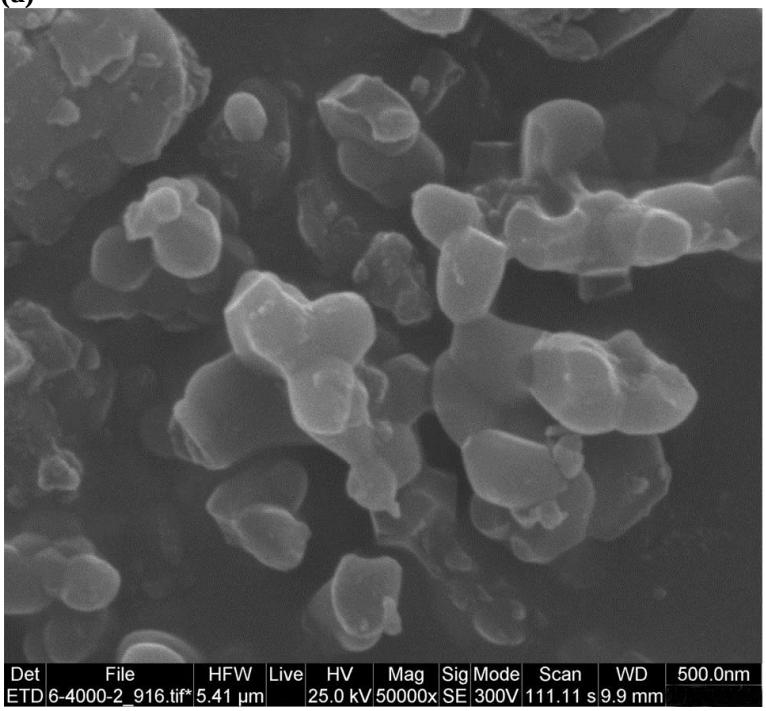

(b)

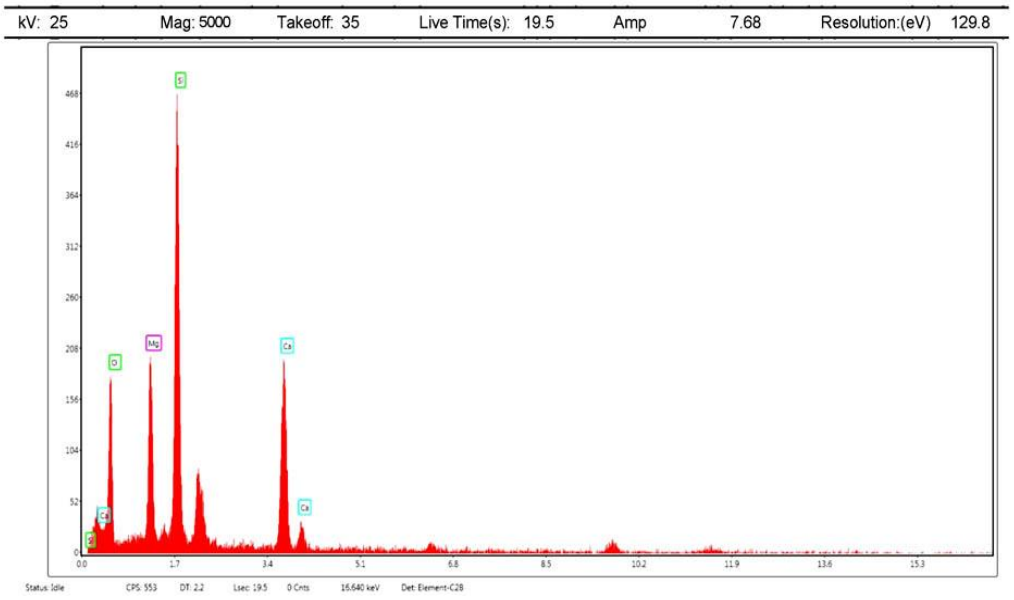

(c)

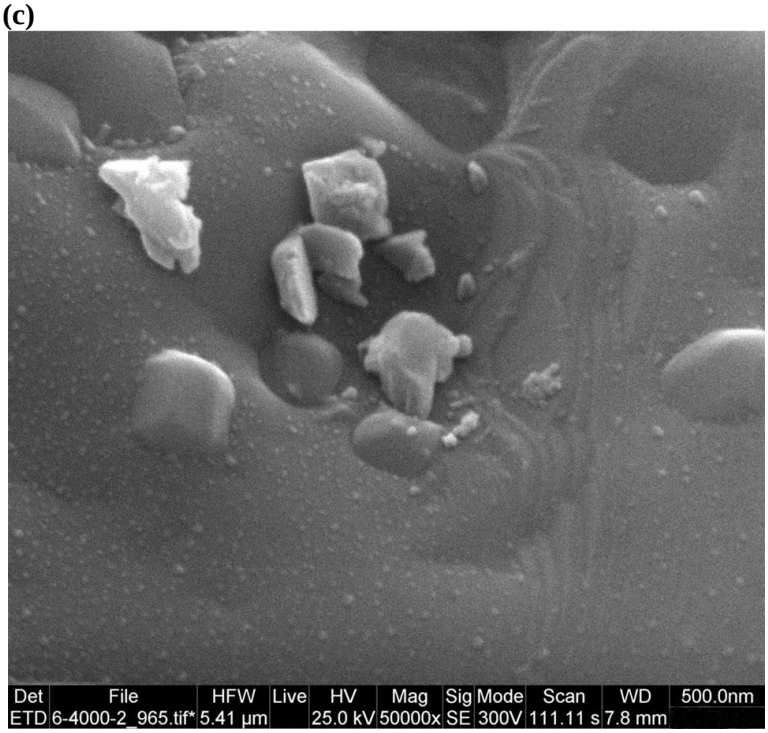

(d)

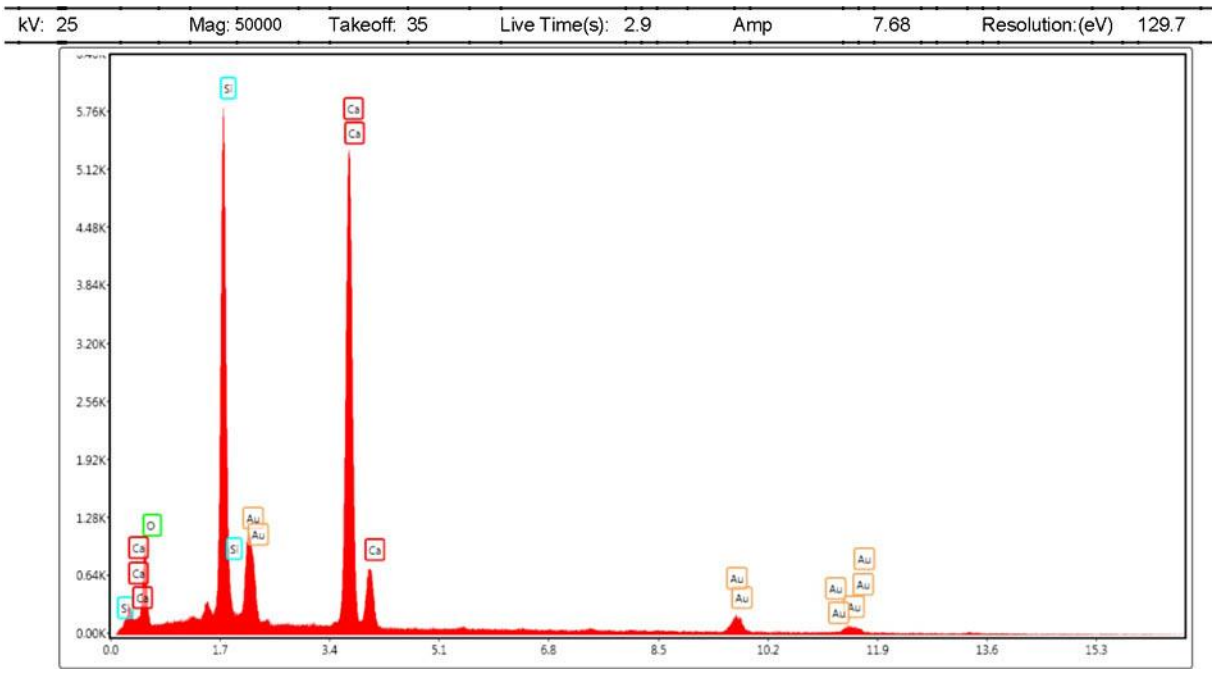

Fig. 4. (a) SEM image of diopside, (b) EDX analyis of diopside, (c) SEM image of wollastonite and (d) EDX analysis of wolastonite

Table 2. Results of EDX analysis of synthesized diopside

Element	Weight%	Atomic %	Net Int.
O	41.79	56.95	68.47
Mg	14.46	12.97	86.53
Si	27.02	20.98	211.76
Ca	16.73	9.1	109.25

Figs. 5a-c exhibited the TEM images of the synthesized diopside in which the particle sizes of the diopsides were smaller than 100 nm. TEM images showed the formation of interconnected agglomerates, and the range of nanostructure was observed. In other words, TEM images suggested

that the real size of the diopside was less than 80 nm. However, it can be stated that the average size was about 80 nm due to developing larger particles as a result of particle agglomeration. It can be concluded that the synthesis of diopside nano-bioceramic by combining mechano-chemical and calcination processes is successful.

(a)

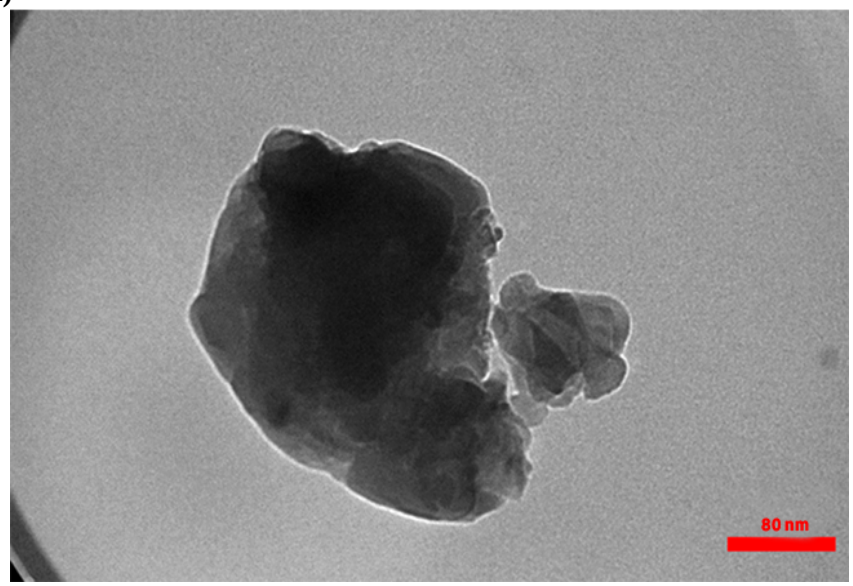

(b)

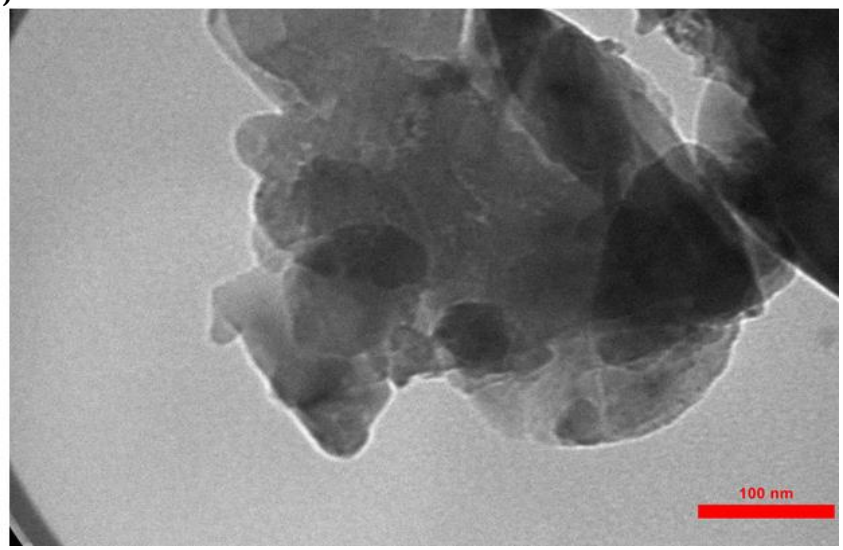

(c)

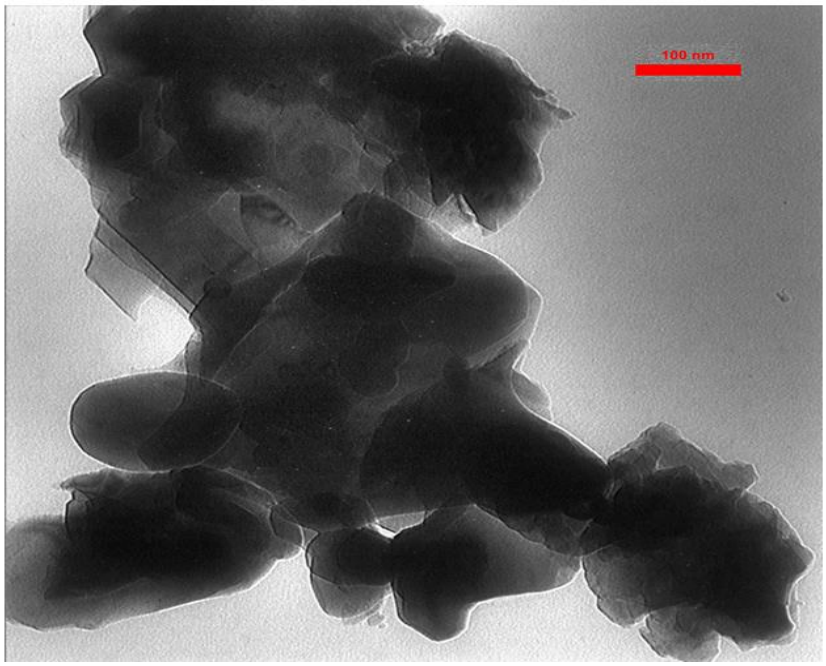

Fig. 5. TEM images of diopside

Table 3. Results of EDX analysis of synthesized wollastonite

Element	Weight%	Atomic %	Net Int.
O	26.44	48.56	2583.16
Si	21.06	22.03	18004.71
Ca	36.95	27.09	22010.61
Au	15.54	2.32	1217.38

Figs. 6a,b illustrate the TEM images of the synthesized wollastonite in which the sizes of the wollastonite were smaller than 100 nm. TEM images showed the development of connected agglomerates, and the range of nanostructure was observed. Moreover, TEM images of the wollastonite indicated that the actual size of wollastonite was almost less than 80 nm. In other words, it can be expressed that the mean size was about 80 nm because of the formation of larger particles resulting from particle agglomeration. It can be concluded that the synthesis of wollastonite nano-bioceramic using a combination of mechano-chemical and calcination processes is successful.

(a)

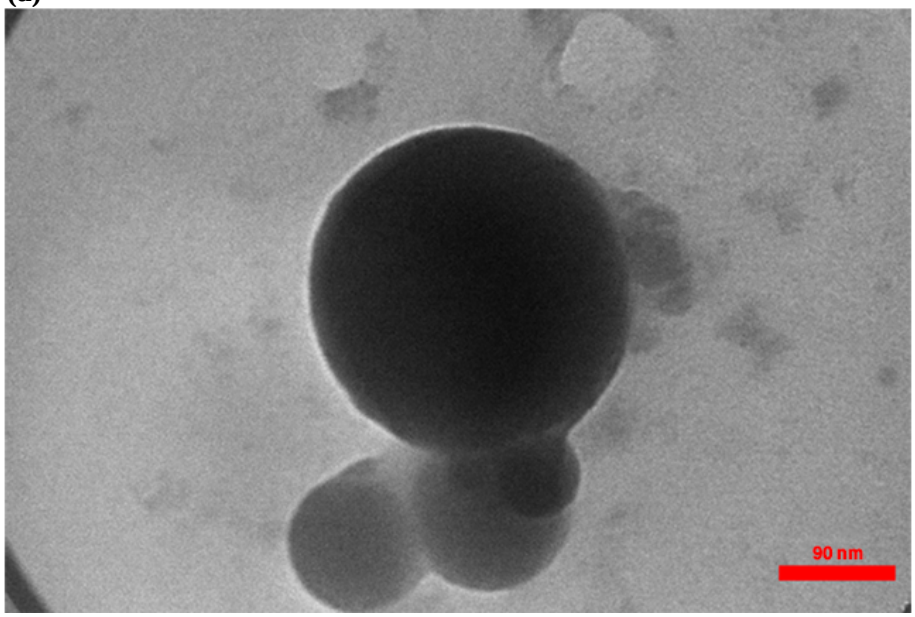

(b)

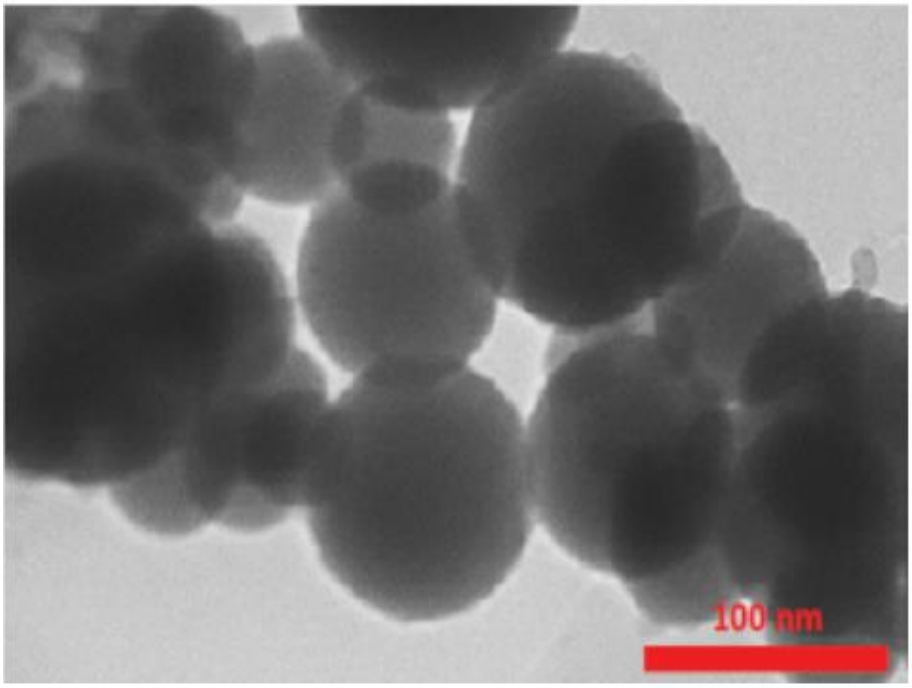

Fig. 6. TEM images of wollastonite

Table 4. Results of the EDX analysis of the synthesized wollastonite bio-mineralization

Element	Weight %	Atomic %	Net Int.
O	46.31	65.68	45.68
P	23.58	17.05	168.82
Ca	30.11	18.28	177.6

Fig. 7a presents the SEM image of wollastonite nano-bioceramic immersed in SBF for up to 28 days and suggests the development of an extensive apatite-like layer on the surface of wollastonite. The EDX analysis (Fig. 7b and Table 4) confirms the presence of Ca, P, and O. Finally, it proves the development of a $CaO\text{-}P_2O_5$ film on the surface of the nano-bioceramic. Actually, the EDX analysis expresses high values related to P and Ca, resulting in the creation of an apatite-like layer on the surface of wollastonite. Fig. 7c shows the SEM image of diopside nano-bioceramic immersed in SBF for up to 28 days, and Fig. 7c depicts the development of an apatite-like layer on the surface of the diopside. The issue was confirmed via EDX analysis (Fig. 7d and Table 5), which presented a high atomic percentage of Ca and P, proving the development of a $CaO\text{-}P_2O_5$ film on the surface of the diopside nano-bioceramic. It can be discussed that Ca^{2+} and Mg^{2+} cause hydrolysis reaction of the silica group to be conducted, generating the initial apatite crystals, and causing the Ca^{2+} and Mg^{2+} ions to be released. The ions migrated to the silica surface, and finally, a $CaO\text{-}P_2O_5$ film was developed on the silica surface, and apatite crystals were nucleated [24, 25]. Concerning the discussions, it is concluded that wollastonite and diopside are bioactive nano-bioceramics that can possess bone tissue bio-mineralization for bone tissue engineering applications.

(a)

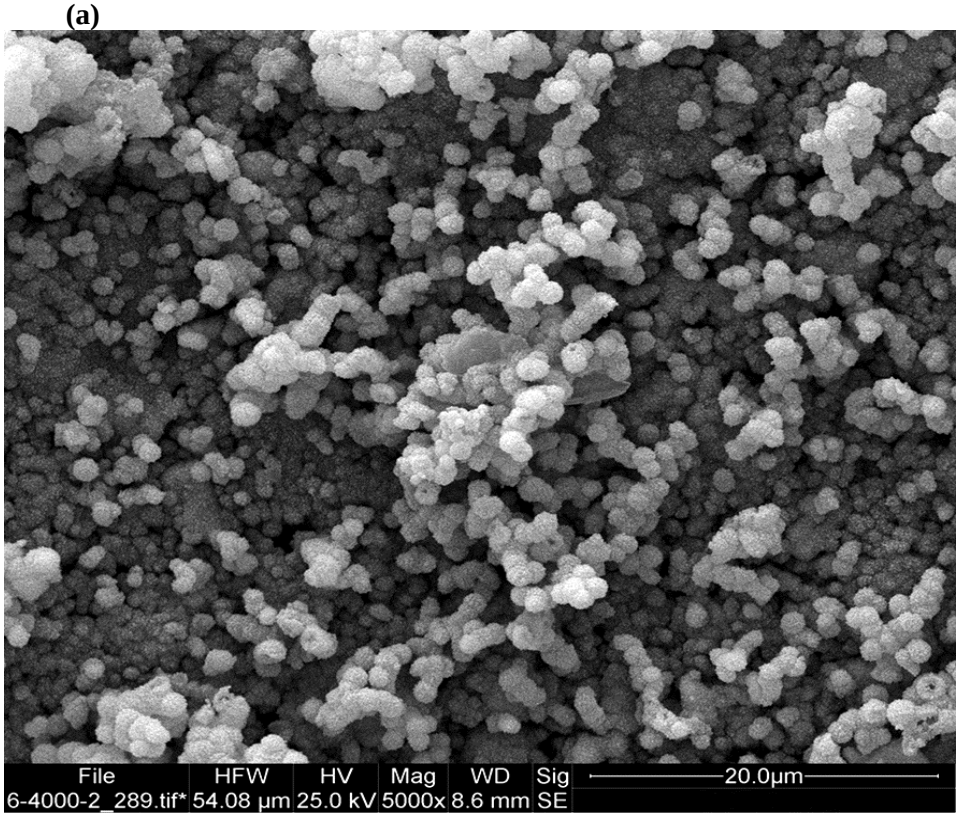
File
6-4000-2_289.tif*
HFW
54.08 µm
HV
25.0 kV
Mag
5000x
WD
8.6 mm
Sig
SE
20.0µm

(b)

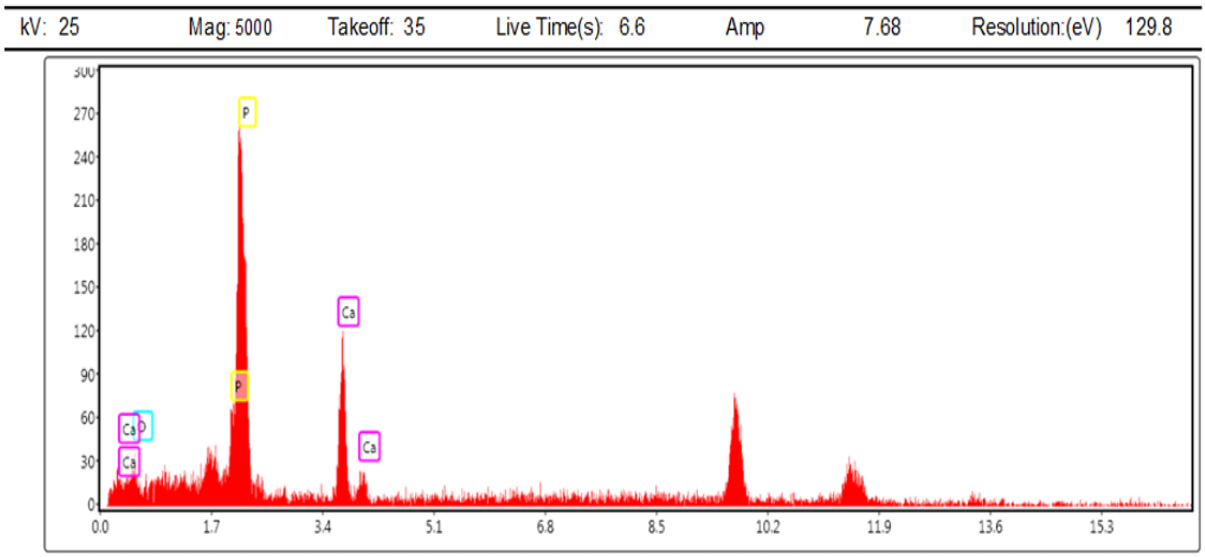
kV: 25
Mag: 5000
Takeoff: 35
Live Time(s): 6.6
Amp
7.68
Resolution:(eV)
129.8
P
Ca
P
Ca
Ca
O
Ca
0.0
1.7
3.4
5.1
6.8
8.5
10.2
11.9
13.6
15.3

(c)

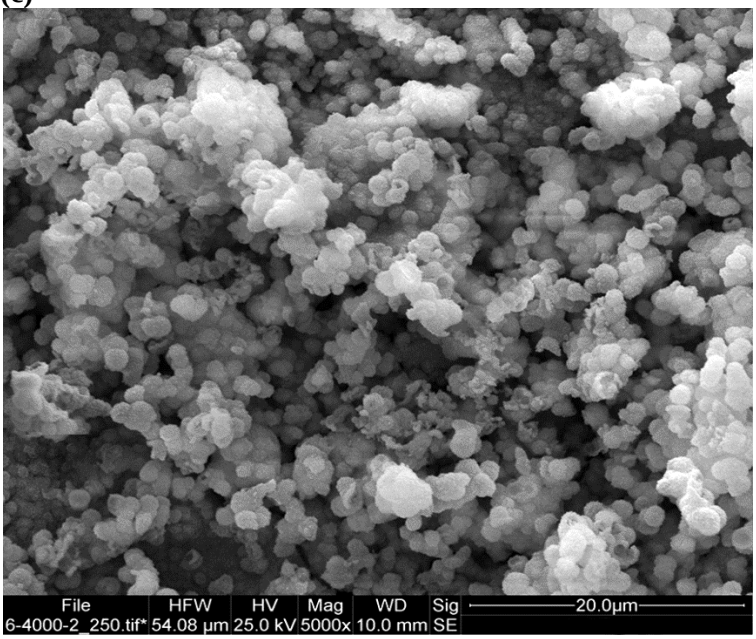

(d)

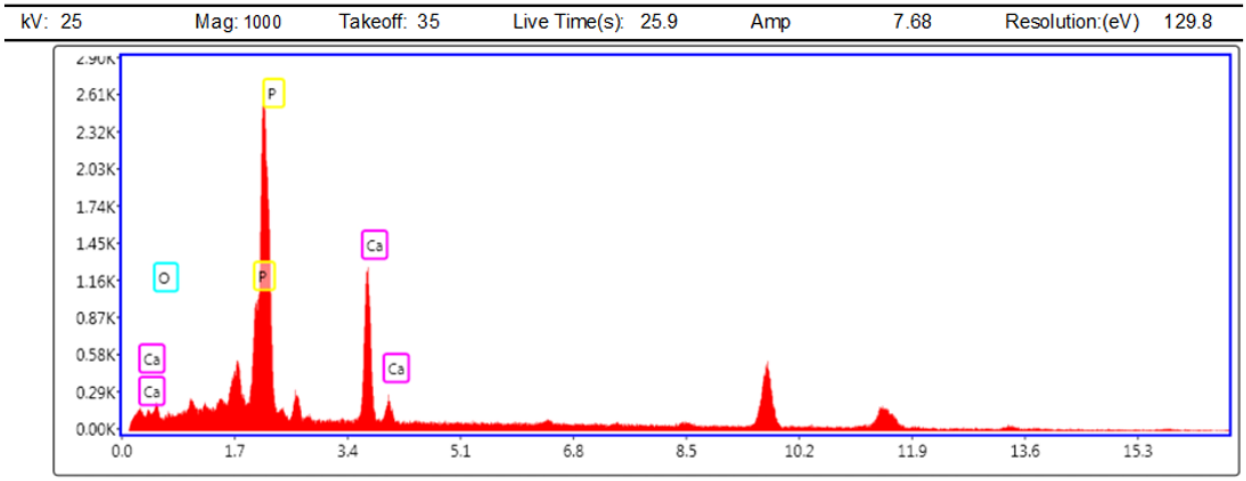

Fig. 7. (a) SEM image of wollastonite in immersed SBF for up to 28 days, (b) EDX analysis, (c) SEM image of diopside immersed in SBF for up to 28 days, (d) EDX analysis

Table 5. Results of the EDX analysis of the synthesized diopside bio-mineralization

Element	Weight %	Atomic %	Net Int.
O	36.59	56.08	80.53
P	28.41	21.42	497.56
Ca	35.1	23.76	559.6

Fig. 8 depicts the mechanism of apatite formation. Generally, morphology related to apatite crystals is in the form of needle-like and cauliflower-like shapes on the surface of the nano-bioceramics. On the other hand, EDX analyses showed that Ca, P, and O elements indicate the formation of Ca–P–O on the surface of the nano- bioceramics. With regard to SEM images and EDX analyses, it can be concluded that the development of an apatite-like layer and apatite crystals on the surface of the nano-wollastonite and nano-diopside was carried out correctly. This issue clearly presents the bioactivity of the synthesized compounds.

Fig. 9 shows the results of cell viability of wollastonite and diopside nano-bioceramics. The cell viability assay related to nano-bioceramics was conducted by utilizing MG-63 osteoblast cells and 1, 3, and 7 days of cell culture. It suggests a meaningful difference ($p<0.05$) in the cell viability of nano-bioceramics. Cell viability and proliferation of MG-63 osteoblast cells enhanced after 7 days. It verified the compatibility cells of wollastonite and diopside

due to stimulating the MG-63 osteoblast cells via wollastonite and diopside, an effective factor for the enhancement of cell growth, viability, and proliferation. Moreover, nano-bioceramics lacked cytotoxicity by the MG-63 osteoblast cells.

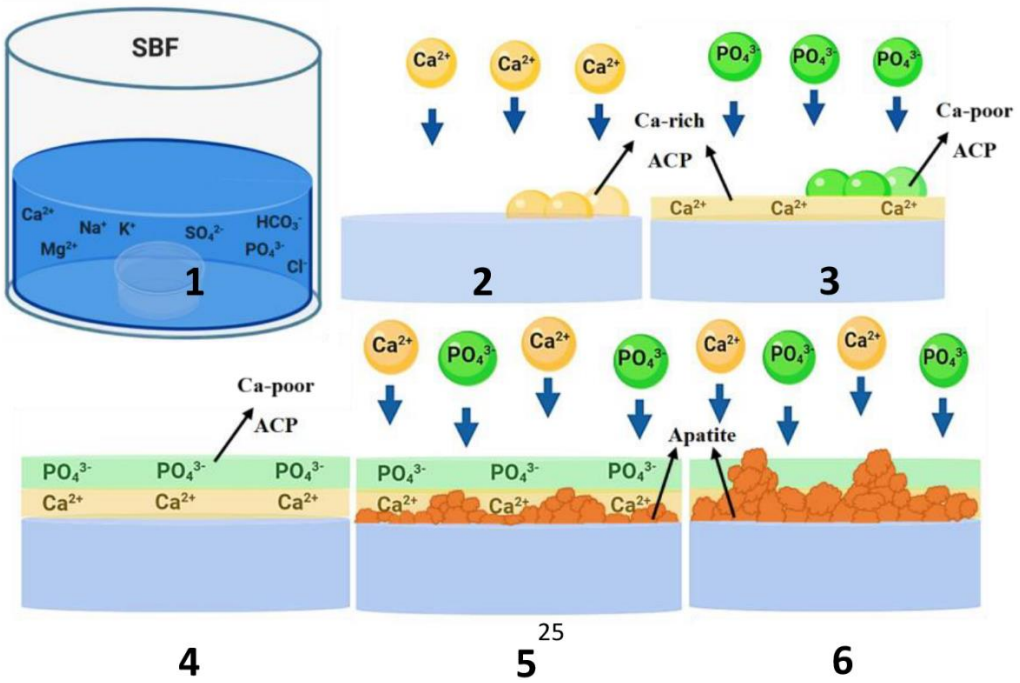

Fig. 8. The mechanism of apatite formation on bioactive diopside and wollastonite nano-bioceramics

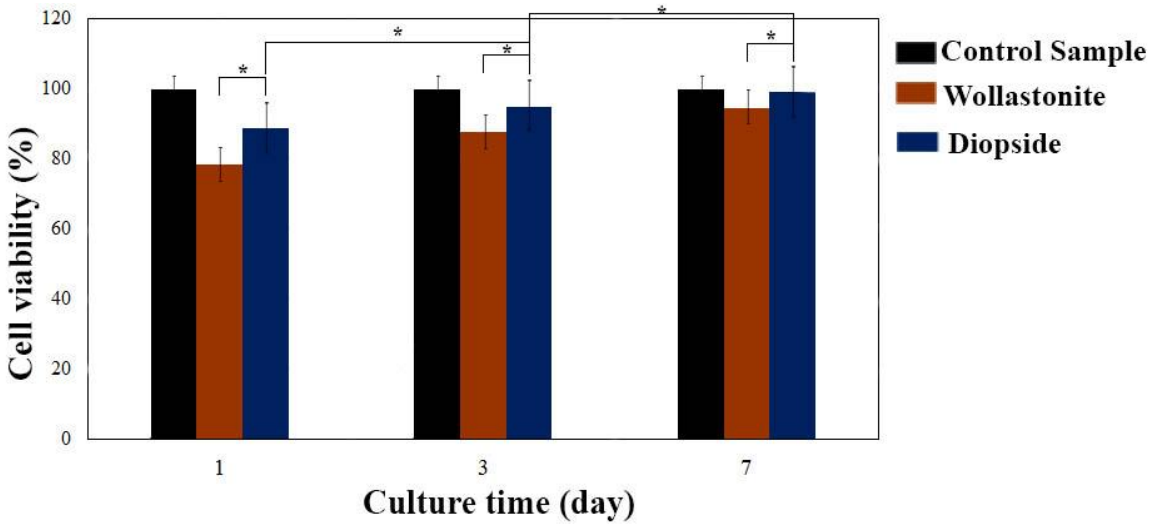

Fig. 9. Results of cell viability related to wollastonite and diopside nano-bioceramics

Figs. 10a,b present the optical microscope images of the culture medium, including MG-63 osteoblast cells and diopside nano-bioceramic after alizarin red staining for 7 and 14 days. After 7 days, red veins (Fig. 10a) are observed. Fig. 10b presents an optical microscope image after 14 days of alizarin red staining. The majority of areas in the image are red, showing that calcium activity in the diopside increased after 14 days. In fact, diopside increased the secretion of calcium in the cells causing the Ca^{2+} ions to be released from the cell membrane. It persuaded the MG-63 osteoblast cells to secrete calcium, indicating the high bioactivity of diopside. Similarly, Figs. 10c,d present the optical microscope images of the culture medium, including MG-63 osteoblast cells and wollastonite nano-bioceramic after 7 and 14 days of alizarin red staining. After 14 days of alizarin red staining, calcium activity increased in wollastonite. In fact, wollastonite caused calcium secretion in the cells to increase, suggesting the release of the Ca^{2+} ion from the cell membrane. Accordingly, wollastonite persuaded the MG-63

osteoblast cells to secrete calcium, showing that wollastonite is bioactive nano-bioceramic.

Fig. 10e presents the optical absorption (nm) according to the culture time (day) diagram after alizarin red staining related to diopside and wollastonite. According to the results, there was a meaningful difference ($p < 0.05$) for wollastonite and diopside at 7 and 14 days.

Fig. 10e proves that increasing calcium activity related to two compounds after 14 days of alizarin red staining is much better and more outstanding than increasing calcium activity after 7 days of alizarin red staining related to two compounds. It can be expressed that alizarin red staining showed that MG-63 osteoblast cells in contact with diopside nano-bioceramic and culture medium were stimulated so that Ca^{2+} was released from the cell membrane, and therefore, more red veins and high absorption related to calcium activity. Moreover, with regard to the results of alizarin red staining between diopside and wollastonite, it is concluded that diopside has offered more acceptable and excellent performance compared to wollastonite. In fact, the bioactivity of diopside was higher than that of wollastonite. Generally, when Mg^{2+} was added to the calcium silicate network, chemical bonds such as ionic and covalent bonds become stronger in $CaO–SiO_2–MgO$ system. In other words, adding Mg^{2+} causes the chemical stability of the calcium-silicate network. The issue is effective in improving the mechanical and biological properties of nano-bioceramics. One of the biological parameters is bioactivity. Therefore, the bioactivity of the diopside is much better in comparison to that of the wollastonite.

(a)

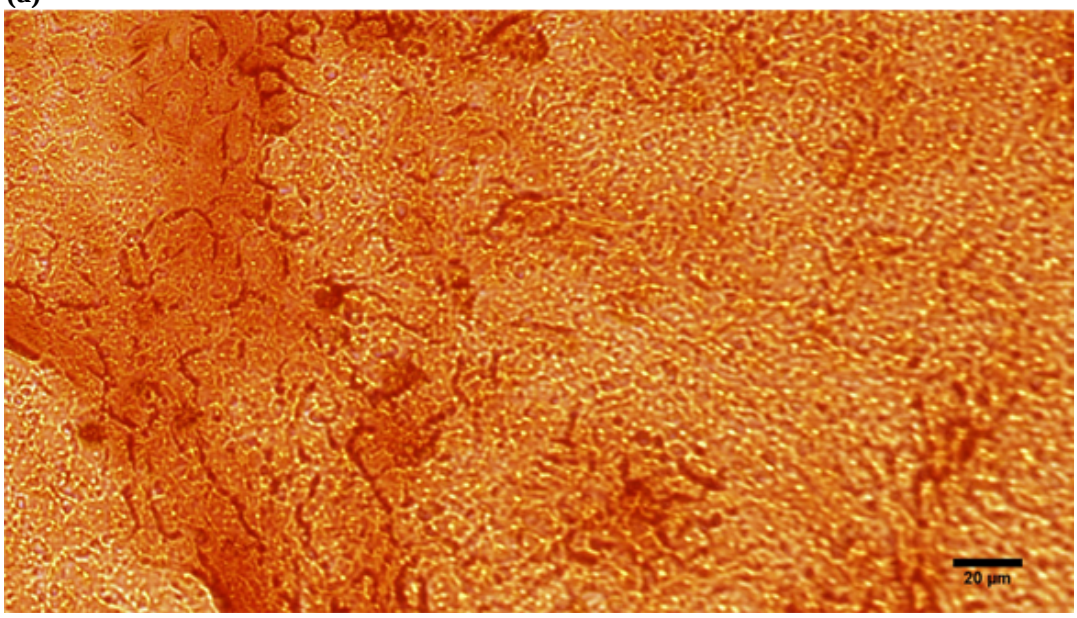

(b)

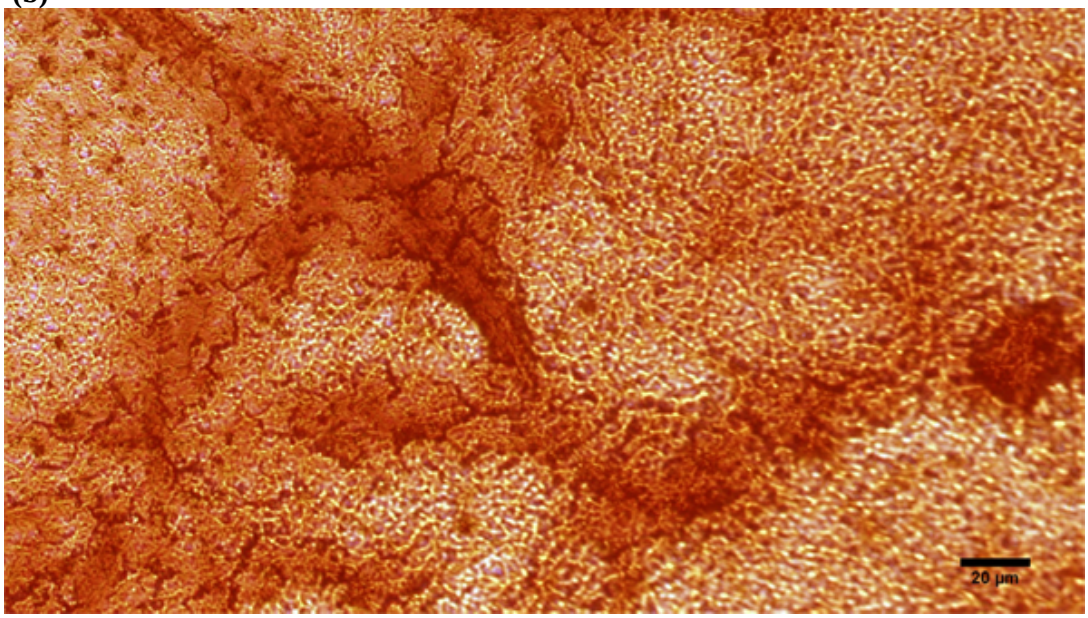

(c)

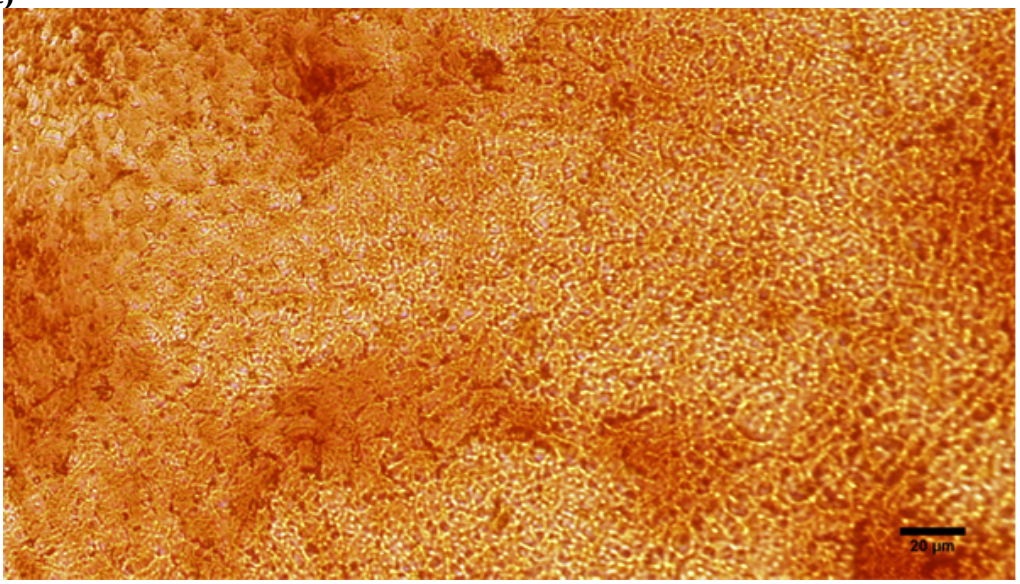

(d)

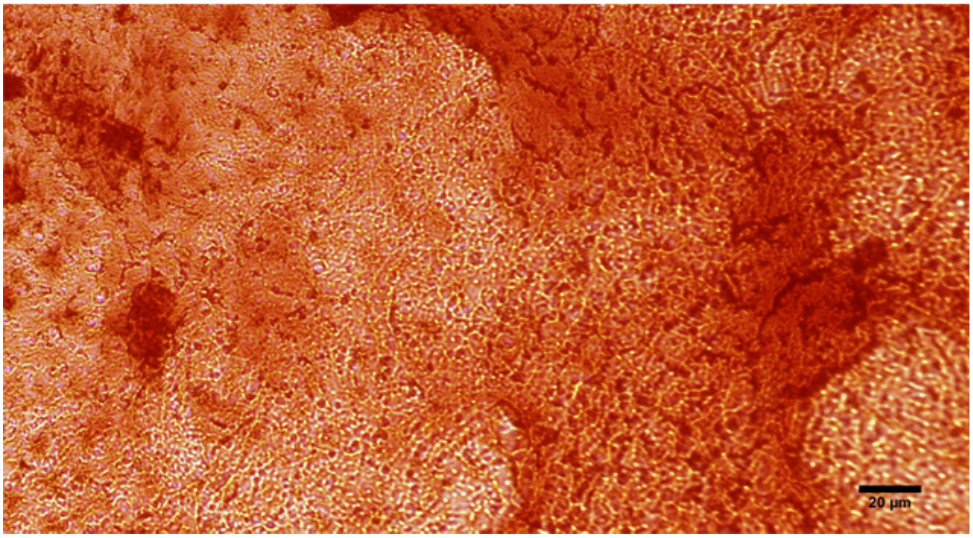

(e)

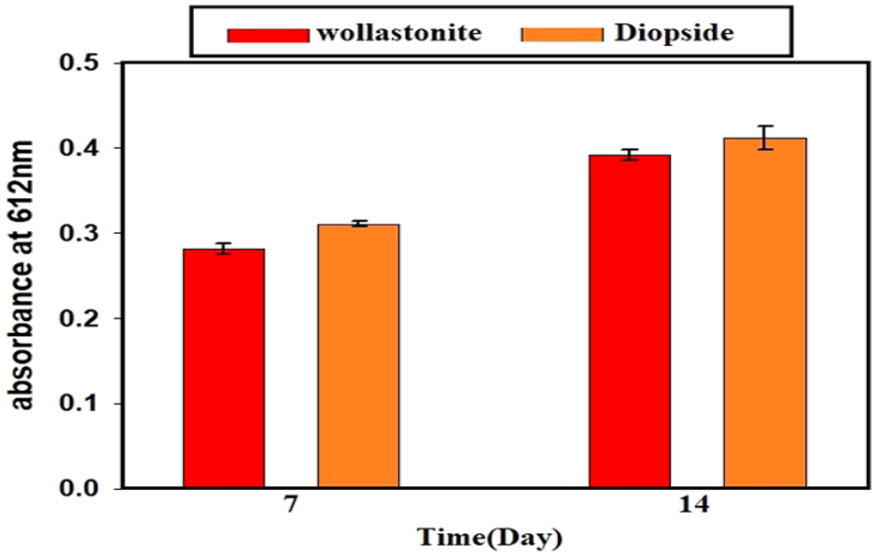

Fig. 10. (a) and (b) Optical microscope images of the culture medium (MG–63 osteoblast cells and diopside) obtained by alizarin red staining, (c) and (d) Optical microscope images of the culture medium (MG–63 osteoblast cells and wollastonite) obtained by alizarin red staining, and (e) diagram of optical absorption according to the culture time after alizarin red staining relevant to diopside and wollastonite compounds

Fig. 11 presents the diagram of the ALP rate according to culture time of diopside and wollastonite after culturing for 3, 7, and 14 days. According to the results, there was a meaningful difference ($p<0.05$) for wollastonite and diopside at 3, 7, and 14 days. As can be observed, high alkaline phosphatase enzyme activity increased in the presence of diopside and wollastonite after 14 days of culture. Moreover, the enzyme possesses better activity in the presence of diopside compared to its activity in the presence of wollastonite. The obtained results showed that the secretion of the alkaline phosphatase enzyme was in contact with diopside and wollastonite compounds from inside the osteoblast cells, causing the formation and restoration of the bone tissue to be accelerated. Diopside had high cell responses compared to wollastonite. This can refer to the incorporation of Mg^{2+} into the calcium-silicate network and, consequently, stability of the network and the enhancement of the cell responses. With respect to cell responses of diopside and wollastonite, it can be concluded that they can serve as potential candidates to apply in bone tissue engineering.

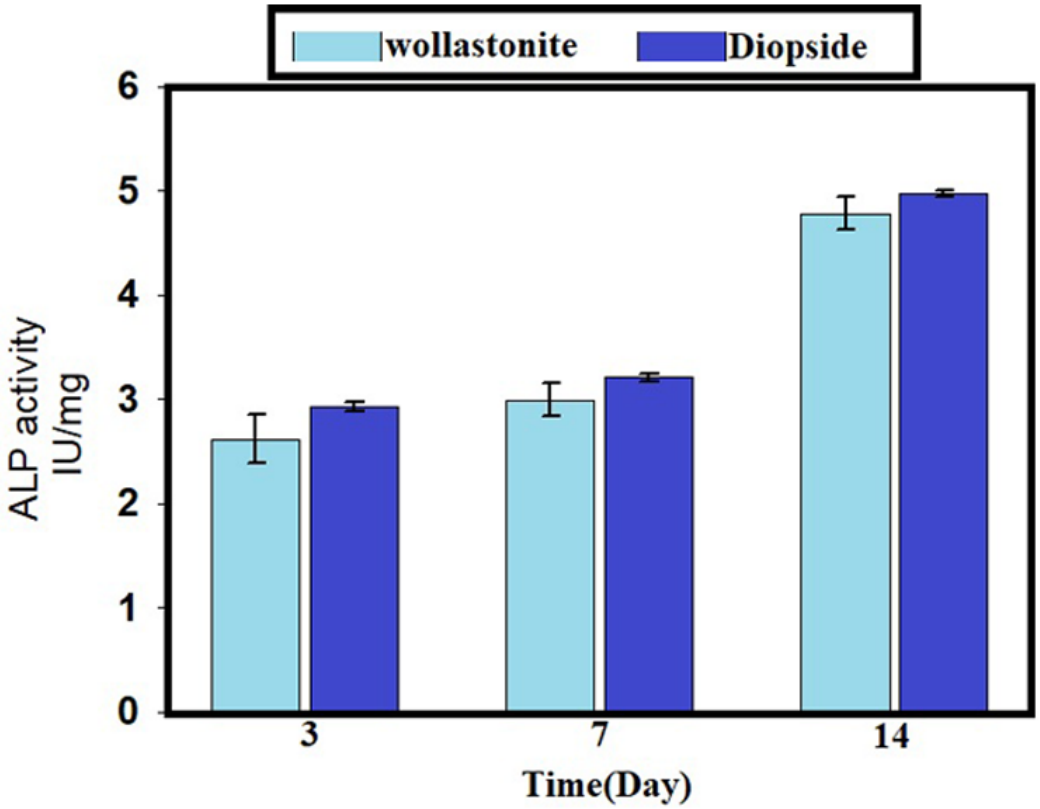

Fig. 11. Diagram of ALP rate–culture time after culturing for 3, 7 and 14 days related to diopside and wollastonite compounds

4. Conclusions

Synthesis and characterization of diopside and wollastonite nano-bioceramics were successfully performed via mechano-chemical and calcination processes. The phase analyses showed that the diopside and wollastonite phases were developed in the $CaO–SiO_2–MgO$ ternary and $CaO–SiO_2$ binary systems after milling for 20 h and calcination at 1200. The TEM images proved that diopside and wollastonite possessed nanostructured with a mean size of about 80 nm due to mechano-chemical and calcination processes. The results related to bio-mineralization and cell responses verified appropriate tissue biomineralization of wollastonite and diopside using the apatite-like layer on the surface of nano-bioceramics. Cell responses of wollastonite and diopside resulted in non-cytotoxicity by the MG-63 osteoblast cells, which confirmed their viability and cell proliferation. Alizarin red staining related to diopside and wollastonite proved high bioactivity and tissue bio-mineralization. The enhancement of the ALP enzyme related to diopside and wollastonite occurred in contact with the MG-63 osteoblast cells. With regard to the existence of Mg^{2+} in the calcium-silicate network and the stability network, diopside exhibited high biological and cell responses compared to wollastonite. Finally, wollastonite and diopside can be suggested as bioactive and biocompatible nano-bioceramics for bone tissue engineering.

References

[1] A. Borger, P. Supancic, R. Danzer, “The ball on three balls test for strength testing of brittle discs:

stress distribution in the disc", Ceram. Eur. Soc. J., Vol. 22, 2002, pp. 1425-1436.
[2] R. Damani, R. Gstrein, R. Danzer, "Critical notch – root radius effect in SENB – S fracture toughness testing", Eur. Ceram. Soc. J., Vol. 16, 1996, pp. 695-702.
[3] P.N. De Aza, Z.B. Luklinska, A. Martinez, M.R. Anseau, F. Guitian. S. De Aza, "Morphological and structural study of pseudowollastonite implants in bone", Microsc. J., Vol. 197, 2000, pp. 60-67.
[4] S.V. Dorozhkin, "Bioceramics of calcium orthophosphates", Biomat. J., Vol. 31, 2010, pp. 1465-1485.
[5] Q. Fu, E. Saiz, M.N. Rahaman, A.P. Tomsia, "Bioactive glass scaffolds for bone tissue engineering: state of the art and future perspectives", Mater. Sci. Eng. C J., Vol. 31, 2011, pp. 1245-1256.
[6] Z. Gou, J. Chang, "Synthesis and in vitro bioactivity of dicalcium silicate powders", Eur. Ceram. Soc. J., Vol. 24, 2004, pp. 93-99.
[7] C. Wu, Y. Ramaswamy, H. Zreiqat, "Porous diopside ($CaMgSi_2O_6$) scaffold: A promising bioactive material for bone tissue engineering", Acta. Biomat. J., Vol. 6, 2010, pp. 2237- 3345.
[8] N. Aza, B. Zofia, M. Anseau, "Bioactivity of diopside ceramic in human", Biomed. Mater. Res. Part B.: Appl. Biomater. J., Vol. 73, 2005, pp. 54-60.
[9] S. Sadeghzade, R. Emadi, S. Labbaf, "Hardystonite-diopside nanocomposite scaffolds for bone tissue engineering applications", J. Mat. Chem. and Phy., Vol. 202, 2017, pp. 95-103.
[10] C. Wu, J. Chang, "A review bioactive silicate ceramics", J. of Biomed. Mat., Vol.8, 2013. pp.1-12.
[11] A. Najafinezhad, M. Abdellahi, H. Ghayour, A. Soheily, A. Chami, A. Khandan, "A comparative study on the synthesis mechanism, bioactivity and mechanical properties of three silicate bioceramics", J. Mat. Sci. Eng. C, Vol.72,2017, pp.259-267.
[12] S. Thomas, P. Balakrishnan, M.S. Sreekala,"Fundamental Biomaterials Ceramics", Woodhead Publishing Series in Biomaterials, 2018.
[13] C. Wu, J. Chang, "Degaradation bioactivity, and cytocompatibility of diopside, akermanite, and bredigite ceramics", Biomed. Mat. Res. Part B: Appl. Biomat. J., Vol.83, 2007, pp. 60-153.
[14] C. Wu, J. Chang, J. Wang, S. Ni, W. Zhai, "Preparation and characteristics of a calcium magnesium silicate (bredigite) bioactive ceramic", Biomat. J., Vol. 26, 2005, pp. 2925-2931.
[15] J.F. Shackelford, R.H.H. Doremus, Handbook ceramic and materials structure, properties and processing, Springer, 2008.
[16] L.H. Long, L.D. Chen, J. Chang, "Low temperature fabrication and characterizaition of β–$CaSiO_3$ ceramics", Ceram. Int. J., Vol. 32, 2006, pp. 457-460.
[17] P. Palmero, "Structural ceramic nanocomposites, a review of properties and powders synthesis methods", J. Nanomat., Vol.5, 2015 pp.656-696.
[18] F. Tavangarian, R. Emadi, "Mechanical activation assisted synthesis of pure nanocrystalline forsterite powder", J. Alloy and Compounds., Vol.485, 2009, pp.648-652.
[19] H. Ghomi, R. Emadi, S. Haghjooyeh Javamard, "Preparation of nanostructure bioactive diopside scaffolds for bone tissue engineering by two near net shape manufacturing techniques", Mat. Lett. J., Vol. 167, 2016, pp. 157-160.
[20] A. Monshi, M. Foroughi, M. Monshi, "Modifid Scherrer Equation to Estimate More Accurately Nano – Crystallite Size Using XRD", Nano. Sci. and Eng. J., Vol. 2, 2012, pp. 154-160.
[21] T. Kokubo, H.Takadama, "How useful is SBF in predicting in vivo bone bioactivity?", Biomat. J., Vol. 27, 2006, pp. 2907-2915.
[22] L. Lu, M.O. Lai, Mechanical Alloying, Kluwer Academic Publisher, Boston, 1998.
[23] G.K. Williamson, W.H. Hall, "X – ray line broadening from filed aluminum and wolfram", Acta. Metall. J., Vol. 1, 1953, pp. 22-31.
[24] C. Wu, J. Chang, "A review bioactive silicate ceramics", Biomed. Mat. J., Vol.8, 2013, pp.1-12.
[25] K. Khoshroo, T.S. Jafarzadeh, F. Moztarzadeh, M. Tahriri, H. Jazayeri, L. Tayebi, "Development of 3D PCL microsphere/TiO_2 nanotube composite scaffolds for bone tissue engineering", Mat. Sci. and Eng. C J., Vol. 70, 2017, pp.586-598

JMATPRO	Journal of Advanced Materials and Processing 10 (1): 57-65, Winter 2022 http://jmatpro.iaun.iau.ir 20.1001.1.2322388.2022.10.1.5.8

Research Paper

Effect of Nano-MgO Additive on Compressive Strength of Concrete Fabricated by Different Processing Methods

Eisa Mahmoudsaleh[1], Ali Heidari[1&2*], Farshid Fathi[1], Seyed Ali Hassanzadeh-Tabrizi[3]

1. Department of Civil Engineering, Najafabad Branch, Islamic Azad University, Najafabad, Iran.

2. Department of Civil Engineering, University of Shahrekord, Shahrekord, Iran.

3. Advanced Materials Research Center, Department of Materials Engineering, Najafabad Branch, Islamic Azad University, Najafabad, Iran.

ARTICLE INFO

Article history:

Received 25 October 2021
Accepted 23 December 2021
Available online 1 January 2022

Keywords:
Nanomaterials
MgO
Concrete
Mechanical properties

ABSTRACT

The effects of adding different nano-MgO dosages (0, 1, 2, 3, and 4 wt.% with respect to cement) on microstructural, compressive strength, and phase evaluation of concrete were investigated. Two different post-treatment conditions with water and CO_2 gas were used to study the processing method on the samples. The specimens were characterized via SEM and XRD analysis. The mechanical properties of the samples were also investigated. The results showed that compressive strength significantly improved after the addition of magnesium oxide nanoparticles. However, this improvement was more remarkable in the case of post-treatment with CO_2 compared to the samples fabricated with water. SEM results showed that the samples treated under CO_2 gas had irregular and needle-like morphology. The samples prepared by normal processing had $CaCO_3$ and SiO_2 phases, whereas the ones fabricated under CO_2 gas contained $CaCO_3$, SiO_2, and $Ca(OH)_2$. With the addition of nano-MgO, the density of concrete decreases in the samples post-treated with water, whereas it increases for the samples post-treatment with CO_2 gas. Adding 4 wt.% nano-MgO to concrete and further post-treatment with CO_2 for 45 days could increase the mechanical properties from ~ 23 MPa to ~ 55 MPa.

Citation: Mahmoudsaleh, E.; Heidari, A.; Fathi, F.; Hassanzadeh-Tabrizi, S.A. (2022) Effect of Nano-MgO Additive on Compressive Strength of Concrete Fabricated by Different Processing Methods, Journal of Advanced Materials and Processing, 10 (1), 57-65. Dor: 20.1001.1.2322388.2022.10.1.5.8

* **Corresponding Author**
E-Mail Address: aliheydarisku6@gmail.com

1. Introduction

Nano dimension materials like nanoparticles, nanobelts, nanosheets, etc., have attracted much attention in the last 100 years [1]. In this dimension, the mechanical and physical properties of materials could be changed. This phenomenon has been extensively used in recent years in many industries like textile, chemical, plastic, cosmetics, and so on [2–4]. One of the essential subjects is to use of nanomaterials for improving the raw materials in the construction industry [5,6].

Portland cement may be a widely used building material in the world. Because of chemical, drying, and autogenous shrinkage caused by temperature stress, this material cracks quickly [7]. These cracks compromise building safety, diminish service life, and result in significant economic and societal losses. In addition, the formed cracks allow acidic chemicals to enter the concrete, causing carbonation, corrosion, and unwanted reactions. It could also destroy the steel in the reinforced concrete [8]. These events reduce the strengths of the structure [9]. Nanomaterials could be added to the concrete to improve the mechanical properties and inhibit these drawbacks. For example, some researchers added carbon nanotube [10,11] to concrete and showed that the nanomaterials ameliorate the properties of the structure. Promising results have also been reported with the addition of graphene [12–14]. Magnesium oxide (MgO) is a fascinating basic oxide ceramic with numerous applications [15]. This oxide ceramic can be used as an absorbent of toxic chemicals, refractories, catalyst support, optic instrument, etc. [16–20]. Volume expansion happens in this material when it reacts with water due to the formation of $Mg(OH)_2$. By adding MgO to concrete, this hydration and expansion could compensate for the contraction of concrete and may reduce the chance of crack formation [21,22].

This study aimed to add nano-MgO to concrete processed by two different methods (post-treated with water and carbon dioxide) to investigate its effects on the mechanical properties, phase evaluation, and microstructure. Although the MgO addition to concrete has been studied before, in the present work, the effect of nano-MgO was investigated based on the post-treatment processing of concrete which is a new approach.

Table 1. Chemical composition of Portland cement

Chemical Composition	CaO	SiO_2	Al_2O_3	Fe_2O_3	MgO	SO_3	K_2O	Na_2O	L.O.I
Weight percent	53.27	21.89	5.3	3.34	6.45	3.67	0.98	0.18	3.21

Table 2. The composition, code name, and applied curing condition of the samples

Curing Condition	Sample Code	Composition weight (g)					
		Cement	Stone Powder	Grit	Sand	Water	Nano-MgO
Water	0% MgO-N	333	167	625	708	120	0
	1% MgO-N	314.7	167	625	708	120	18.3
	2% MgO-N	296.4	167	625	708	120	36.6
	3% MgO-N	287	167	625	708	120	55
	4% MgO-N	260	167	625	708	120	73.32
CO_2	0% MgO-C	333	167	625	708	120	0
	1% MgO-C	314.7	167	625	708	120	18.3
	2% MgO-C	296.4	167	625	708	120	36.6
	3% MgO-C	287	167	625	708	120	55
	4% MgO-C	260	167	625	708	120	73.32

2. Experimental procedure

2.1. Materials and Methods

In the present study, Portland cement, Stone Powder, Grit, Sand, and water with the chemical composition shown in Table 1 were used. Nano-MgO was purchased from US-nano. Based on the compositions shown in Table 2, the raw materials were mixed. The MgO-mixed cement was made by adding different amounts of nano magnesium oxide to the Portland cement and other compounds mixture. The raw materials were mixed based on the ASTM C 305 [23]. The method includes the dispersion of nano-MgO in water by ultrasonic for 15 min in order to deagglomerate MgO nanoparticles. All the samples were produced with a water-to-cement ratio of 0.45 and produced in a laboratory mixer. For the construction of blocks, H_2O was added to the mixed samples for 3 min under stirring. The fresh pastes were cast in steel molds. The samples were covered with a polyethylene sheet to prevent water evaporation. After 24 h, the samples were demolded without slump. Then, the samples were subjected to CO_2 gas or immersed in water for 7, 30, and 45 days to investigate the effect of curing on the samples. The purity of CO_2 gas was 98%. Four samples were produced for each mixture and an average value of measurements with error bars was reported. The name of the samples was shown in Table 2.

2.2. Characterizations

The phase evaluation of the samples was analyzed by X-ray diffraction (Philips PW3040 diffractometer) with copper radiation. SEM images were taken with a VEGA/TESCAN Mira 3-XMU microscope. The compressive strength of the fabricated specimens was measured by uniaxial loading of 55 kN/min using a Toni Technik Baustoffprüfsysteme machine. The density (ρ) of samples was measured according to their size and weights based on equation 1.

$$\rho = \frac{Mass\ of\ sample\ after\ post-tratment}{Volume\ of\ sample\ after\ post-tratment} \quad \text{(Eq. 1)}$$

3. Results and discussion

Fig. 1 shows the XRD result and SEM image of the nano-MgO used for addition to the concrete. According to the XRD pattern of the sample (Fig. 1a), all of the peaks are related to the conventional cubic MgO reflections (JCPDS 45–0946). The (111), (200), (220), (311), and (222) MgO crystal planes correspond to the diffraction peaks at 36.6°, 42.5°, 61.8°, 74.0°, and 78.3°. SEM micrograph (Fig. 1b) shows that the powders have homogeneous spherical particles with an average particle size of about 30 nm. The nanopowders contain some aggregates and agglomerates. The high surface energy of the nanopowders causes the production of these agglomerates. As a result, nanoparticles tend to clump together in order to reduce their surface energy [24–27].

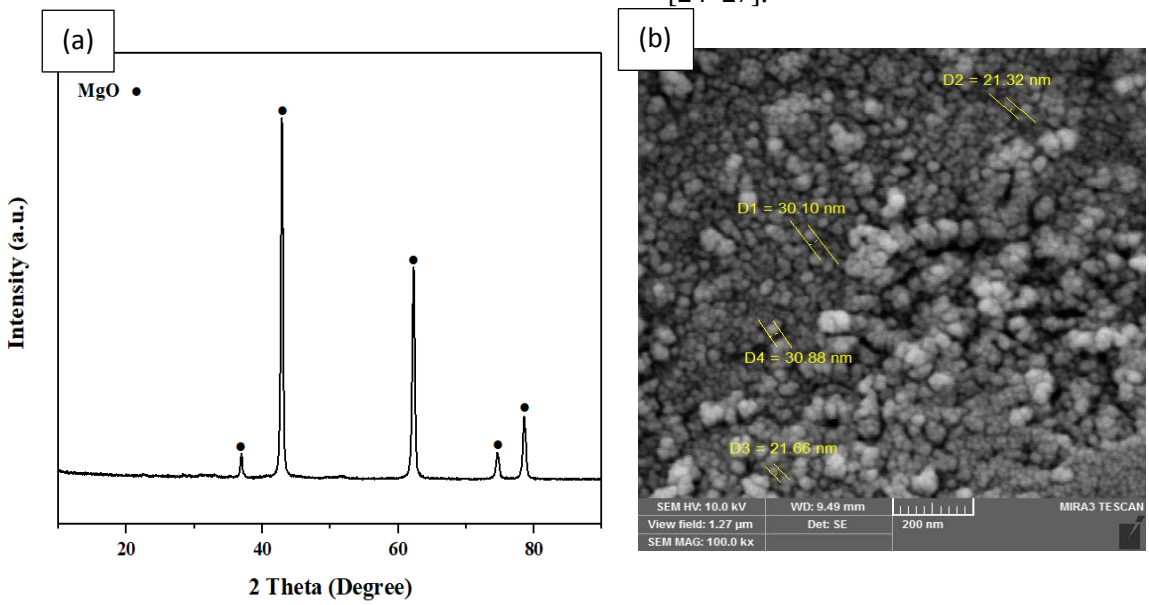

Fig. 1. (a) XRD pattern and (b) SEM image of the MgO.

Fig. 2 displays the XRD patterns of samples with different amounts of MgO post-treated with water and CO_2 gas for 45 days. As can be seen, in the sample post-treated with water, $CaCO_3$, SiO_2, and $Ca(OH)_2$ phases are observed. The formation of calcium hydroxide is due to a reaction between calcium oxide and water during post-treatment according to equation 2 [28].

$$CaO + H_2O \rightarrow Ca(OH)_2$$
$$\Delta H = -104.2\ kJ\ mol^{-1} \quad \text{(Eq. 2)}$$

Due to variations in the specific volumes of $Ca(OH)_2$ (0.45 cm^3/g) and CaO (0.29 cm^3/g) [29], the sample expands during the reaction. The nano-MgO may also react with water and form magnesium hydroxide, which accompanies expansion. Due to the intrinsic contraction of concrete during reaction and

drying, cracks form, which is harmful and reduces the mechanical properties. The expansion of formed hydrated phases after post-treatment compensates for the contraction of the concrete and reduces the chance of crack creation. The peaks related to magnesium oxide could not be detected in the samples, which may be due to the low amount of MgO in the samples. The samples with CO_2 post-treatment show $CaCO_3$ and SiO_2 components. Processing with carbon dioxide prevented the formation of hydrated phases. In this condition, the carbonate phases of calcium and magnesium may be formed.

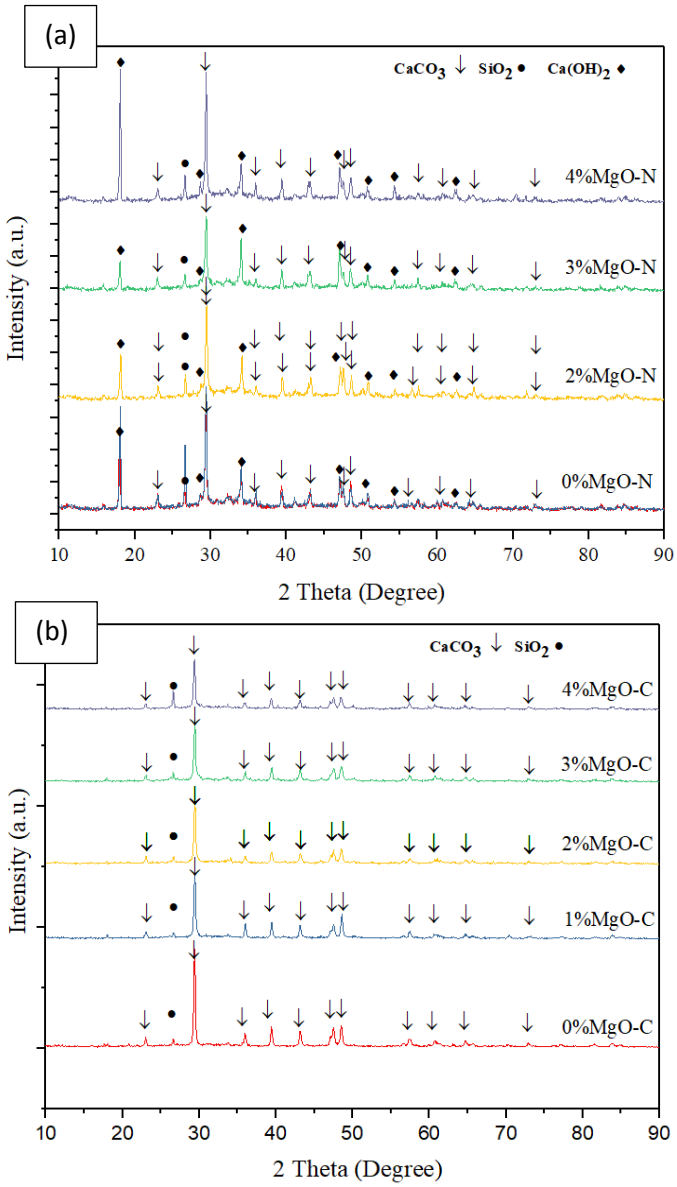

Fig. 2. XRD patterns of the fabricated samples with different nano MgO post-treated with (a) water and (b) CO_2.

density of the samples with different amounts of MgO post-treated with water and CO_2 is shown in Fig. 3. As can be seen, nano-MgO has a different effect on the density of the samples. In the samples post-treated with water, by increasing MgO content, the density of concrete decreases. This reduction is due to the hydration of magnesium oxide (ρ=~3.58 g cm^{-3}) and the formation of $Mg(OH)_2$ (ρ=~2.34 g cm^{-3}). For the samples post-treated with CO_2, the density of samples increases by adding nano magnesium oxide. This increase may be accomplished by the creation of magnesium carbonate (ρ=~2.96 g cm^{-3}) The

from magnesium hydroxide (ρ=~2.34 g cm^{-3}) according to equation 3 [30].

$$Mg\ (OH)_2 + CO_2 \rightarrow MgCO_3 + H_2O$$

$\Delta H = -30.2$ kJ mol^{-1} (Eq. 3)

In addition to $MgCO_3$, the formation of the hydrated phase of magnesium carbonate has also been reported. In other words, the reaction between water and $MgCO_3$ can create nesquehonite ($MgCO_3.3H_2O$), dypingite ($Mg_5(CO_3)_4(OH)_2.5H_2O$), and artinite ($Mg_2(OH)_2CO_3.3H_2O$) [31,32]. Among these hydrated phases of magnesium carbonate,

nesquehonite is more common in the CO_2 post-treatment [30]. It was reported that the formation of these hydrated phases could create a densified structure with high binding power, therefore improving the mechanical characteristics of the construction [33,34]. However, the formation of the prominent phase in the final products strongly depends on many factors such as temperature, CO_2 pressure, the humidity of CO_2 gas, etc. [35–38].

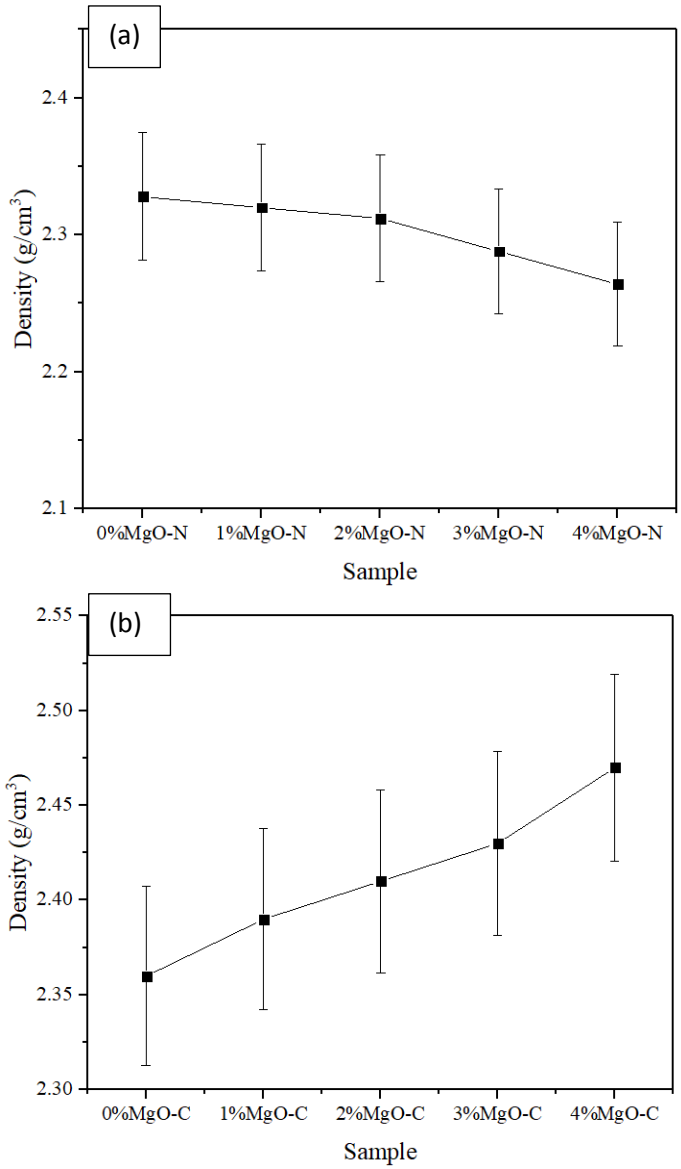

Fig. 3. The density of the samples with different amounts of MgO post-treated with (a) water and (b) CO_2.

Fig. 4 shows SEM micrographs of the samples with different amounts of MgO post-treated for 45 days with water and CO_2. As can be seen, the samples post-treated with water have particles with irregular and spherical morphologies, whereas the samples post-treated with CO_2 exhibit irregular and needle-like morphologies. The needle-like shape of particles in the carbon dioxide post-treated samples may be due to the formation of carbonate phases. There are some cracks and pores in the pure concrete, which could be attributed to the contraction of concrete during the drying. By increasing the nano magnesium oxide in the concreate, the number of cracks and pores is reduced. This reduction of the defects in the nano-MgO added samples is due to the volume changes during the formation of hydrated and carbonated phases during the post-treatment process. In other words, the expansion due to the formed phases reduces the contraction effect of the concrete [39,40].

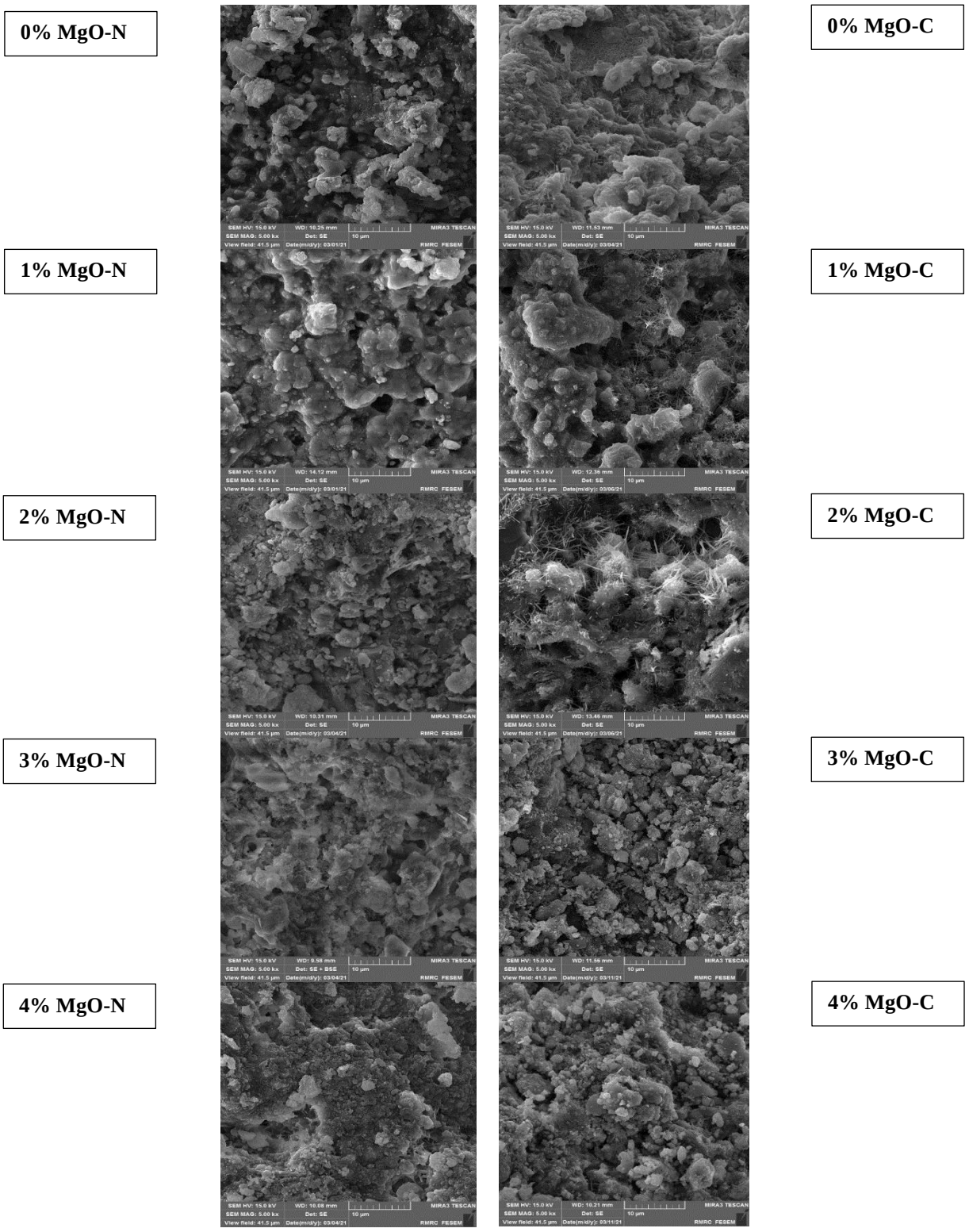

Fig. 4. SEM micrographs of the samples with different amounts of MgO post-treated with (a) water and (b) CO_2.

Fig. 5 represents the compressive strength of the samples with different amounts of MgO and post-treated with water and CO_2 on different days. It is clear that in all samples, with the increase of post-treatment days from 7 days to 45 days, the compressive strengths of the samples improve. This improvement could be attributed to the formation of hydrated and carbonated phases during post-treatment, which results in the reduction of the formed stress in the concrete. In addition, the addition of MgO leads to an improvement in the mechanical properties of the samples. The SEM results showed that adding MgO reduces the number of defects like cracks and pores, which may explain why nano-MgO ameliorates the compressive strength. In addition, it was reported that the improvement in the mechanical properties of samples by adding MgO could be due to its high activity and the seeding effect of these nanoparticles

[41]. It seems that post-treatment with CO_2 has a better effect on improving compressive strength. For instance, the 4% MgO-C sample reached a compressive strength of about 55 MPa, but the 4% MgO-N sample had a compressive strength of about 51 MPa after 45 days post-treatment. It is noteworthy that the uniform distribution of nano-size MgO in the concrete matrix is critical. It is because, during the hydration and carbonation of magnesium oxide, uniform stress would create in the microstructure, which results in the filling of pores and cracks. Therefore, it may cause better improvement in the mechanical properties of final products. It is noteworthy that high amounts of MgO or large-scale MgO may have an adverse effect on the mechanical properties of samples. For example, It was reported that high amounts of large-size magnesium oxide in the cement could cause extreme expansion, which results in the formation of cracks and reduction of mechanical properties. In the nanosized scale, the formation of these local stressed is reduced, which may improve these destructing expansion effects [42,43].

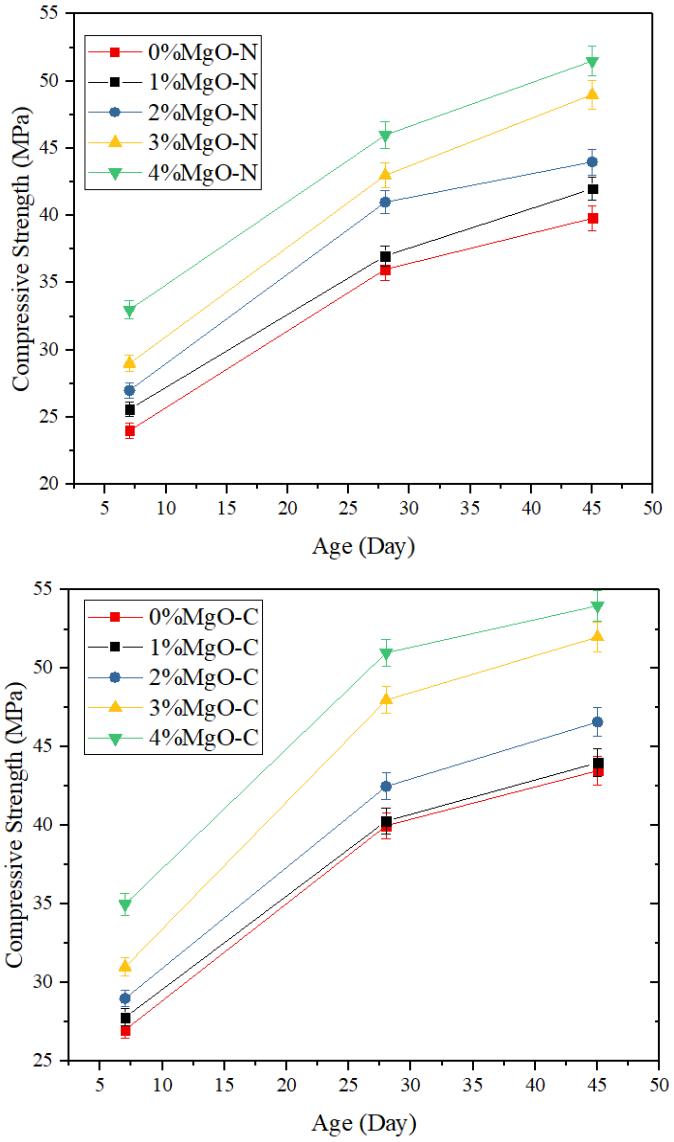

Fig. 5. Compressive strength of the samples with different amounts of MgO post-treated with (a) water and (b) CO_2.

4. Conclusions

The effect of two different post-treatment with water and CO_2 on the mechanical properties of the MgO-added concrete was investigated. The samples were studied via X-ray diffraction and Scanning electron microscopy. The XRD results showed that $CaCO_3$, SiO_2, and $Ca(OH)_2$ phases are formed in the post-treated samples with H_2O, whereas the hydrated phases are not observed in the post-treated specimens with CO_2. Compressive strength improved by adding nano-MgO and increasing the time of post-treatment. The samples post-treated in CO_2 had irregular and needle-like morphologies. The density of the samples post-treated with water decreases with adding nano-MgO, whereas the density of the ones post-treated with carbon dioxide increases by increasing magnesium oxide. Post-treatment of concrete with

CO_2 had a better effect on the ameliorating of mechanical properties than processing with water.

References

[1] N. Baig, I. Kammakakam, W. Falath, Nanomaterials: A review of synthesis methods, properties, recent progress, and challenges, Mater. Adv. 2 (2021) 1821–1871.
[2] G. Bhattacharya, S.J. Fishlock, J.A. McLaughlin, S.S. Roy, Metal-oxide nanomaterials recycled from E-waste and metal industries: A concise review of applications in energy storage, catalysis, and sensing, Int. J. Energy Res. 45 (2021) 8091–8102.
[3] M.A. Subhan, K.P. Choudhury, N. Neogi, Advances with Molecular Nanomaterials in Industrial Manufacturing Applications, Nanomanufacturing. 1 (2021) 75–97.
[4] C. Thongchom, N. Refahati, P. Roodgar Saffari, P. Roudgar Saffari, M.N. Niyaraki, S. Sirimontree, S. Keawsawasvong, An experimental study on the effect of nanomaterials and fibers on the mechanical properties of polymer composites, Buildings. 12 (2021) 7.
[5] M. Janczarek, Ł. Klapiszewski, P. Jędrzejczak, I. Klapiszewska, A. Ślosarczyk, T. Jesionowski, Progress of functionalized TiO_2-based nanomaterials in the construction industry: A comprehensive review, Chem. Eng. J. 430 (2022) 132062.
[6] A.A. Firoozi, M. Naji, M. Dithinde, A.A. Firoozi, A review: influence of potential nanomaterials for civil engineering projects, Iran. J. Sci. Technol. Trans. Civ. Eng. 45 (2021) 2057–2068.
[7] E. Enríquez, M. Torres-Carrasco, M.J. Cabrera, D. Muñoz, J.F. Fernández, Towards more sustainable building based on modified Portland cements through partial substitution by engineered feldspars, Constr. Build. Mater. 269 (2021) 121334.
[8] L. Wang, M. Jin, Y. Wu, Y. Zhou, S. Tang, Hydration, shrinkage, pore structure and fractal dimension of silica fume modified low heat Portland cement-based materials, Constr. Build. Mater. 272 (2021) 121952.
[9] Z. Li, B. Delsaute, T. Lu, A. Kostiuchenko, S. Staquet, G. Ye, A comparative study on the mechanical properties, autogenous shrinkage and cracking proneness of alkali-activated concrete and ordinary Portland cement concrete, Constr. Build. Mater. 292 (2021) 123418.
[10] Y. Liu, T. Shi, Y. Zhao, Y. Gu, Z. Zhao, J. Chen, B. Zheng, S. Shi, Autogenous shrinkage and crack resistance of carbon nanotubes reinforced cement-based materials, Int. J. Concr. Struct. Mater. 14 (2020) 1–10.
[11] T. Shi, Z. Li, J. Guo, H. Gong, C. Gu, Research progress on CNTs/CNFs-modified cement-based composites–a review, Constr. Build. Mater. 202 (2019) 290–307.
[12] Y. Zhao, Y. Liu, T. Shi, Y. Gu, B. Zheng, K. Zhang, J. Xu, Y. Fu, S. Shi, Study of mechanical properties and early-stage deformation properties of graphene-modified cement-based materials, Constr. Build. Mater. 257 (2020) 119498.
[13] C.J. Liu, X.C. Hunag, Y.-Y. Wu, X.W. Deng, Z.L. Zheng, B. Yang, Studies on mechanical properties and durability of steel fiber reinforced concrete incorporating graphene oxide, Cem. Concr. Compos. (2022) 104508.
[14] P. Reddy, D.R. Prasad, Investigation on the impact of graphene oxide on microstructure and mechanical behaviour of concrete, J. Build. Pathol. Rehabil. 7 (2022) 1–10.
[15] R. Pournajaf, S.A. Hassanzadeh-Tabrizi, R. Ebrahimi-Kahrizsangi, A. Alhaji, A.A. Nourbakhsh, Optimization of magnesia sintering parameters fabricated by spark plasma sintering method for infrared transparency, Mater. Res. Express. 8 (2021) 65002.
[16] S. Gandhi, P. Abiramipriya, N. Pooja, J.J.L. Jeyakumari, A.Y. Arasi, V. Dhanalakshmi, M.R.G. Nair, R. Anbarasan, Synthesis and characterizations of nano sized MgO and its nano composite with poly (vinyl alcohol), J. Non. Cryst. Solids. 357 (2011) 181–185.
[17] R. Pournajaf, S.A. Hassanzadeh-Tabrizi, R. Ebrahimi-Kahrizsangi, A. Alhaji, A.A. Nourbakhsh, Polycrystalline infrared-transparent MgO fabricated by spark plasma sintering, Ceram. Int. 45 (2019) 18943–18950.
[18] X. Xu, T. Zhu, Y. Li, Y. Dai, M. Nath, Y. Ye, N. Hu, Y. Li, X. Wang, Effect of particle grading on fracture behavior and thermal shock resistance of MgO-C refractories, J. Eur. Ceram. Soc. 42 (2022) 672–681.
[19] A.S. Farooqi, M. Yusuf, N.A.M. Zabidi, R. Saidur, M.U. Shahid, B.V. Ayodele, B. Abdullah, Hydrogen-rich syngas production from bi-reforming of greenhouse gases over zirconia modified Ni/MgO catalyst, Int. J. Energy Res. 46 (2022) 2529–2545.
[20] H.L. Senevirathna, P.V.T. Weerasinghe, X. Li, M.-Y. Tan, S.-S. Kim, P. Wu, Counter-Intuitive Magneto-Water-Wetting Effect to CO2 Adsorption at Room Temperature Using $MgO/Mg(OH)_2$ Nanocomposites, Materials (Basel). 15 (2022) 983.
[21] L. Wang, G. Li, X. Li, F. Guo, S. Tang, X. Lu, A. Hanif, Influence of reactivity and dosage of MgO expansive agent on shrinkage and crack resistance of face slab concrete, Cem. Concr. Compos. 126 (2022) 104333.
[22] L. Wang, X. Song, H. Yang, L. Wang, S. Tang, B. Wu, W. Mao, Pore structural and fractal analysis of the effects of MgO reactivity and dosage on permeability and F–T resistance of concrete, Fractal Fract. 6 (2022) 113.
[23] A. Standard, C305. Standard practice for

mechanical mixing of hydraulic cement pastes and mortars of plastic consistency, Annu. B. ASTM Stand. (2006).
[24] M.A.Y.A. Bakier, K. Suzuki, P. Khajornrungruang, Study on Nanoparticle Agglomeration During Chemical Mechanical Polishing (CMP) Performance, J. Nanofluids. 10 (2021) 420–430.
[25] V.I. Popkov, Y. Albadi, The effect of co-precipitation temperature on the crystallite size and aggregation/agglomeration of $GdFeO_3$ nanoparticles, Наносистемы: Физика, Химия, Математика. 12 (2021) 224–231.
[26] Q. Li, L. Zhang, S. Wei, Y. Zhang, R. Sun, T. Zhou, W. Bu, Q. Yao, Z. Jiang, H. Chen, Weakly agglomerated α-Al2O3 nanopowders prepared by a novel spray precipitation method, Ceram. Int. 44 (2018) 11374–11380.
[27] R. Pournajaf, S.A. Hassanzadeh-Tabrizi, Polyacrylamide synthesis of nanostructured copper aluminate for photocatalytic application, J. Adv. Mater. Process. 5 (2018) 12–19.
[28] Y.A. Criado, M. Alonso, J.C. Abanades, Kinetics of the CaO/Ca (OH) 2 hydration/dehydration reaction for thermochemical energy storage applications, Ind. Eng. Chem. Res. 53 (2014) 12594–12601.
[29] J. Kariya, J. Ryu, Y. Kato, Reaction performance of calcium hydroxide and expanded graphite composites for chemical heat storage applications, ISIJ Int. 55 (2015) 457–463.
[30] L. Wang, L. Chen, J.L. Provis, D.C.W. Tsang, C.S. Poon, Accelerated carbonation of reactive MgO and Portland cement blends under flowing CO_2 gas, Cem. Concr. Compos. 106 (2020) 103489.
[31] R.L. Frost, S. Bahfenne, J. Graham, Raman spectroscopic study of the magnesium-carbonate minerals—artinite and dypingite, J. Raman Spectrosc. An Int. J. Orig. Work All Asp. Raman Spectrosc. Incl. High. Order Process. Also Brillouin Rayleigh Scatt. 40 (2009) 855–860.
[32] A.L. Harrison, V. Mavromatis, E.H. Oelkers, P. Bénézeth, Solubility of the hydrated Mg-carbonates nesquehonite and dypingite from 5 to 35° C: Implications for CO_2 storage and the relative stability of Mg-carbonates, Chem. Geol. 504 (2019) 123–135.
[33] S.A. Walling, J.L. Provis, Magnesia-based cements: a journey of 150 years, and cements for the future?, Chem. Rev. 116 (2016) 4170–4204.
[34] L. Mo, F. Zhang, D.K. Panesar, M. Deng, Development of low-carbon cementitious materials via carbonating Portland cement–fly ash–magnesia blends under various curing scenarios: a comparative study, J. Clean. Prod. 163 (2017) 252–261.
[35] L. Mo, D.K. Panesar, Effects of accelerated carbonation on the microstructure of Portland cement pastes containing reactive MgO, Cem. Concr. Res. 42 (2012) 769–777.
[36] V.D. Pizzol, L.M. Mendes, L. Frezzatti, H. Savastano Jr, G.H.D. Tonoli, Effect of accelerated carbonation on the microstructure and physical properties of hybrid fiber-cement composites, Miner. Eng. 59 (2014) 101–106.
[37] B.J. Zhan, D.X. Xuan, C.S. Poon, C.J. Shi, Effect of curing parameters on CO_2 curing of concrete blocks containing recycled aggregates, Cem. Concr. Compos. 71 (2016) 122–130.
[38] C. Shi, Y. Wu, Studies on some factors affecting CO_2 curing of lightweight concrete products, Resour. Conserv. Recycl. 52 (2008) 1087–1092.
[39] Y. Sun, P. Zhang, W. Guo, J. Bao, C. Qu, Effect of nano-$CaCO_3$ on the mechanical properties and durability of concrete incorporating fly Ash, Adv. Mater. Sci. Eng. 2020 (2020).
[40] S. Ruan, C. Unluer, Influence of mix design on the carbonation, mechanical properties and microstructure of reactive MgO cement-based concrete, Cem. Concr. Compos. 80 (2017) 104–114.
[41] P. Hou, Y. Cai, X. Cheng, X. Zhang, Z. Zhou, Z. Ye, L. Zhang, W. Li, S.P. Shah, Effects of the hydration reactivity of ultrafine magnesium oxide on cement-based materials, Mag. Concr. Res. 69 (2017) 1135–1145.
[42] R. Polat, R. Demirboğa, F. Karagöl, The effect of nano-MgO on the setting time, autogenous shrinkage, microstructure and mechanical properties of high performance cement paste and mortar, Constr. Build. Mater. 156 (2017) 208–218.
[43] Q. Ye, K. Yu, Z. Zhang, Expansion of ordinary Portland cement paste varied with nano-MgO, Constr. Build. Mater. 78 (2015) 189–193.

JMATPRO	Journal of Advanced Materials and Processing 10 (1): 67-76, Winter 2022 http://jmatpro.iaun.iau.ir 20.1001.1.2322388.2022.10.1.6.9

Research Paper

Effect of Fluoride Coating on the Degradation of Mg-Based Alloy Containing Calcium for Biomedical Applications

Abouzar Rezaei-Baravati, Masoud Kasiri-Asgarani*, Hamid Reza Bakhsheshi-Rad†, Mahdi Omidi, Ebrahim Karamian

Advanced Materials Research Center, Department of Materials Engineering, Najafabad Branch, Islamic Azad University, Najafabad, Iran

ARTICLE INFO

Article history:

Received 27 October 2021
Accepted 29 December 2021
Available online 1 January 2022

Keywords:
Magnesium alloy
Corrosion behavior
Fluoride treatment
Surface treatment
Weight loss

ABSTRACT

The effect of hydrofluoric acid (HF) treatment on the corrosion performance of the Mg–Zn–Al–0.5Ca alloy was studied by immersing a specimen in HF solutions for varying lengths of time at room temperature. X-ray diffraction (XRD), scanning electron microscopy (SEM), and atomic force microscopy (AFM) were used to study the evolution of microstructures. In vitro corrosion resistance was assessed using potentiodynamic polarization and a room-temperature immersion test in simulated body fluid (SBF). The fluoride-treated Mg–Zn–Al–0.5Ca alloy formed by 24h immersion in HF exhibited a more homogeneous, compact, and thicker (2.1 μm) coating layer compared to the other HF treated specimens in 6, 12, and 18 hours. The corrosion resistance performance of the Mg–Zn–Al–0.5Ca alloy formed by 24h immersion in HF was the best, with a corrosion rate of 2.87 mm/y according to the electrochemical experiment. The mean weight loss of the untreated samples was considerably higher (up to 2 times) than that of the fluoride-treated alloys, according to in vitro degradation assessments. According to the findings, the fluoride-treated Mg–Zn–Al–0.5Ca alloy is a promising candidate for biodegradable implants because of its low degradation kinetics and apatite formation ability.

Citation: Rezaei-Baravati, A.; Kasiri-Asgarani, M.; Bakhsheshi-Rad, H.R.; Omidi, M.; Karamian, E. (2022) Effect of Fluoride Coating on the Degradation of Mg-Based Alloy Containing Calcium for Biomedical Applications, Journal of Advanced Materials and Processing, 10 (1), 67-76. Dor: 20.1001.1.2322388.2022.10.1.6.9

† **Corresponding Authors**
E-Mail Address: m.kasiri@pmt.iaun.ac.ir; rezabakhsheshi@pmt.iaun.ac.ir

1. Introduction

Mg and its alloys have been extensively investigated as biodegradation implant materials due to their remarkable qualities, such as analogous density (1.74–1.84 g/cm^3) and elastic modulus (41–45 GPa) to human bones, high strength to weight ratio, and good biocompatibility. Nevertheless, the high corrosion rate and localized/pitting corrosion behavior reduced their mechanical solidity as an implant, severely restricting magnesium alloy's therapeutic application for orthopedic fixation systems [1]. Presently, the corrosion rate of magnesium can be controlled by employing two methodologies: composition alteration and alloy surface treatment. One of the essential tools for enhancing the corrosion resistance of Mg alloy is alloying. Ca is an essential alloying component in human bone, and the release of Mg and Ca ions can improve bone recovery [2]. Zinc can also enhance castability, increase age-hardening response, form intermetallic compositions, alter and refine grain size. The incorporation of aluminum improves fluidity and tensile strength by strengthening the solid solution and corrosion resistance [3]. Aluminum at low concentrations has been proposed as an alloying element for biomedical applications. Surface modification, in addition to micro-alloying, is used to boost the corrosion resistance of magnesium alloys. For medical applications, the ideal magnesium alloy coating has characteristics such as corrosion resistance, degradability, and biocompatibility [4]. Surface modifications are classified based on the approach of coating preparation, which includes mechanical, physical, chemical, and biological or biomimetic [5-7]. The reaction between the magnesium substrate and the conversion coated media produces a chemical coating layer that is strongly bonded to the substrate. Because it is based on chemical reactions, it might be more susceptible to thermodynamics and kinetics [4]. Recently, fluoride treatment has been considered to be an effective method for preparing a protective chemical fluoride conversion coating (MgF_2) for Mg alloy with high corrosion resistance [8]. Fluoride coatings have been shown to improve the corrosion resistance of magnesium alloys [9, 10] and to have proper biocompatibility. Furthermore, it is assumed that the film has a high binding force with the magnesium matrix attributed to the presence of chemical bonds between magnesium and fluoride ions [11]. The coating layer (MgF_2) has also been indicated to present high density while staying chemically inert and nontoxic, as well as lowering solubility in water. Furthermore, fluorine is a component of human bone and teeth [12]. In this study, fluoride coating was generated on Mg–Zn–Al–0.5Ca alloy, and its compositions, microstructures, electrochemical, and in vitro dynamic degradation performance were investigated.

2. Materials and methods

2.1. Specimen preparation

Pure Mg ingot (99.9%), high purity Al chips (99.9%), pure zinc chips (99.9%), and Mg–40Ca master alloy were used as starting materials. In a mild steel crucible with argon gas flow, the components were melted for 30 minutes at 690°C. Upon the melting and alloying procedures, molten metal with a 0.5 weight percent Ca concentration was poured into a pre-heated mild steel mold to form ingots. Several disk samples (φ15mm × 5mm) were cut from the ingots. Each specimen's surface was wet-ground with 320 to 2000 silicon carbide emery papers before rinsing twice in distilled water. And after electro-polishing at room temperature was microstructurally analyzed using scanning electron microscopy.

2.2. Conversion coating treatment and characterization

A warm air flow was utilized to dry the polished specimens after being bathed entirely with distilled water, rinsed, and degreased ultrasonically with ethanol. Finally, the specimens were bathed with distilled water, dried, and stored for future inquiry. After that, the specimens were immersed in 40 wt.% hydrofluoric acid at room temperature for varying lengths of time (6, 12, 18, and 24 h). After being treated with hydrofluoric acid, the samples were rinsed with distilled water and air-dried. The samples before any treatment and the final mass after each period of immersion were measured using analytic balance to evaluate the mass change. The microstructures of the untreated and fluoride-coated specimens were confirmed by scanning electron microscopy (SEM, Jeol Jsm-6380LA), and the chemical compound of the alloys was determined by energy-dispersive spectroscopy (EDS, Zeiss Supra 33VP). The microstructural stages of the untreated and treated specimens were determined using X-ray diffractometry (XRD). The experiment was conducted using a diffractometer (XRD, Siemens D500) using Cu–K_α (λ = 1.540598 Å) radiation and operated at 40 kV and 35 mA. The specimens' surface topography was examined utilizing an atomic force microscope (AFM, NanoScope IV, Digital Equipment) (tapping). A non-contact microscope was used to capture the images.

2.3 Corrosion test

2.3.1 Electrochemical tests

The electrochemical test was conducted in a glass cell that includes 200 mL of Kokubo simulated body fluid (SBF) [13] at pH 7.66, utilizing Versastat 3 potentiostat/ galvanostat (Princeton Applied Research) at 37 °C. Table 1 shows the chemical combination of the SBF medium. Furthermore, for

the potentiodynamic polarization assessments, a saturated calomel electrode (SCE) and a graphite rod were utilized as the reference and counter electrodes, respectively, with the sample serving as the working electrode in a three-electrode cell. All tests were recorded at a scan rate of 0.5 mV/s, beginning at −250 mV_{SCE} below the open circuit potential. The specimens' surfaces were exposed to the solution. The exposed area surface was approximately 1 cm^2. For each treatment condition, four measurements were carried out as well for the untreated specimens. This fitting can be controlled manually using the software. A section of the curve from E_{corr} (V_{SCE}) was selected for the Tafel fittings, and i_{corr} was determined from the value where the fit met the E_{corr} (V_{SCE}) potential value. All testing was conducted three times to confirm the reproducibility of the findings.

Table 1. Kokubo simulated body fluid's chemical compound.

Solution	Ion concentration (mmol/L)							
	Na^+	K^+	Ca^{2+}	Mg^{2+}	HCO_3^-	Cl^-	HPO_4^{2-}	SO_4^{2-}
Human blood plasma	142.0	5.0	2.5	1.5	27.0	103.0	1.0	0.5
Kokubo (c-SBF)	142.0	5.0	2.5	1.5	4.2	147.8	1.0	0.5

2.3.2 Immersion test

For in vitro testing, fluoride-coated and untreated specimens were immersed in 150 mL Kokubo simulated body fluid (SBF) at pH 7.66, according to ASTM G31-72. The beakers were sealed and incubated at a consistent temperature of 37 °C for a week. Following that, the specimens were extracted from the SBF, gently washed with distilled water, and dried in room temperature air for surface examination. To determine the average corrosion rate, specimens were immersed in acetone, deionized water solution for varying lengths of time and then cleaned in acetone, and deionized water solution to remove corrosion products developed on the specimens. The corrosion rate was calculated as follows:

$$C_R = \frac{W}{At\rho} \quad (1)$$

where C_R indicates corrosion rate and w represents weight loss A is the initial surface area exposed to SBF; ρ is the density of Mg alloy; while t is the length of immersion employed in this investigation [12]. SBF specimens were immersed for 12 h intervals. The average pH of the samples was taken from three measurements. After the immersion test, the surface appearance of corroded specimens was looked at by using SEM and EDS to look at them.

3. Results and discussion

3.1 Preparation of specimens

In a displacement reaction, magnesium and HF form MgF_2 layer, which is insoluble and provides a barrier coating for magnesium. Initial studies with MZA-0.5Ca samples in HF at varied treatment periods demonstrated a quite slow reaction between Mg and HF. There were few or no bubbles noticed during immersion. The time change of the increase in mass per unit area is seen in Fig.1. With increasing immersion time, the graph reveals a constant rise in mass and thus growth of the MgF_2 film, although the rate of progress is slow. It is worth noting that slow growth of MgF_2 film due to its character as a barrier. Nevertheless, the increase in mass must only be described as an estimate of the MgF_2 film growth. A simple conversion of mass added to film thickness taking an increase from F would result in an underrate. This is due to the dissolution of Mg into the acid and removing the oxide/hydroxide from the sample surface, which would lower the mass. As the immersion time for all samples increased from 18 to 24 h, the slope of the mass curve, as shown in Fig. 1, decreased due to a decrease in deposition rate. These results were similar to prior investigations, which indicated that deposit development might occur at the film/metal interface since the mobility of the F ions is high. As a result, as the film thickness grows, deposit growth decreases.

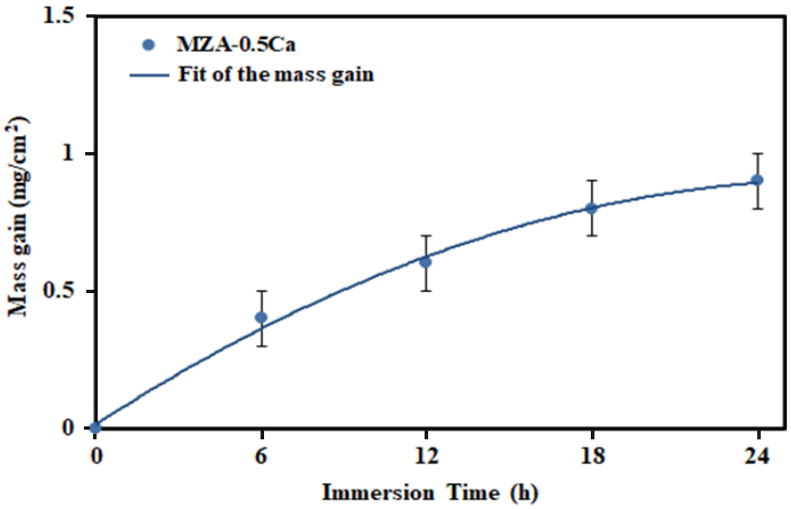

Fig. 1. Variation of specific mass gain of sample as a function of HF treatment time.

As shown in Fig. 2, the appearance of the specimens altered dramatically with treatment time. With immersion times of 6, 12, 18, and 24 h, the specimens were light-bronze, dark-bronze, light-golden, dark-golden, and black. The specimens had a grey color after 24 h of immersion, which darkened with increasing treatment time, eventually resulting in black color. This variation in the specimens suggests the existence of various compounds on the sample surface.

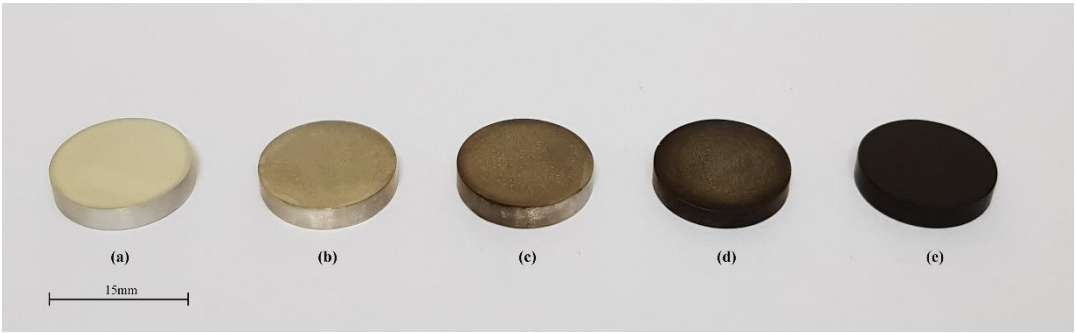

Fig. 2. Optical images of (a) untreated sample, and samples after immersion in the 40% HF solution for (b) 6 h, (c) 12 h, (d) 18 h and (e) 24 h.

3.2 Microstructure and coating characterization

The microstructure of untreated MZA–0.5Ca alloy is shown in Fig. 3a to be composed of α-Mg matrix, $Mg_{17}Al_{12}$, and $(Mg,Al)_2Ca$ phases. $Mg_{17}Al_{12}$ precipitates with spherical morphology were found inside the equiaxial grains of α-solid solution, according to microstructure analyses. Phase $(Mg,Al)_2Ca$ has been identified using XRD and EDS analysis, with some Al entering the Mg_2Ca structure. Based on the Mg–Ca and Mg–Al–Ca phase diagrams, a small content of calcium can be dissolved in the α-Mg matrix, so it is possible that the lamellar eutectic $(Mg,Al)_2Ca$ particles form during melt solidification and the tiny granular $(Mg,Al)_2Ca$ particles form after solidification. Fig. 3b-e illustrates the surface morphology of fluoride-treated samples following the immersion in HF acid for 24 hours. On the surface of the specimen, a compact film with some irregularly distributed pores can be seen. Many corrosive micro-batteries could be created on the surface of the specimen when they were immersed in hydrofluoric acid. The magnesium might be dissolved in the micro-anode region [9] and reactions could occur as follows:

$$Mg \rightarrow Mg^{2+} + 2e^- \quad (2)$$

$$2H^+ + 2e^- \rightarrow H_2 \uparrow \quad (3)$$

Meanwhile, the Mg^{2+} reacted with F^- ion, and thus MgF_2 can be established and reactions could occur as follows [9]:

$$Mg^{2+} + 2F^- \rightarrow MgF_2 \quad (4)$$

As the reaction progresses, the reaction interface of magnesium dissolution should be reduced, and thus the deposition of MgF_2 should be slowed. As a result, as the thickness of the film increased, its growth slowed. After 24 h of immersion in hydrofluoric acid, the surface barrier film was thick enough just to stop the reaction. An oxidation reaction occurred during the formation of MgF_2 according to Ref. [9]:

$$Mg + 2H_2O \rightarrow Mg(OH)_2 + H_2 \uparrow \quad (5)$$

$$Mg(OH)_2 + 2HF \rightarrow MgF_2 + 2H_2O \quad (6)$$

$$Mg(OH)_2 \rightarrow MgO + H_2O \quad (7)$$

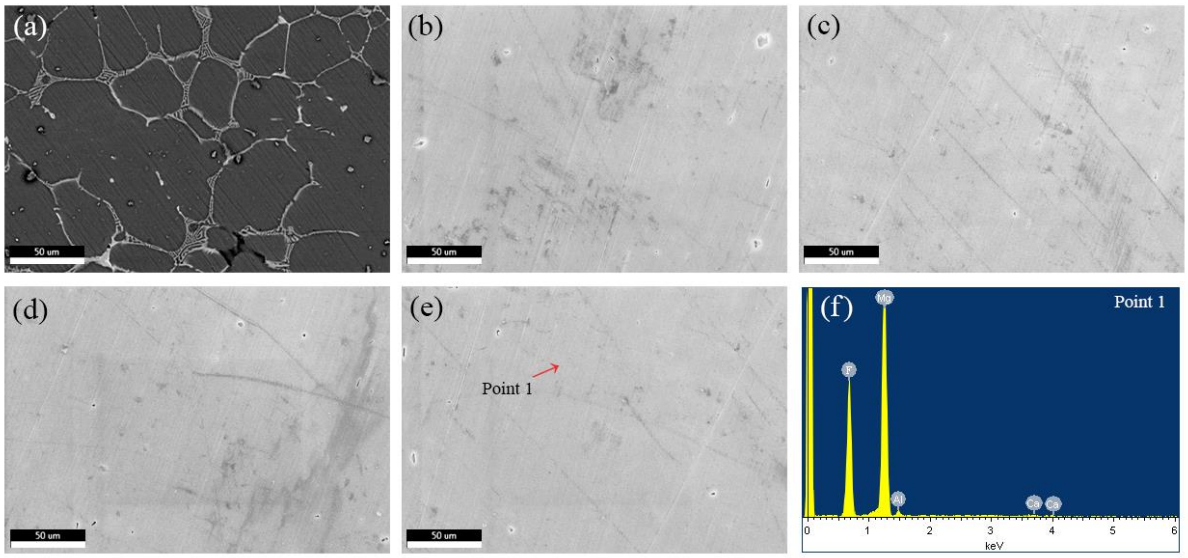

Fig. 3. SEM images of the (a) untreated sample, and fluoride-coated MZA-0.5Ca samples after immersion in the 40% HF solution for (b) 6 h, (c) 12 h, (d) 18 h, (e) 24 h, and (f) EDS spectrum of point 1.

The coating layer is composed of Mg, Ca, Al and F elements, according to EDS analysis of treated samples (Fig. 3f). The presence of fluoride demonstrated that HF acid was involved in creating the coating layer. Since the coating was narrow, the alloy substrate was also recognized in the range with excellent resolution [9, 14]. Furthermore, the XRD patterns of the untreated sample are shown in Fig. 4a, where low intensities peaks related to the $Mg_{17}Al_{12}$ and $(Mg,Al)_2Ca$ phases were observed in the MZA-0.5Ca alloy [15]. During the primary processing of this alloy, the presence of such particles may cause the development of specific dynamic and static recrystallization behaviors [16]. The XRD pattern from the fluoride conversion layer on MZA-0.5Ca alloy is shown in Fig. 4. Aside from the peaks of α-Mg substrates, some new peaks were detected due to MgF_2 reflection. According to the XRD results, the film on the MZA-0.5Ca alloy is MgF_2. The low intensity of the diffraction peaks implies that MgF_2 has low crystallinity.

Fig. 5 clearly shows that the thickness of the fluoride conversion coating was proportional to the treatment time. With increasing treatment time, the fitting curve shows a monotonic increase in thickness and thus growth of the fluoride coating. However, as the treatment continued, the rate of growth slowed. The coating thickness had achieved a constant value of about 2.1 μm after 24 h.

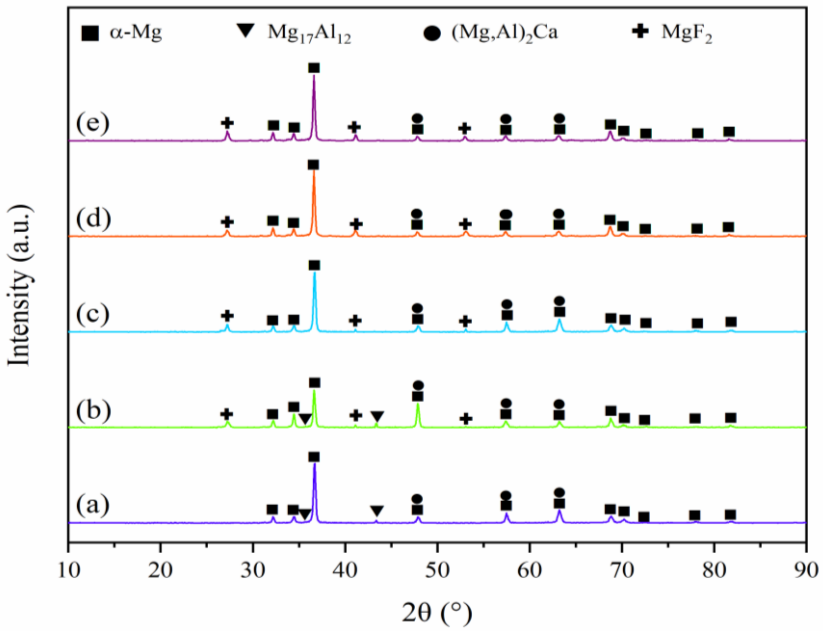

Fig. 4. XRD patterns of (a) untreated sample, and fluoride-coated MZA-0.5Ca samples after immersion in the 40% HF solution for (b) 6 h, (c) 12 h, (d) 18 h and (e) 24 h

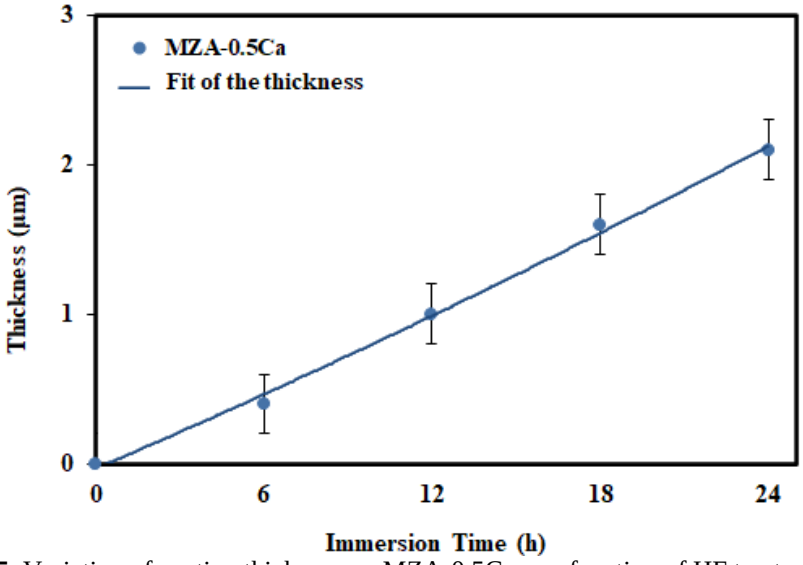

Fig. 5. Variation of coating thickness on MZA-0.5Ca as a function of HF treatment time

Fig. 6 depicts the mean surface roughnesses (R_a) of treated and untreated specimens. The corrosion behavior of the treated samples is significantly influenced by surface roughness. It was demonstrated that decreasing sample surface roughness reduced surface area for the corrosive attack [17]. The surface may become coarser after fluoride treatments, according to atomic force microscope (AFM) measurements. Untreated specimens had an average roughness of 271 nm, while 24h treated specimens had an average roughness of 335 nm.

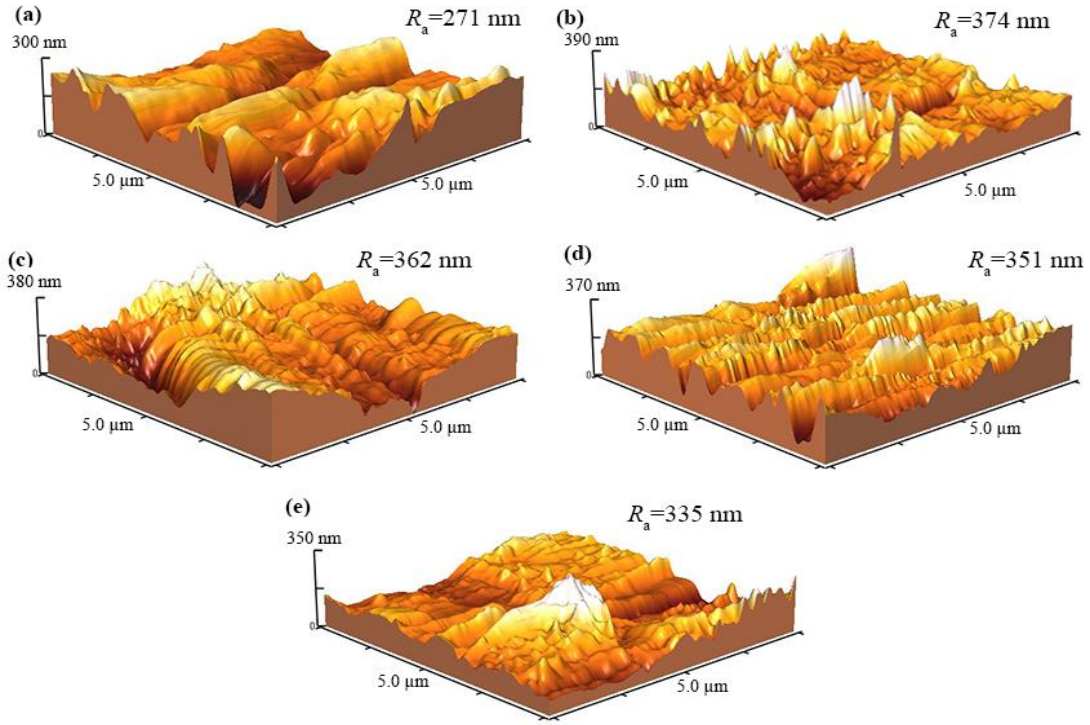

Fig. 6. Atomic force microscopy of (a) untreated specimens and fluoride-coated MZA-0.5Ca specimens following the immersion in a 40% HF solution for (b) 6 h, (c) 12 h, (d) 18 h, and (e) 24 h.

3.3 Electrochemical measurement

Fig. 7 depicts typical polarization curves in Kokubo solution for untreated and treated samples. Table 2 shows the corrosion potential E_{corr} and corrosion current density i_{corr} values derived from these curves. The E_{corr} was ennobled due to the fluoride layer, which functioned as a barrier. After 24 h of immersion in hydrofluoric acid, the corrosion rate was reduced to 2.87 mm/year. The polarization curve approximately corresponded in time with that of the untreated sample. Increased immersion duration in the HF solution would raise specimen corrosion resistance ultimately. The corrosion rate of specimens treated for 6, 12, and 18 hours, is higher

than that of those treated for 24 hours. Corrosion resistance is reduced due to cracks in the coating. Cl^- ions might enter the cracks and come into touch with the Magnesium substrate. The cathodic current, which exhibits hydrogen evolution, declined with a lower slope in the treated samples than in untreated samples when the applied potential increased. As the applied potential increased, the anodic current, which shows specimen dissolution, increased with a greater slope in the untreated specimen than in the coated specimens. This behavior might be caused by localized corrosion and then the pit growth [18]. The corrosion potential has been shifted slightly to the negative side. Even a very thin film of MgF_2 appears to be sufficient to significantly slow down corrosion.

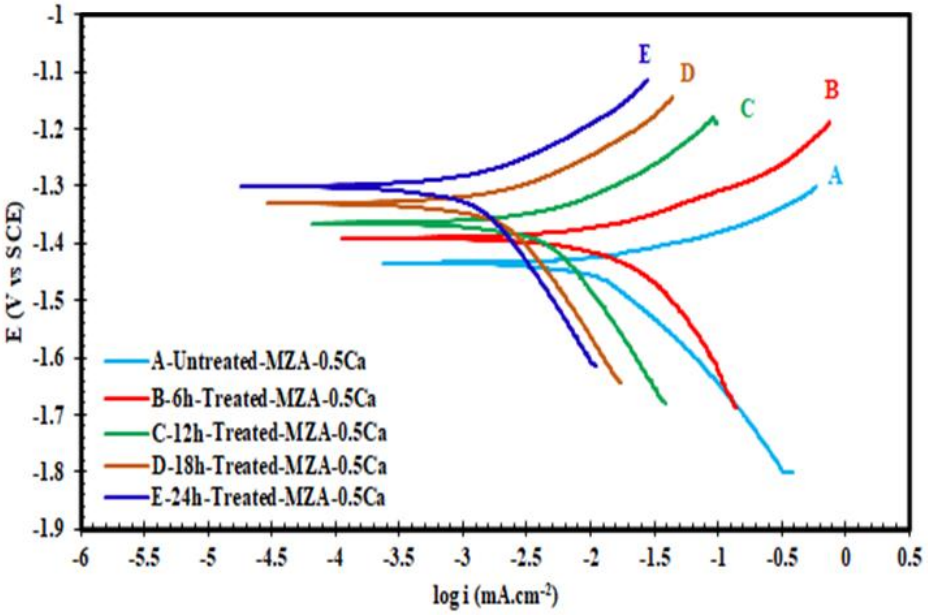

Fig. 7. Polarization curves for untreated MZA-0.5 and fluoride-coated MZA-0.5 samples in SBF solution at 37 °C.

Table 2. Parameters obtained from polarization curves for untreated MZA-0.5 and fluoride-coated MZA-0.5 samples in SBF solution at 37 °C

Specimen	E_{corr} (mV vs. SCE)	i_{corr} (μA/cm^2)	Corrosion rate, C_R (mm/year)
Untreated-MZA-0.5Ca	–1435 ± 12	162 ± 13	3.7 ± 0.21
6h-Treated-MZA-0.5Ca	–1389± 11	153± 14	3.49± 0.28
12h-Treated-MZA-0.5Ca	–1372± 15	144± 15	3.29± 0.25
18h-Treated-MZA-0.5Ca	–1341± 14	135± 12	3.08± 0.24
24h-Treated-MZA-0.5Ca	–1309± 11	126± 13	2.87± 0.22

3.4 In vitro degradation mechanism of fluoride coated MZA−0.5Ca alloy

Fig. 8 depicts the weight loss of untreated and fluoride-treated (40% HF treated) samples in Kokubo solution after 168 hours. During the initial stages of the test, it was discovered that the film might operate as a corrosion barrier covering the matrix, leading to a much-reduced degradation rate of the treated specimens in comparison with the untreated specimens. The degradation rate of fluoride-treated samples is influenced by two factors. The thickness of the coating layer is the first consideration. It was discovered during chloride solution testing that increasing the thickness of the dense layer inhibits the additional corrosion in Mg [19]. Surface roughness is another element that influences the corrosion rate of treated samples. Nevertheless, the weight loss rate was dramatically decreased after 72 hours due to the deposition of hydroxyapatite (HAp) on the sample [20]. For the entire stage, treated specimens had significantly lower mass losses than untreated specimens. This indicated that the MgF_2 film might operate like a corrosion-barrier covering on the alloy, resulting in a decreased degradation rate on the MZA-0.5Ca alloy.

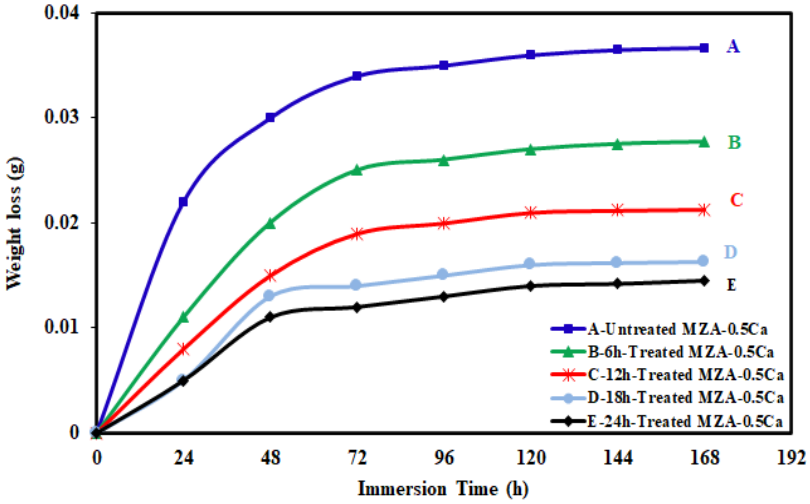

Fig. 8. The weight loss of untreated MZA-0.5 and fluoride-coated MZA-0.5 samples as a function of immersion time in SBF solution

3.5 Immersion tests

Fig. 9a depicts the variation in pH value and the volume of hydrogen evolution of uncoated and fluoride-coated MZA-0.5 samples as a function of the immersion time in SBF solution. The MgF_2 coating also protected the treated alloys from fast degrading when the pH of the immersion solution was increased slightly. The hydrogen evolution volume of treated and untreated samples had an almost linear relationship with immersion duration, which can be seen in Fig. 9b; where untreated alloys generated much more hydrogen bubbles than MgF_2-coated alloys.

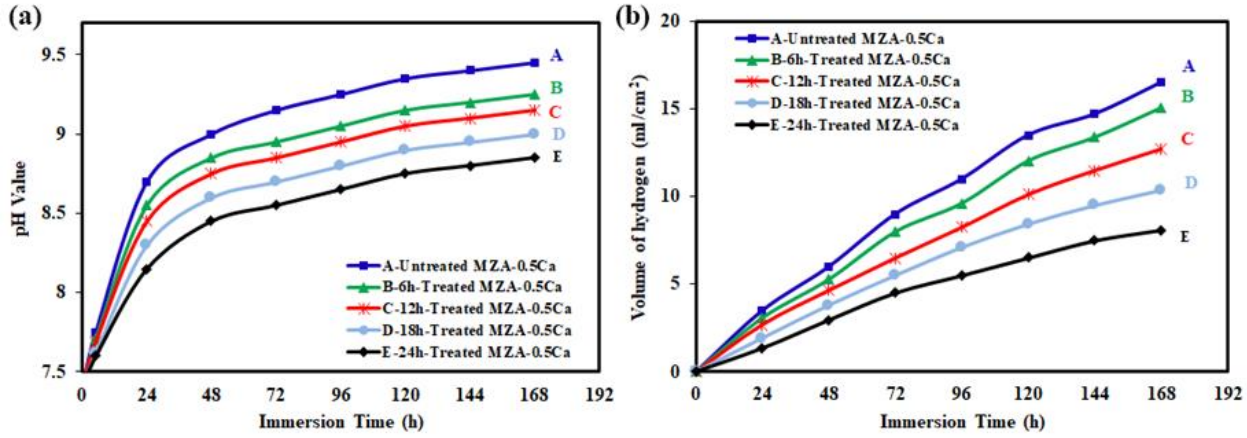

Fig. 9. (a) The variation in pH value in SBF solution and (b) the hydrogen evolution volume of uncoated and fluoride-coated MZA-0.5 samples as a function of the immersion time in SBF solution.

The surface morphology of the untreated and treated MZA-0.5Ca alloys after 168 h in SBF solution is shown in Fig. 10. Untreated samples were found to have a severe corrosion attack as shown in Fig. 10 (a,b). The EDS analysis in Fig. 10 shows that the corroded sample surface contained C, O, P and primarily Mg, with trace Ca detected. The surface morphology of the samples (MgF_2-coated) after 6, 12, 18, 24h HF-treatment for 168 h immersion are shown in Fig. 10(c-j). After the immersion test, the surface of the HF-treated sample experienced mild corrosion attacks, while untreated samples suffered from serious corrosion attacks. The MgF_2 coating shields the treated samples from the electrolyte, reducing chloride ion corrosive attack. As a result, corrosion of treated samples cannot begin until the protective coating has dissolved or peeled. The reduction of corrosion rate of Mg alloy implants is guaranteed by the service life of the surface coating [21,22]. The EDS analysis shows that compounds rich in Ca and P had deposited on the MgF_2 film which may imply the formation of hydroxyapatite.

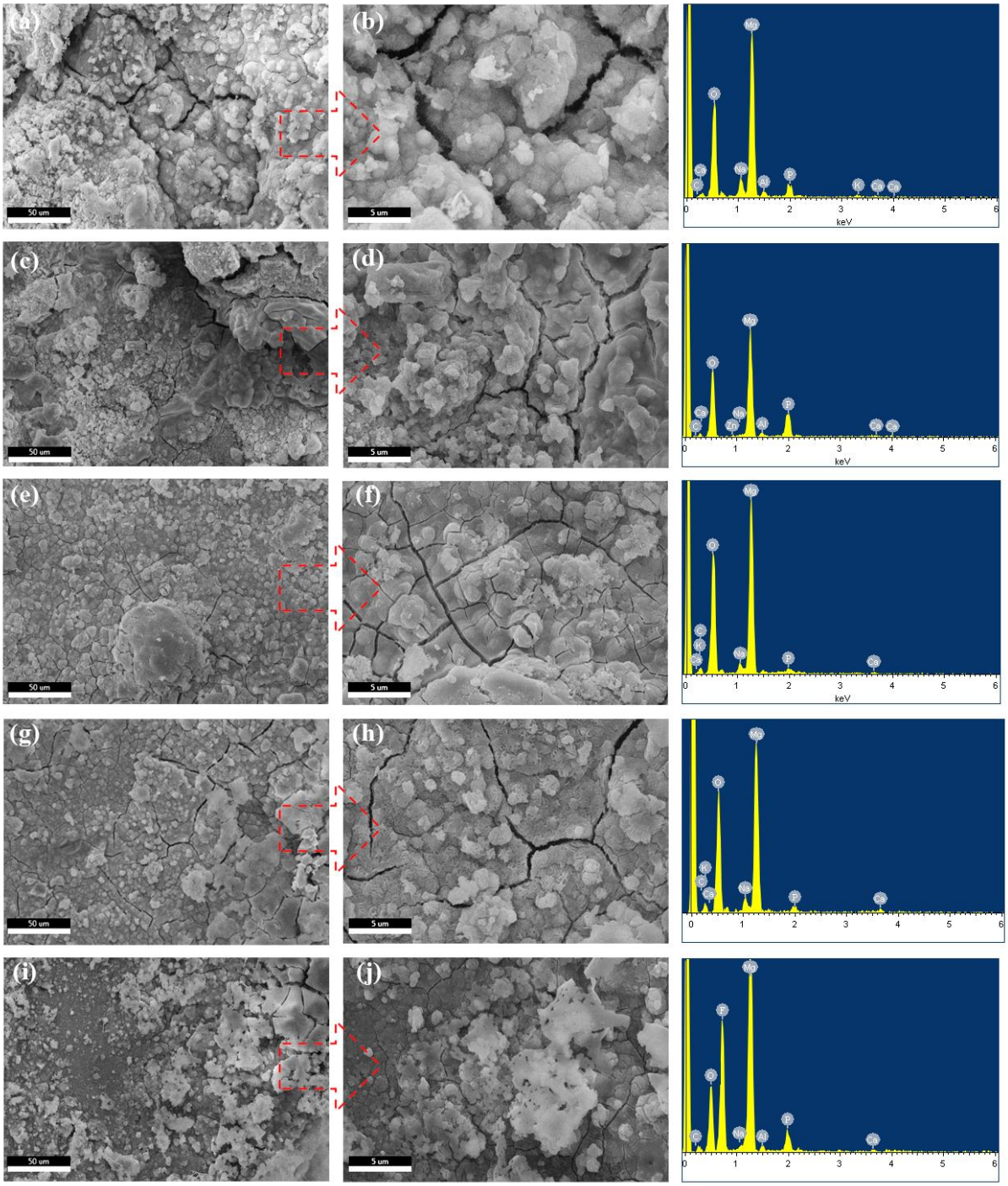

Fig. 10. The surface morphologies and EDS spectrum of (a,b) uncoated MZA-0.5Ca alloy, and samples after (c,d) 6h, (e,f) 12h, , (g,h) 18h and (i,j) 24h F-treatment for 168 h immersion in SBF solution and corresponding EDS analysis.

4. Conclusions

On the MZA-0.5Ca alloy, a facile conversion coating method was established employing HF at room temperature. The corrosion resistance in SBF solution was tested after the coated specimens were characterized and the following conclusions were attained.

1) A uniform and compact coating of about 2.1 μm thick was created after 24 hours of immersion in 40% HF, and the conversion immersion was mainly composed of tetragonal MgF_2.

2) EIS and polarization tests exhibited that the fluoride conversion coating significantly increased corrosion resistance. In addition, the degradation rate in vitro of fluoride-treated alloys in the SBF solution is slower than the untreated alloys.

3) A viable option for biodegradable medical implants is MZA-0.5Ca alloy treated with HF for 24 hours because of its low degradation kinetics and formation of corrosion protective layers on the surface of MZA-0.5Ca alloy.

References

[1] C. Zhang, S. Zhang, D. Sun, J. Lin, F. Meng, H. Liu, "Superhydrophobic fluoride conversion coating on bioresorbable magnesium alloy–fabrication, characterization, degradation and cytocompatibility with bmscs", J. Magnesium Alloys, Vol. 9, No. 4, 2021, pp. 1246-1260.
[2] S. Ghaedi Faramoushjani, F. Chinaei, H.R. Bakhsheshi-Rad, M. Hasbullah Idris, "Effect of fluoride conversion coating on corrosion of behavior of mg-ca-zn alloy", Proc. Advanced Materials Research, 2013, pp. 3-6.
[3] I. Baghni, Y.-S. Wu, J.-Q. Li, C. Du, W. Zhang, "Mechanical properties and potential applications of magnesium alloys", Trans. Nonferrous Met. Soc. China, Vol. 13, No. 6, 2003, pp. 1253-1259.
[4] Z.-Z. Yin, W.-C. Qi, R.-C. Zeng, X.-B. Chen, C.-D. Gu, S.-K. Guan, Y.-F. Zheng, "Advances in coatings on biodegradable magnesium alloys", J. Magnesium Alloys, Vol. 8, No. 1, 2020, pp. 42-65.
[5] X. Xiong, Y. Yang, J. Li, M. Li, J. Peng, C. Wen, X. Peng, "Research on the microstructure and properties of a multi-pass friction stir processed 6061al coating for AZ31 Mg alloy", J. Magnesium Alloys, Vol. 7, No. 4, 2019, pp. 696-706.
[6] Y. Guo, Y. Zhang, Z. Li, S. Wei, T. Zhang, L. Yang, S. Liu, "Microstructure and properties of in-situ synthesized ZrC-Al3Zr reinforced composite coating on AZ91D magnesium alloy by laser cladding", Surf. Coat. Technol., Vol. 334, 2018, pp. 471-478.
[7] X.-B. Chen, H.-Y. Yang, T.B. Abbott, M.A. Easton, N. Birbilis, "Corrosion protection of magnesium and its alloys by metal phosphate conversion coatings", Surf. Eng., Vol. 30, No. 12, 2014, pp. 871-879.
[8] S. Li, L. Yi, X. Zhu, T. Liu, "Ultrasonic treatment induced fluoride conversion coating without pores for high corrosion resistance of Mg alloy", Coatings, Vol. 10, No. 10, 2020, pp. 996.
[9] T. Yan, L. Tan, D. Xiong, X. Liu, B. Zhang, K. Yang, "Fluoride treatment and in vitro corrosion behavior of an AZ31B magnesium alloy", Mater. Sci. Eng., C, Vol. 30, No. 5, 2010, pp. 740-748.
[10] F. Witte, J. Fischer, J. Nellesen, C. Vogt, J. Vogt, T. Donath, F. Beckmann, "In vivo corrosion and corrosion protection of magnesium alloy LAE442", Acta Biomater., Vol. 6, No. 5, 2010, pp. 1792-1799.
[11] Y. Chen, Y. Song, S. Zhang, J. Li, H. Wang, C. Zhao, X. Zhang, "Effect of fluoride coating on in vitro dynamic degradation of Mg–Zn alloy", Mater. Lett., Vol. 65, No. 17-18, 2011, pp. 2568-2571.
[12] M. Ren, S. Cai, T. Liu, K. Huang, X. Wang, H. Zhao, S. Niu, R. Zhang, X. Wu, "Calcium phosphate glass/MgF_2 double layered composite coating for improving the corrosion resistance of magnesium alloy", J. Alloys Compd., Vol. 591, 2014, pp. 34-40.
[13] T. Kokubo, H. Takadama, How useful is SBF in predicting in vivo bone bioactivity?, Biomaterials Vol. 27, 2006, pp. 2907–2915.
[14] C. Zhang, C. Liu, Y. Ma, "Preparation of compound coating of fluorine conversion layer and calcium phosphate on AZ31 magnesium alloy", Mater. Res. Innovations, Vol. 18, No. sup2, 2014, pp. S2-564-S2-569.
[15] J. Yang, J. Peng, E.A. Nyberg, F.-s. Pan, "Effect of Ca addition on the corrosion behavior of Mg–Al–Mn alloy", Appl. Surf. Sci., Vol. 369, 2016, pp. 92-100.
[16] S.Z. Khalajabadi, M.R.A. Kadir, S. Izman, R. Ebrahimi-Kahrizsangi, "Fabrication, bio-corrosion behavior and mechanical properties of a mg/ha/mgo nanocomposite for biomedical applications", Mater. Des., Vol. 88, 2015, pp. 1223-1233.
[17] E. Budke, J. Krempel-Hesse, H. Maidhof, H. Schüssler, "Decorative hard coatings with improved corrosion resistance", Surf. Coat. Technol., Vol. 112, No. 1-3, 1999, pp. 108-113.
[18] Y. Wan, G. Xiong, H. Luo, F. He, Y. Huang, X. Zhou, "Preparation and characterization of a new biomedical magnesium–calcium alloy", Mater. Des., Vol. 29, No. 10, 2008, pp. 2034-2037.
[19] X. Gu, W. Zheng, Y. Cheng, Y. Zheng, "A study on alkaline heat treated Mg–Ca alloy for the control of the biocorrosion rate", Acta Biomater., Vol. 5, No. 7, 2009, pp. 2790-2799.
[20] B.-L. Yu, J.-K. Lin, J.-Y. Uan, "Applications of carbonic acid solution for developing conversion coatings on Mg alloy", Trans. Nonferrous Met. Soc. China, Vol. 20, No. 7, 2010, pp. 1331-1339.
[21] X. Gu, N. Li, W. Zhou, Y. Zheng, X. Zhao, Q. Cai, L. Ruan, "Corrosion resistance and surface biocompatibility of a microarc oxidation coating on a Mg–Ca alloy", Acta Biomater., Vol. 7, No. 4, 2011, pp. 1880-1889.
[22] H.R. Bakhsheshi-Rad, M.H. Idris, M.R.A. Kadir, M. Daroonparvar, "Effect of fluoride treatment on corrosion behavior of Mg–Ca binary alloy for implant application", Trans. Nonferrous Met. Soc. China, Vol. 23, No. 3, 2013, pp. 699-710.